

**Titre:** Portable 3D Interferometric Microscopy for Microfluidic-Based  
Title: Platforms

**Auteur:** Isam Gharib  
Author:

**Date:** 2020

**Type:** Mémoire ou thèse / Dissertation or Thesis

**Référence:** Gharib, I. (2020). Portable 3D Interferometric Microscopy for Microfluidic-Based  
Citation: Platforms [Mémoire de maîtrise, Polytechnique Montréal]. PolyPublie.  
<https://publications.polymtl.ca/4229/>

 **Document en libre accès dans PolyPublie**  
Open Access document in PolyPublie

**URL de PolyPublie:** <https://publications.polymtl.ca/4229/>  
PolyPublie URL:

**Directeurs de  
recherche:** Mohamad Sawan  
Advisors:

**Programme:** génie électrique  
Program:

**POLYTECHNIQUE MONTRÉAL**

affiliée à l'Université de Montréal

**Portable 3D interferometric microscopy for microfluidic-based platforms**

**ISAM GHARIB**

Département de génie électrique

Mémoire présenté en vue de l'obtention du diplôme de *Maîtrise ès sciences appliquées*

Génie électrique

Mars 2020

**POLYTECHNIQUE MONTRÉAL**

affiliée à l'Université de Montréal

Ce mémoire intitulé :

**Portable 3D interferometric microscopy for microfluidic-based platforms**

présenté par **Isam GHARIB**

en vue de l'obtention du diplôme de *Maîtrise ès sciences appliquées*

a été dûment accepté par le jury d'examen constitué de :

**Christian CARDINAL**, président

**Mohamad SAWAN**, membre et directeur de recherche

**L'Hocine YAHIA**, membre

**DEDICATION**

*To all my friends,*

...

## ACKNOWLEDGEMENTS

I would like to express my sincere gratitude to my research director Prof. Mohamad Sawan that gave me the opportunity to pursue my researches in Polystim Neurotechnologies Laboratory, and all the technical and general supports in these few years at Polytechnique Montreal. I appreciate Prof. Christian Cardinal and Prof. L'Hocine Yahia for kindly accepting to evaluate this thesis. I am grateful to all the staff of Electrical Engineering Department of Polytechnique Montreal, especially Nathalie Lévesque, Marie-Yannick Laplante, Laurent Mouden, Maxime Thibault, and, Réjean Lepage for all their help. I would also like to thank my colleagues and friends at Polystim for useful discussions and help, especially Ahmad Hassan, Aref Trigui, Mohamed Ali, Mostafa Amer, Ahmed Abubakr, Nader Zarif, and, Seyed Mohammad Noghabaei. Also, special thanks to Prof. William Skene that gave me the access to his laboratory for fluorescence lifetime measurements. I would like to acknowledge Natural Sciences and Engineering Research Council of Canada (NSERC) for the support and Canadian Microelectronics Corporation (CMC) Microsystems for the design and simulation tools.

## RÉSUMÉ

Ce projet de maitrise s'intitule dans le cadre de la technologie des Organes-sur-puces visant comme perspective l'examen de médicaments. Prenant un cas concret celui du traitement du Cancer, l'idée constructive est de créer un microenvironnement 3D simulant les interactions entre les cellules cancéreuses, il s'est avéré que leurs comportements est similaire à celles vivantes dans le vrai environnement biologique. Un réseau de microcapteurs doit être réalisé pour mesurer les différents paramètres de l'activité cellulaire, à savoir le pH, Glucose, Lactate et l'urée. Ces paramètres permettent d'évaluer le degré de l'efficacité du médicament ajouté tout en mesurant le niveau d'activité de ces cellules, leur métabolisme ainsi que leur prolifération. Outre que cela, pour éviter toute intervention risquée sur l'animal ou sur le corps humain, cette plateforme conçue représente une solution alternative pour le développement et la vérification de nouveaux médicaments. La mesure de ces paramètres biochimiques en 3D et en temps réel représente le défi majeur de ce projet. A ce propos, un système hybride optique-microfluidique non invasif est proposé mesurant les valeurs de la durée de vie de la fluorescence dans chaque endroit de l'environnement 3D et en se basant sur la technologie DMD (digital micromirror device) pour deviser et diriger la lumière vers les directions voulues. Tout changement dans la valeur de cette durée de vie donne des informations sur le changement des spécifications biochimiques dans l'échantillon. Les différentes parties de ce système ont été conçues de telle sorte qu'elles soient intégrables et donc permettre d'avoir un instrument facile à utiliser transportable dans des endroits de températures et d'oxygènes présentant des milieux favorables pour les cellules biologiques.

## ABSTRACT

This master degree project is within the context of Organs-On-Chip technology for the main purpose of drug testing related to Cancer treatment, for example. This can be done by creating a 3D micro-environment in which Cancer cells could interact like those who are in the real biological environment. A sensor network should be designed to measure the variation of cells activities, such as pH, Glucose, Lactate and urea. The measurement of these parameters is a strong tool to validate the efficiency of the injected drug, by determining the level of cells activity, their metabolism and their proliferation. Thus, to avoid any intervention risk on animal or human body, this designed platform represents an alternative solution for developing and verification of new drugs. The measurement of these biochemical parameters in 3D and in real time is the main challenge in this project. Therefore, a new hybrid opto-microfluidic non invasive system was proposed while measuring the fluorescence lifetime in every location inside the 3D environment and based on DMD (digital micromirror device) technology to drive the excitation light beams to the desired directions. Any change in this lifetime value gives information about biochemical specifications change in the sample. This proposed system was designed and fabricated in a way that we can have a full integrated instrument that can be easily introduced inside cell culture incubators for a specific temperature and oxygen required by biological cells to survive.

## TABLE OF CONTENTS

DEDICATION . . . . .	iii
ACKNOWLEDGEMENTS . . . . .	iv
RÉSUMÉ . . . . .	v
ABSTRACT . . . . .	vi
TABLE OF CONTENTS . . . . .	vii
LIST OF TABLES . . . . .	ix
LIST OF FIGURES . . . . .	x
LIST OF SYMBOLS AND ACRONYMS . . . . .	xiv
LIST OF APPENDICES . . . . .	xv
CHAPTER 1 INTRODUCTION . . . . .	1
CHAPTER 2 LITERATURE REVIEW . . . . .	5
2.1 Fluorescence Lifetime Method . . . . .	5
2.1.1 Principle and Theory . . . . .	5
2.1.2 Techniques . . . . .	6
2.1.3 Processes Affecting Fluorescence Lifetime . . . . .	8
2.2 3D Sensing and Imaging . . . . .	12
2.2.1 Laser Scanning Confocal Microscopy (LSCM) . . . . .	12
2.2.2 Two-Photon Fluorescence Microscopy (TPFM) . . . . .	13
2.2.3 Stimulated Emission Depletion (STED) microscopy . . . . .	14
2.2.4 LED-CT Scan . . . . .	15
CHAPTER 3 3D INTERFEROMETRIC FLUORESCENCE MICROSCOPY . . . . .	17
3.1 Basic Principle . . . . .	17
3.2 System Implementation . . . . .	19
3.3 Experimental Setup . . . . .	21
3.4 Results . . . . .	28



CHAPTER 4	HIGH-EFFICIENCY LED DRIVER . . . . .	32
4.1	Introduction . . . . .	32
4.2	Fluorescence Lifetime Method . . . . .	33
4.3	Novel Driver Circuit . . . . .	36
4.4	Results . . . . .	39
4.5	Conclusion . . . . .	42
CHAPTER 5	VALVES ARRAY FOR A FULL MICROFLUIDIC INTEGRATION .	43
5.1	Introduction . . . . .	43
5.2	Description of the Proposed System . . . . .	45
5.3	Results . . . . .	50
5.4	Conclusion . . . . .	53
CHAPTER 6	ELECTRONIC SYSTEM FOR FULL PORTABILITY . . . . .	54
6.1	Overview . . . . .	54
6.2	System description . . . . .	54
6.2.1	Power Block . . . . .	55
6.2.2	Radio Frequency Communication . . . . .	55
6.2.3	Sensors Read-Out Circuit . . . . .	55
6.2.4	Control Unit . . . . .	56
6.3	PCB Design . . . . .	56
CHAPTER 7	CONCLUSION . . . . .	58
APPENDICES	. . . . .	59
REFERENCES	. . . . .	59

## LIST OF TABLES

Table 3.1	UNITS FOR COMPONENTS POSITION . . . . .	20
Table 3.2	FLUORESCENCE LIFETIME VALUE . . . . .	30
Table 4.1	COMPONENTS OF THE LED DRIVING CIRCUIT . . . . .	38
Table 4.2	SIGNAL STATE TIME VALUES . . . . .	38
Table 4.3	PERFORMANCE COMPARISON OF LED DRIVERS . . . . .	41
Table 5.1	TRUTH TABLE OF SCHEMA SHOWN IN FIG. 3. . . . .	45
Table 5.2	PHYSICAL AND GEOMETRICAL DESIGN PARAMETERS FOR THE PROPOSED SYSTEM . . . . .	49
Table 6.1	COMPARISON TABLE FOR DIFFERENT RF MODULES FROM DIFFERENT MANUFACTURERS. . . . .	56

## LIST OF FIGURES

Figure 2.1	Jablonski diagram and a time scale of photophysical processes for organic molecules [25]. . . . .	5
Figure 2.2	Typical absorption and fluorescence emission spectra. The fluorescence spectrum is located at longer wavelengths with respect to the absorption spectrum. The distance between their band maxima is called the Stokes shift [26]. . . . .	6
Figure 2.3	Relative phase shift ( $\phi$ ) and modulation of the excitation (subscript E) and emission (subscript F) light in frequency domain fluorescence spectroscopy. AC and DC indicate the amplitude and offset of the respective waves [28]. . . . .	7
Figure 2.4	Diagram of FRET. Upon excitation by the photon, the electron of the donor is promoted to the excited state (1), followed by the energy transfer to the acceptor excited orbital (2), simultaneous return of the excited electron back to the ground state (3), and excitation of an acceptor (3) [25]. . . . .	9
Figure 2.5	Dexter electron transfer process, where the distance between acceptor and donor is shorter [25]. . . . .	10
Figure 2.6	Fluorescence lifetime of rhodamine 6G in methanol (molecular fluorescence lifetime is $\sim 4$ ns) as a function of the concentration of the dye, for measured lifetime, and measured lifetime corrected for self-absorption. Adapted from [30]. . . . .	11
Figure 2.7	Principle of operation of a laser scanning confocal microscope. Laser light is focused on the thick specimen by reflection from the dichroic mirror (DM) and the objective lens. The laser excites fluorescence throughout the specimen that passes through the DM and is focused onto the image plane. A pinhole only allows light from the confocal plane of the specimen to reach the photomultiplier tube (PMT) [33].	12

Figure 2.8	Basic elements of a laser scanning confocal microscope. Laser light is directed to the scan mirrors via a dichroic mirror. The laser is scanned across the specimen by the scan mirrors and the returning emitted fluorescence is descanned by the same mirrors and transmitted by the dichroic mirror. The fluorescence passes through the barrier filter and is focused on to the pinhole (adjustable iris) before reaching the PMTs. Additional dichroic mirrors can be used to separate fluorescence wavelengths [33]. . . . .	13
Figure 2.9	Basic elements of a two-photon microscope. PMTs detectors do not require pinholes or focused images and are located immediately below the objective [33]. . . . .	14
Figure 2.10	Creation of reduced excitation spot for STED microscopy. The STED (592-nm) laser beam (red) is shaped by a 2 phase plate into a doughnut and concentrically overlaid with the 488- nm excitation laser (blue). The process of STED occurs in the yellow zone to reduce the zone of fluorescence. Increased STED laser power decreases the diameter, d, of the excitation spot [33]. . . . .	15
Figure 2.11	Measure of pH distribution by computed tomography (CT) scan. (a) The concept of the system and (b) the algorithm of CT scan using the projection-slice theorem by ( ) parallel beam or ( ) fan beam [37]. . . .	16
Figure 3.1	Principle of 2-scanning plans: Step 1 provides the information of the segment without arrangement, thanks to the interference; In step 2, each pixel is associated with its corresponding lifetime. . . . .	17
Figure 3.2	The system presentative schema with implemented optical devices. The horizontal and vertical scanning steps of the sample is insured by DMD. The Plano-convex lenses provide a collimated beam from the pulsed and the continuous sources. Mirrors M5 and M6 orientate the generated beams before and after the sample. The rest of the mirrors serves to filter the non-collimated rays and the light noises and residues coming from the sources. Emission filter blocks the direct beams coming from the source and only allow the fluorescence emission to get through. The convex lens picks up the resulting beams and drives it to the high-speed photodiode for measurement. . . . .	20
Figure 3.3	Assembly drawing of the proposed instrument designed by Solidworks software. 123.97 mm x 74.56 mm x 60.92 mm is its sizing. . . . .	21

Figure 3.4	Photograph of the Instrument inside. The grey parts are fabricated by Stereolithography (SLA) while the others are made by Fused Deposition Modeling (FDM) for low cost. . . . .	22
Figure 3.5	Collimator calibration by using four micro-positioners. Two for right/left and two for back/forward. . . . .	23
Figure 3.6	Fabricated PCB for photodiode output signal amplification and LED driving. . . . .	24
Figure 3.7	Experimental setup to test the instrument by measuring the interference between vertical and horizontal blue beam, inside a glass bowl contains fluorescein. In the right bottom is the obtained picture in the dark. . . . .	25
Figure 3.8	FLS920 Fluorescence Lifetime Spectrometer to measure fluorescein lifetime for direct and combined beams. 401.6 nm picosecond pulsed diode laser (77.4 ps) is used as excitation source. . . . .	26
Figure 3.9	Modular structure of the proposed hybrid opto micro-fluidic platform with the photograph of the real fabricated chip. . . . .	27
Figure 3.10	Photodiode output voltage vs LED driver current for vertical, horizontal and combined optical beams. . . . .	28
Figure 3.11	Photodiode output voltage vs fluorescein concentration for vertical, horizontal and combined optical beams. . . . .	29
Figure 3.12	Fluorescence lifetime measurement for direct and combined beams, within three solution on three different pH value. 7.10 for first graph, 6.13 for second graph and 4.89 for the third graph. . . . .	31
Figure 4.1	Poly-amidoamine fluorescence emission decays for pH sensing [56]. . .	34
Figure 4.2	LED rise/fall time improvement driver circuits: (a) Halbritter <i>et al</i> circuit [59]; (b) Toshiki <i>et al</i> circuit [55]. . . . .	35
Figure 4.3	Novel circuit intended to reduce the fall time of the LED. . . . .	36
Figure 4.4	Driver equivalent circuit: (a) Turn-On phase, (b) Turn-Off phase. . .	37
Figure 4.5	Timing diagram of proposed circuit. . . . .	37
Figure 4.6	LED terminal voltage ( $V_{LED}$ ) waveform for a square waveform input with the switching driver. . . . .	39
Figure 4.7	LED terminal voltage ( $V_{LED}$ ) waveform without the switching driver. . .	40
Figure 4.8	Optical fall time vs LED pulse current with and without the switching circuit. . . . .	40
Figure 4.9	Fluorescence lifetime efficiency $\chi$ vs. Lifetime ( $\tau$ ). . . . .	41
Figure 5.1	Body-on-chip model . . . . .	44

Figure 5.2	Two bit DEMUX valve control system and its equivalent logic circuit [69]	45
Figure 5.3	Simplified schema illustrating the proposed system. . . . .	46
Figure 5.4	The proposed valves array system based on geometries variation . . .	47
Figure 5.5	Membrane braking obstacle simulation . . . . .	48
Figure 5.6	Global system schematic to drive 125 channels with 31 DEMUX units and 3 off-chip control lines . . . . .	49
Figure 5.7	The proposed Integrated microfluidic platform . . . . .	50
Figure 5.8	Vertical displacement vs membrane high . . . . .	50
Figure 5.9	Valves displacement vs applied differential pressure . . . . .	51
Figure 5.10	Fluidic flux vs applied differential pressure for valves $V_1, \dots, V_4$ . . . .	52
Figure 5.11	Fluidic flux vs applied differential pressure for valves $W_1, \dots, W_4$ . . .	52
Figure 6.1	Block diagram of the proposed electronic system . . . . .	54
Figure 6.2	PCB board of the designed electronic system . . . . .	57
Figure 6.3	3D card of the designed electronic system . . . . .	57

## LIST OF SYMBOLS AND ACRONYMS

TCSPC	Time-Correlated Single Photon Counting
FRET	Förster Resonance Energy Transfer
LSCM	Laser Scanning Confocal Microscopy
TPFM	Two-Photon Fluorescence Microscopy
STED	Stimulated emission depletion
CT	Computed Tomography
LED	Light Emitting Diode
DMD	Digital Micro-mirror Display
OOC	Organ-On-Chip

LIST OF APPENDICES

Appendix A . . . . . 65

Appendix B . . . . . 66

Appendix C . . . . . 67

Appendix D . . . . . 68



## CHAPTER 1 INTRODUCTION

Biomedical three dimensional (3D) imaging is a valuable tool for studying local living cells behaviors and characterization. The increasing demand of quantitative and accurate extra/intracellular imaging of cells physiology parameters (pH, Oxygen,  $\text{Ca}^{2+}$ , velocity, motion, diffusion) induces the need of more sophisticated and reliable 3D imaging techniques. In cell culturing field, the variation of pH makes a direct impact for the conditioning of the cell culture medium [1][2][3], any gradient of pH can affect the growth of the cells. In order to avoid a bad cell culturing, it is required to precisely control the time-lapse transition of pH and its distribution inside the cell culture medium. Also, visualization of intracellular pH makes the big and the detailed picture of cells function, being related to metabolism and growth [4], endocytosis [5], ion transport and homeostasis [6] and the ability of tumor cells to metastasize [7].

Cancer cell studies shows that the ability of cells to navigate and migrate is determined by four factors: (1) the pore size [8], that makes a constriction arrest for nuclear migration [9], (2) the physical properties of the microenvironment [10] in which the nuclear envelope protein lamin A is the major determinant of nuclear stiffness that affects the migratory potential of cancer cells through small constrictions [11][12], (3) the mechanical deformability of the cell [13], and (4) the cell's ability to generate and transmit forces to the nucleus and the extracellular environment [8][9]. Three-dimensional measurement of this factors promotes better understanding of tumor cell migration and metastasis [14].

One of the important cells parameters is the oxygen concentration which is an essential factor for aerobic organisms and generation of cellular energy (ATP) [15]. The microenvironment and cellular activity play an important role on the variation of energy supply and consumption which generate a gradient of oxygen concentration. In tumor cells for example, the concentration of the oxygen is much less than that of normal cells because of impaired vascular network and therefore a poor oxygen supply. As another example of cellular activities that generate a variation of oxygen concentration, pancreatic cells and brown adipose tissue increase oxygen consumption by respectively synthesizing the insulin and producing heat [16][17]. Thus, the measurement of the 3D intracellular oxygen variation is a fundamental building stone for understanding cellular oxygen dynamics.

Single-particle tracking (SPT) which is the observation of the motion of individual particles within a medium is broadly used to quantify the dynamics of molecules and record useful information about both the environment and the particle in the trajectory [18] such as viruses [19], transport vesicles [20], proteins [21] or lipids [22]. Analysis of this trajectory provides

useful information on the mode of motion, which may be diffusive, motor-directed, confined, or a mixture of these modes [23][24]. Hence, 3D image tracking provides a better sub-view and therefore much more understanding of cell biology phenomenon such as diffusion coefficient variation, Brownian motion and other characteristics.

Many technologies have been developed and investigated for optical 3D imaging and sensing. The challenge of the most existing techniques is the spatial and temporal resolution limits imposed by the detection systems used such as charge-coupled device (CCD) chip and CMOS camera. To mitigate these resolutions issue, we propose in this project a new three-dimensional (3D) imaging and sensing fluorescence microscopy instrument based on lifetime fitting and interference phenomenon. The proposed system in this work investigates a novel method that requires only a simple high-speed photodiode for photon counting and a fitting algorithm to build the full 3D image. To implement this idea, a novel instrument was designed and fabricated in a way that it can be integrated with microfluidics chips to have a full wearable microscope in terms of power and wireless communication. Experimental verification has been done to validate the basic principles of the system and the obtained results are presented likewise.

## CONTRIBUTIONS

During this Master thesis a new 3D fluorescence bio-sensing device was proposed for Organs-On-Chip (OOC) application and micro-fluidic platforms, which was the subject of a patent and an upcoming article. The technique of this new system requires only a simple high-speed photodiode for photon counting and a fitting algorithm to build the full 3D image, which eliminates the need of CCD or CMOS camera that impose temporal and spatial resolutions, and also resolve the problem of Ernst Abbe's diffraction limit. As well, a novel LED driver circuit to achieve a high speed fall time excitation was proposed, which was the subject of the accepted article. This second contribution is a solution for a major challenging point of making a wearable photonic devices that require the fluorescence lifetime method. Furthermore, a submitted article proposes an embedded on-chip valves controller to make this proposed device more suitable for complex microfluidic platforms and Organs-On-Chip applications.

### Upcoming Article

— I. Gharib, and M. Sawan, "Towards Portable 3D Interferometric Fluorescence Microscopy for Microfluidics based platforms".

### Patent (Submitted)

— I. Gharib, and M. Sawan, "Portable 3D Interferometric Fluorescence Microscopy", 2020.

### Submitted Article

— I. Gharib, and M. Sawan, "Microfluidic Valve Arrays for Drug Delivery in Organ-On-Chips", IEEE Engineering in Medicine and Biology Society Conference (EMBC), 2020.

### Published Article

— I. Gharib, and M. Sawan, "High-efficiency LED Driver for Short Fluorophores Lifetime Biosensing Applications", IEEE International New Circuits and Systems Conference (NEW-CAS), 2019.

The present thesis is made up of four parts. The first one presented in Chapter 3 exhibits the fabricated instrument as a first prototype to validate the main basic ideas of the proposed method. Since this new method is based on fluorescence lifetime measurement, a light excitation with a short fall time is required to make this method possible. However, the most existing light source for short excitation are expensive and more difficult to be integrated in wearable instruments. To resolve this issue, Light emitting diodes (LED) can be used as an alternative solution because of their portability and lower cost. Nevertheless, LEDs fall time is in general in the average of 20 ns which is not enough for the most used fluorophore. Thus, in Chapter 4 we present a novel LED driver to deliver short pulse excitation by reducing significantly the optical fall time.

Instead of working with only one 3D environment, the proposed instrument can be used for systems consisting of large number of microfluidic rooms to make possible multiple independent imaging measurements at the same time and in one chip. However, a large number of micro-fluidic channels will be needed to access various specific locations. Thus, in Chapter 5 we present an embedded on-chip controller to drive the expected large number of switching valves with less number of off-chip control components. Also, the utility of this system on Organs-On-Chip (OOC) is presented in this chapter.

Chapter 6 presents a designed electronic system to make this fabricated instrument fully wearable in terms of power, communication and automatic calibration.

## CHAPTER 2 LITERATURE REVIEW

### 2.1 Fluorescence Lifetime Method

#### 2.1.1 Principle and Theory

Fluorescence lifetime method is one of the recent techniques in the arsenal of medical imaging and biological sensing. Fluorescence is a physical phenomenon that occurs when a fluorophore molecule absorbs a photon of appropriate energy and an emission light is resulting. This process is due to a chain of photophysical events that manifest, such as internal conversion or vibrational relaxation, intersystem crossing (from singlet state to a triplet state), as shown in the Jablonski diagram for organic molecules (Fig 2.1) [25].

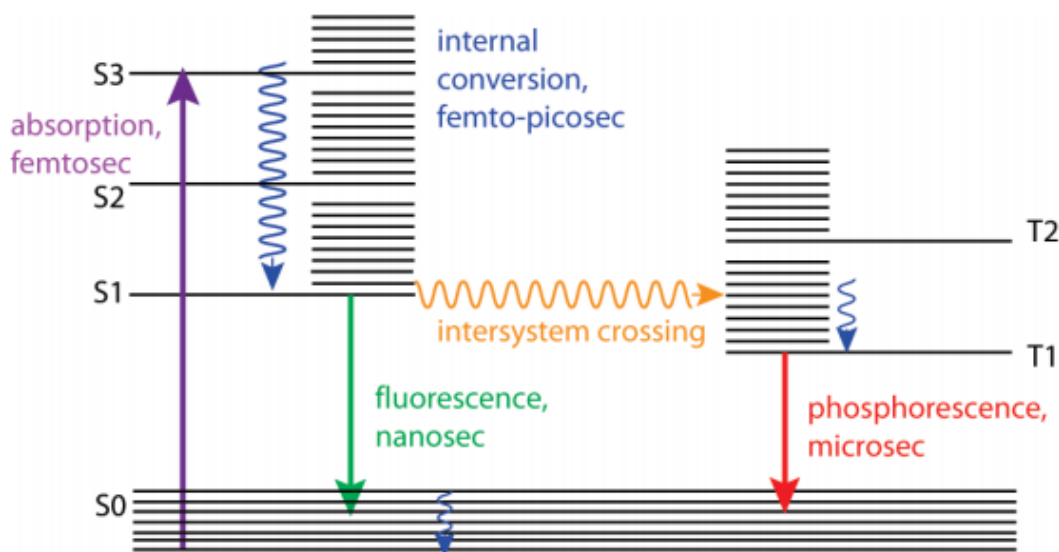


Figure 2.1 Jablonski diagram and a time scale of photophysical processes for organic molecules [25].

When the molecule is excited, the electrons at fundamental state  $S_0$  reach the excited levels ( $S_1, S_2, \dots$ ) without change in the spin configuration, then the return of the electrons to the fundamental state generates the fluorescence. A shift between absorption wavelength and emission wavelength is observed (Fig 2.2), called Stokes shift as reference to the English physicist George Gabriel Stokes who describes this phenomenon for the first time [26].

In an ideal case of identical independent fluorescence emitters, the fluorescence decay is a

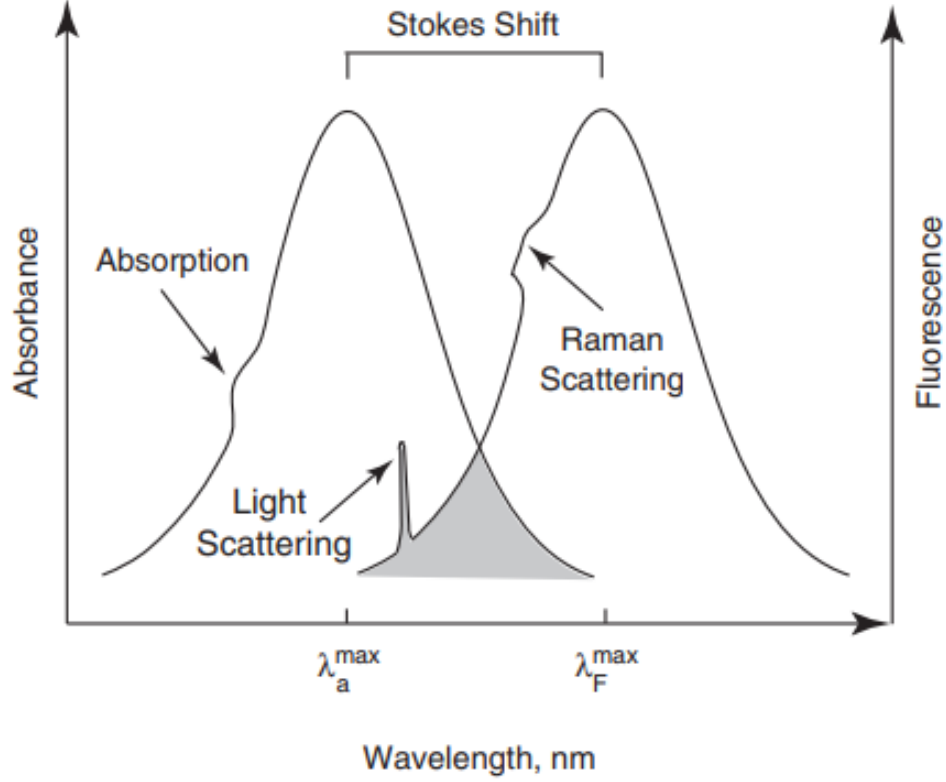


Figure 2.2 Typical absorption and fluorescence emission spectra. The fluorescence spectrum is located at longer wavelengths with respect to the absorption spectrum. The distance between their band maxima is called the Stokes shift [26].

single exponential function of time  $t$  expressed by Eq. (2.1)

$$F(t) = F_0 \exp(-t/\tau) \quad (2.1)$$

where  $F_0$  is the initial intensity at time  $t = 0$ . The time constant  $\tau$  is called the fluorescence lifetime, it is determined as being inversely proportional to the sum rate constants of a radiative process  $k_f$  and the non-radiative processes  $k_{nr}$  collectively known as quenching (Eq. (2.2)) [25].

$$\tau = \frac{1}{k_f + k_{nr}} \quad (2.2)$$

### 2.1.2 Techniques

#### Time-Domain Method

Time-domain data acquisition methods is commonly used to determine the fluorescence lifetime of fluorophores. The sample (a cuvette, cells, or tissue) is excited with a short pulse of

light and a time-correlated single photon counting (TCSPC) is used as fluorescence detection method which simplify data collection and enhance quantitative photon counting [27]. The fluorescence lifetime is calculated from the slope of the decay curve obtained from TCSPC method and resolved according to Eq. (2.1). This calculation can be done by using fitting algorithms, with least-squares curve method being the most common.

### Frequency-Domain Method

In frequency domain technique (Fig. 2.3), the incident light is sinusoidally modulated at high frequencies. In this configuration, the emission occurs at the same frequency as the incident light, but it experiences a phase delay and change in the amplitude  $M$  relative to the excitation light (demodulation) due to the loss of electron energy (Stokes' shift) between excitation and emission [28].

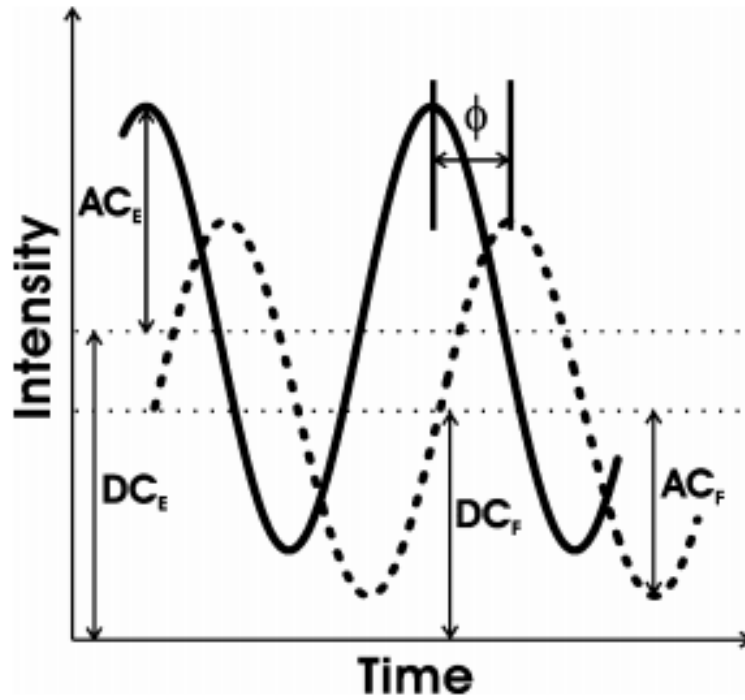


Figure 2.3 Relative phase shift ( $\phi$ ) and modulation of the excitation (subscript E) and emission (subscript F) light in frequency domain fluorescence spectroscopy. AC and DC indicate the amplitude and offset of the respective waves [28].

The lifetime  $\tau_M$  can be determined from this modulation via Eq. (2.3)

$$M = \frac{1}{\sqrt{1 + (\omega\tau_M)^2}} \quad , \quad M = \frac{(AC)_E/(DC)_E}{(AC)_F/(DC)_F} \quad (2.3)$$

where  $\omega$  is the light angular modulation frequency.

### Time-Resolved Fluorescence Anisotropy

In addition to measuring fluorescence lifetime, time-resolved methods are instrumental in identifying other important characteristics of fluorophores such as the rotation of molecules in different media. In the fluorescence anisotropy (also called fluorescence polarization) technique, the fluorophore is irradiated with linearly polarized light using a polarization filter. The resultant fluorescence intensity is measured through another polarization filter placed in front of the detector and oriented in the parallel and perpendicular directions to the incident polarized light. Fluorescent anisotropy  $r$  can then be determined from Eq. (2.4)

$$r = \frac{F_{\parallel} - F_{\perp}}{F_{\parallel} + 2F_{\perp}} \quad (2.4)$$

where  $F_{\parallel}$  is the fluorescence intensity with polarization filters parallel to each other and  $F_{\perp}$  with perpendicular orientation.

Equation (2.5) proposed by Francis Perrin [29], describes that anisotropy depends on fluorescence lifetime and rotational correlation time of the molecules.

$$\frac{r^0}{r} = 1 + \frac{\tau}{\theta_r} \quad (2.5)$$

where  $r^0$  is limiting anisotropy measured in solid glycerol to prevent molecular movement,  $\tau$  is fluorescence lifetime,  $\theta_r$  is rotational-correlation time of a macromolecule.

This equation reveals the dependency of fluorescence lifetime on the molecular rotation. Thus, This technique help to eliminate this effect to find true fluorescence lifetime free from polarization artifacts, by setting an appropriate optical calibration.

#### 2.1.3 Processes Affecting Fluorescence Lifetime

##### Förster Resonance Energy Transfer (FRET)

Förster resonance energy transfer (FRET), fluorescence resonance energy transfer (FRET), resonance energy transfer (RET) or electronic energy transfer (EET) is a mechanism de-



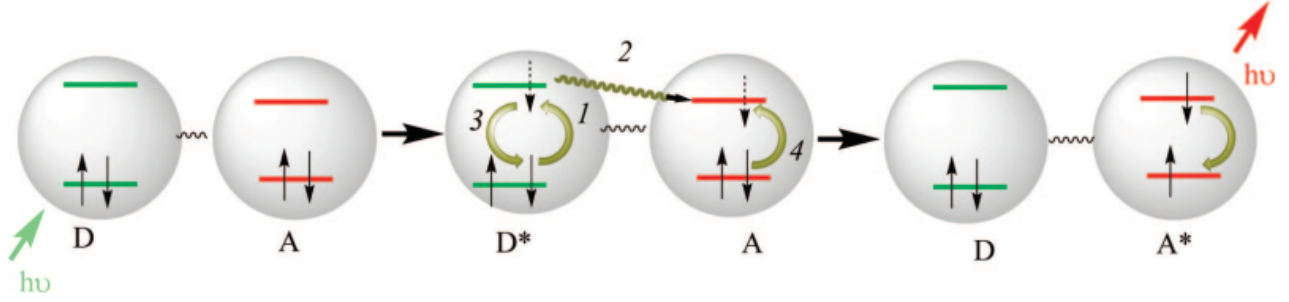


Figure 2.4 Diagram of FRET. Upon excitation by the photon, the electron of the donor is promoted to the excited state (1), followed by the energy transfer to the acceptor excited orbital (2), simultaneous return of the excited electron back to the ground state (3), and excitation of an acceptor (3) [25].

scribing energy transfer between two light sensitive molecules (chromophores). A donor chromophore, initially in its electronic excited state, may transfer energy to an acceptor chromophore through nonradiative dipole–dipole coupling (Fig. 2.4).

The efficiency of this energy transfer is inversely proportional to the sixth power of the distance between donor and acceptor, making FRET extremely sensitive to small changes in distance [25]. This condition is often achieved if two identical fluorophores form a FRET pair (homoFRET), in which case the overall lifetime decreases if the two fluorophores are close, and expressed by Eq. (2.6).

$$E_t = 1 - \frac{\tau_{da}}{\tau_d} \quad (2.6)$$

where  $\tau_{da}$  is the fluorescence lifetime of the donor in the presence of the acceptor and  $\tau_d$  is the lifetime of the donor without the acceptor. This energy transfer  $E_t$ , can be expressed using Förster Eq. (2.7).

$$E_t = \frac{R_0^6}{R_0^6 + r^6} \times 100 \quad (2.7)$$

where  $r$  is the distance between two fluorophores and  $R_0$  is Förster radius where half of the energy is transferred.

### Dexter Electron Transfer

Dexter electron transfer (also called Dexter electron exchange and Dexter energy transfer) is a fluorescence quenching mechanism in which an excited electron is transferred from one molecule (a donor) to a second molecule (an acceptor) via a non radiative path [25] (Fig. 2.5).

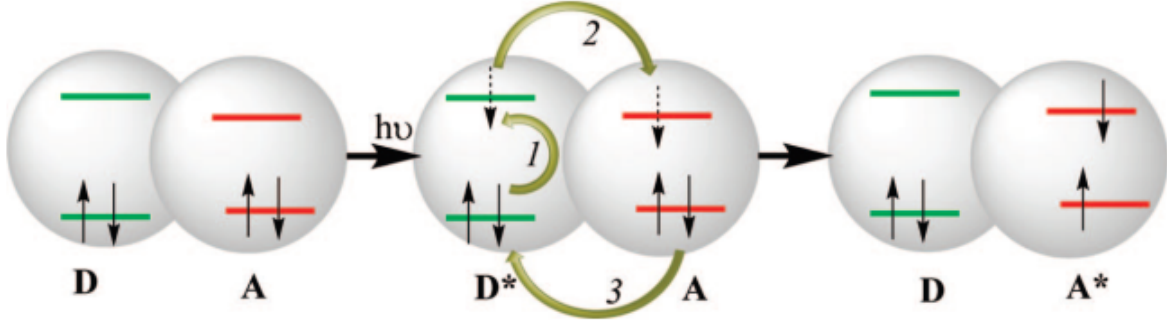


Figure 2.5 Dexter electron transfer process, where the distance between acceptor and donor is shorter [25].

This process requires a wavefunction overlap between the donor and acceptor, which means it can only occur at short distances.

The main difference between FRET and Dexter Electron Transfer is that phenomenon happens at a distance between two fluorophores shorter than the Förster radius. For FRET, the Förster radius  $R_0$  is given by Eq. (2.8).

$$R_0 = 0.211(k^2 n^{-4} \Phi_D J)^{1/6} \quad (2.8)$$

where  $n$  is refractive index,  $k^2$  is orientation factor,  $\Phi_D$  is quantum yield of the donor, and  $J$  is the spectral overlap integral and given by Eq. (2.9).

$$J = \int_0^\infty F_D(\lambda) \lambda^4 d\lambda \quad (2.9)$$

where  $\lambda$  is wavelength (nm), and  $F_D(\lambda)$  is the fluorescence intensity.

While for Dexter Electron Transfer,  $J$  is given by Eq. (2.10).

$$J = \int_0^\infty F_D(\lambda) \epsilon_A(\lambda) d\lambda \quad (2.10)$$

where  $\epsilon_A(\lambda)$  is the molar absorptivity of the acceptor at a given  $\lambda$ .

### Photon Reabsorption

One of the major advantages of fluorescence lifetime imaging is the independence of the lifetime from concentration. This statement is however only valid for a certain range of concentration in which fluorophores do not interact either chemically or photonically. It is also essential that a minimum concentration threshold be attained to provide sufficient fluorescent signal for lifetime measurement [25]. Figure 2.6 present an example of fluorophore

concentration can affect the value of fluorescence lifetime for rhodamine 6G [30].

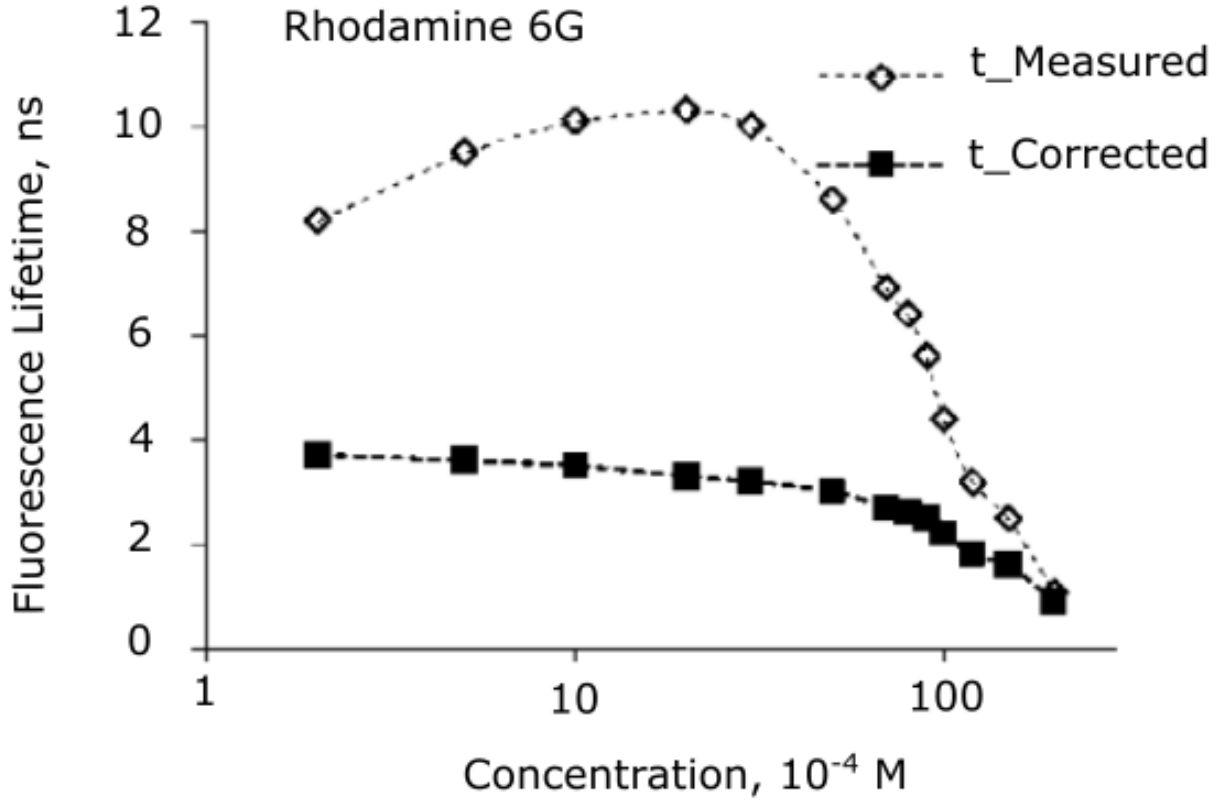


Figure 2.6 Fluorescence lifetime of rhodamine 6G in methanol (molecular fluorescence lifetime is  $\sim 4$  ns) as a function of the concentration of the dye, for measured lifetime, and measured lifetime corrected for self-absorption. Adapted from [30].

This reabsorption process phenomenon can be modelled by Eq. (2.11) [31].

$$\tau_{ra} = \frac{\tau}{1 - a\Phi} \quad , \quad a = f(J, c) \quad (2.11)$$

where  $a$  is the probability of reabsorption as a function of the overlap between emission and absorption ( $J$ ) spectra and concentration of the fluorophore ( $c$ ) and  $\Phi$  is quantum yield.

## 2.2 3D Sensing and Imaging

### 2.2.1 Laser Scanning Confocal Microscopy (LSCM)

Many technologies have been developed and investigated for optical 3D imaging and molecules tracking. Laser Scanning Confocal Microscopy (LSCM) [32] (Fig. 2.7 and Fig. 2.8) is one of the first techniques used for this purpose which uses pinhole aperture that ensures that light reaching the detector comes only from the equivalent (confocal) point in the specimen where the excitation light was focused. Confocal microscopy is a form of fluorescence microscopy that sharpens the images collected by visualizing the light from only one plane of focus. This allows for the collection of multiple focal planes in what is called a z-stack, which provides three-dimensional data.

(LSCM) is an alternate method available for obtaining the optical equivalent of thin fluorescent sections. The optical principle of confocal microscopy is simple, but a large investment in hardware and software is required. LSCM optically isolates fluorescence emission to the image plane, providing a means of obtaining high-resolution images of photoreceptor cells in thick sections. The image can be sequentially compiled, pixel by pixel, by recording the fluorescence intensity at each position.

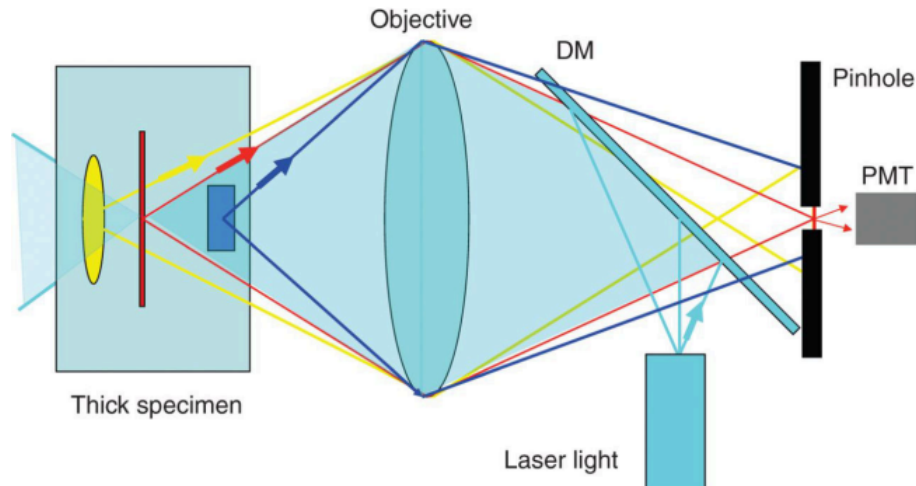


Figure 2.7 Principle of operation of a laser scanning confocal microscope. Laser light is focused on the thick specimen by reflection from the dichroic mirror (DM) and the objective lens. The laser excites fluorescence throughout the specimen that passes through the DM and is focused onto the image plane. A pinhole only allows light from the confocal plane of the specimen to reach the photomultiplier tube (PMT) [33].

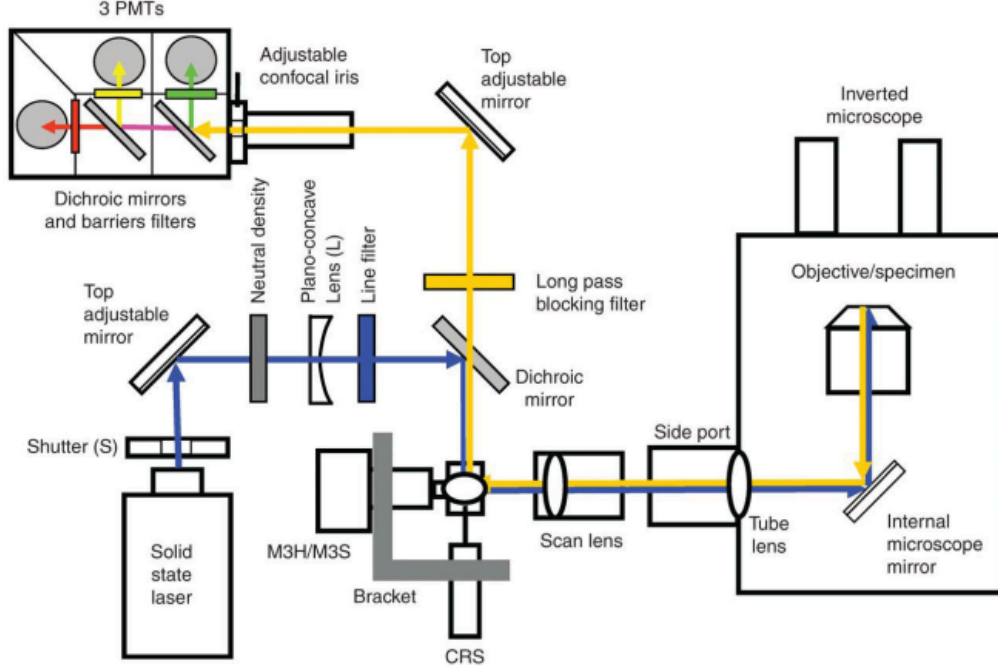


Figure 2.8 Basic elements of a laser scanning confocal microscope. Laser light is directed to the scan mirrors via a dichroic mirror. The laser is scanned across the specimen by the scan mirrors and the returning emitted fluorescence is descanned by the same mirrors and transmitted by the dichroic mirror. The fluorescence passes through the barrier filter and is focused on to the pinhole (adjustable iris) before reaching the PMTs. Additional dichroic mirrors can be used to separate fluorescence wavelengths [33].

### 2.2.2 Two-Photon Fluorescence Microscopy (TPFM)

Two-Photon Fluorescence Microscopy (TPFM) [34] (Fig. 2.9) is another type of laser scanning microscopy which is based on a quantum phenomenon that a fluorescence can occur when a fluorophore absorbs two photons essentially simultaneously with less energy. Thus, with the two-photon mode of excitation, the fluorescence occurs only in the intersection point of the two excitations, which eliminates the need of a pinhole. This technique and that of LSCM, however, suffer from the diffraction limits imposed by the wave nature of light which limits the resolution between closely opposed sources of light. Equations (2.12) and (2.13) respectively describe the Ernst Abbe's diffraction limit expression for XY and Z resolutions.

$$R_{XY} \approx 0.61\lambda/N.A \quad (2.12)$$

$$R_Z \approx 1.4\lambda\eta/(N.A)^2 \quad (2.13)$$

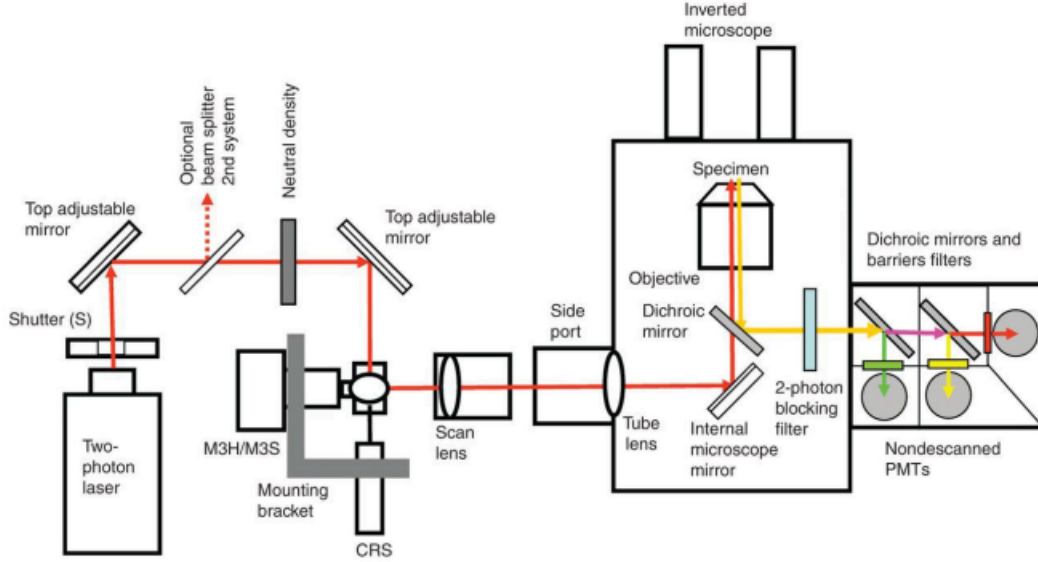


Figure 2.9 Basic elements of a two-photon microscope. PMTs detectors do not require pin-holes or focused images and are located immediately below the objective [33].

where  $\lambda$  is the wavelength of the emission light,  $\eta$  is the refractive index of the mounting medium, and  $N.A$  is the numerical aperture of the objective lenses.

### 2.2.3 Stimulated Emission Depletion (STED) microscopy

Super-resolution imaging techniques named photoactivation localization nanoscopy [35][36] have been developed to mitigate the resolution limitations of the aforementioned techniques. STED microscopy is one of several types of super resolution microscopy techniques that have recently been developed to bypass the diffraction limit of light microscopy to increase resolution [33]. STED is a deterministic functional technique that exploits the non-linear response of fluorophores commonly used to label biological samples in order to achieve an improvement in resolution, that is to say STED allows for images to be taken at resolutions below the diffraction limit.

It creates super-resolution images by the selective deactivation of fluorophores, minimising the area of illumination at the focal point, and thus enhancing the achievable resolution for a given system (Fig. 2.10).

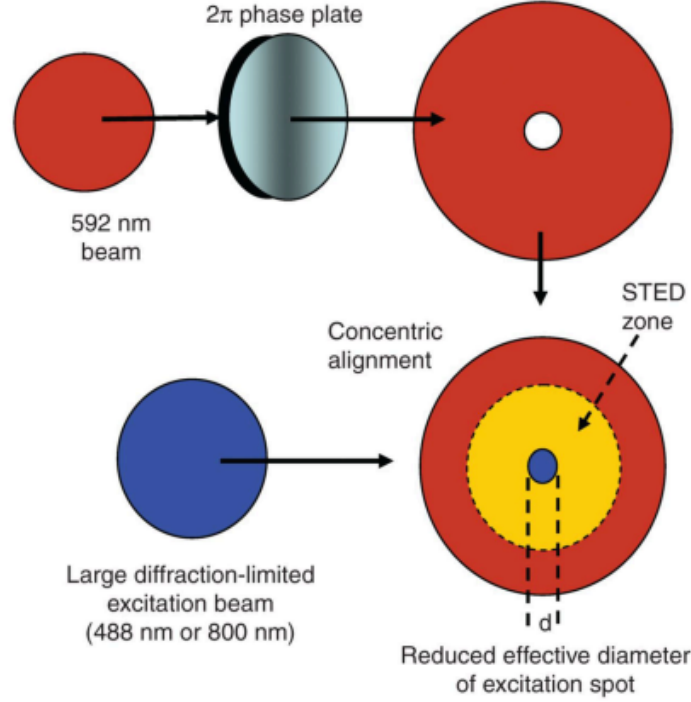


Figure 2.10 Creation of reduced excitation spot for STED microscopy. The STED (592-nm) laser beam (red) is shaped by a 2 phase plate into a doughnut and concentrically overlaid with the 488- nm excitation laser (blue). The process of STED occurs in the yellow zone to reduce the zone of fluorescence. Increased STED laser power decreases the diameter,  $d$ , of the excitation spot [33].

#### 2.2.4 LED-CT Scan

CT scan is a technique that can be used for 3D bio-chemical sensing by using light absorbance, and it's based on parallel scan lines as shown in Fig. 2.11 [37]. Assume  $f(x, y)$  as a distribution of absorbance on  $xy$  plane.  $x'y$  plane has an angle of  $\theta$  with respect to  $xy$  plane on  $z$  axis. When parallel light is irradiated along  $y$ , the projected distribution of absorbance along  $x$  can be calculated as

$$R(\theta, x') = \int_{-\infty}^{\infty} f(x, y) dy' \quad (2.14)$$

$f(x, y)$  can be found as

$$f(x, y) = \frac{1}{2\pi} \int_0^{2\pi} \left( \frac{1}{2\pi} \int_0^{\infty} e^{i\omega(x \cos \theta + y \sin \theta)} G(\theta, \omega) \omega d\omega \right) d\theta \quad (2.15)$$

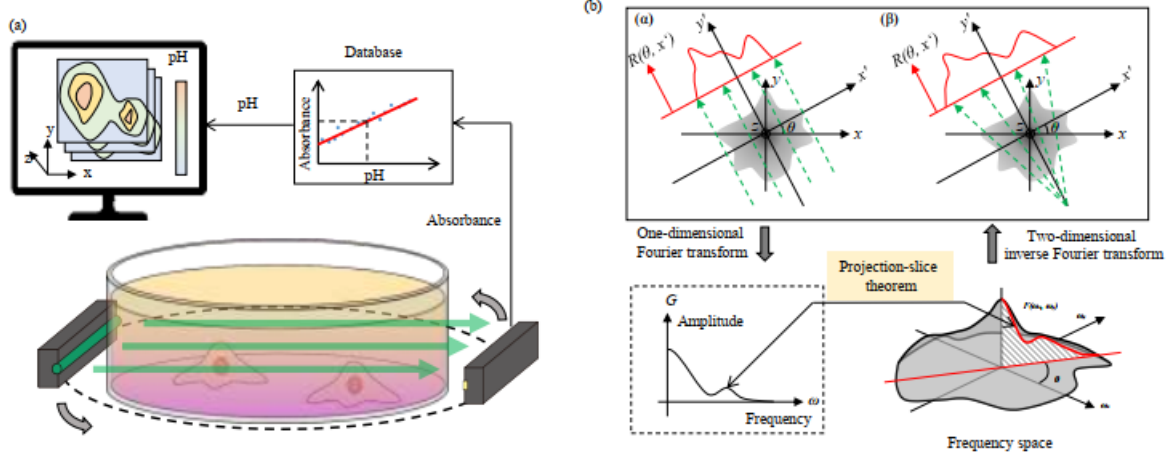


Figure 2.11 Measure of pH distribution by computed tomography (CT) scan. (a) The concept of the system and (b) the algorithm of CT scan using the projection-slice theorem by ( ) parallel beam or ( ) fan beam [37].

where  $G(\theta, \omega)$  is the Fourier transformation of  $R$  about  $x'$

$$G(\theta, \omega) = \int_{-\infty}^{\infty} R(\theta, x') e^{-i\omega x'} dx' \quad (2.16)$$



## CHAPTER 3 3D INTERFEROMETRIC FLUORESCENCE MICROSCOPY

The following sections in this chapter are the reproduction of upcoming article [38] and the subject of a submitted patent [39].

### 3.1 Basic Principle

This present work exploits the Fluorescence Lifetime Imaging Microscopy (FLIM) technique in a way that only two scanning planes are enough to get a full 3D sensing of cells sample. FLIM is an imaging technique that based on adding fluorescent indicator to the cells sample and exciting it by a short-light pulse. After the excitation source is turned off the light emission of the fluorescent indicator decay by a specific lifetime  $\tau$ . Any change in  $\tau$  value gives information about biochemical specifications change in the sample [40] [41] [42]. For a heterogeneous medium of pH for example, the fluorescence emission decay behaves in a multi-exponential instead of mono-exponential for homogeneous medium [43]. In case of heterogeneous medium, the resulting fluorescence dynamics is characterized by Eq. (3.1).

$$F(t) = \sum_{j=1}^N A_j \exp(-t/\tau_j) \quad (3.1)$$

where  $A_j$ , and  $\tau_j$  are the amplitudes and decay times of the  $N$  exponential components of the fluorescence decay. To determine These parameters  $A_j$  and  $\tau_j$ , many fitting algorithms have

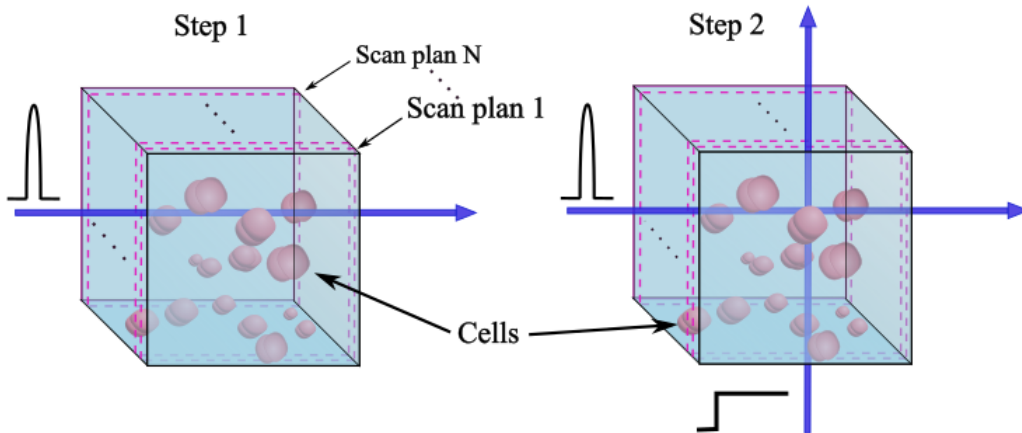


Figure 3.1 Principle of 2-scanning plans: Step 1 provides the information of the segment without arrangement, thanks to the interference; In step 2, each pixel is associated with its corresponding lifetime.

been developed for this purpose, such as Fast Fitting Algorithm [44], Maximum-Likelihood Method [45] and Compressive Sensing Estimation [46]. The principle work of the new method presented in this paper is based on two scanning planes (x,y) and (y,z) as it is shown in Fig. 3.1. In step 1, the sample is excited with a short pulse in the x direction throughout a chosen segment k. From this step we get the fluorescence decay described in Eq. (3.2).

$$F(t) = \sum_{j=1}^N A_{k,j} \exp(-t/\tau_{k,j}) \quad (3.2)$$

where N is the number of discrete pixels  $P_{k,j}$  throughout that segment k, and with fitting we can determine the couples  $\{A_{k,j}, \tau_{k,j}\}_{j \in [1,N]}$ .

At that level we don't know the associated parameter  $\tau_{k,j}$  for each pixel  $P_{k,j}$ , we only know the couple of  $\{\tau_{k,j}\}_{j \in [1,N]}$  that necessary exist in this segment without any arrangement. In step 2, we excite firstly with a continuous beam with intensity A in z direction throughout segment l and then followed by a short pulse like in step 1. In this second step, the resulting fluorescence decay is described by Eq. (3.3).

$$F(t) = \sum_{j=1, j \neq l}^N A_{k,j} \exp(-t/\tau_{k,j}) + A'_{k,l} \exp(-t/\tau_{k,l}) + A' \quad (3.3)$$

where  $A'_{k,l}$  and  $A'$  are the new resulting intensities that follow Eq. (3.4).

$$A'_{k,l} + A' = A_{k,l} + A + A_{interference} \quad (3.4)$$

where  $A_{interference}$  is the term that occur because of the phenomena of interference that happens in pixel  $P_{k,l}$  between the two beams.

The passage from step 1 to step 2 make us notice that  $A_{k,l}$  that is changing ( $A_{k,l}$  to  $A'_{k,l}$ ). That means that the related  $\tau_{k,l}$  is the exact lifetime that should be associated to the pixel  $P_{k,l}$ . By this way and by sweeping all the segment we will be able to determine the lifetime of every pixel. We should note that for the vertical excitation we use a continuous beam, because if we use instead a pulse excitation, we get in addition many other confusing lifetimes. While for the continuous beam we only get a shifting constant in our expression that we can filter easily. We should also note that no change will be happening to parameters  $\tau_{k,l}$  when we combine the vertical and horizontal beams, because lifetime does not depend on the amplitude of the beam but rather with the characteristics of the medium. The remain of this paper it to prove the two main points of this idea; The interference and the non-changing of lifetime while moving from step 1 to step 2. The phenomenon of interference occurs when two monochromatic beams with the same frequency superpose to form a resultant wave of

greater or lower amplitude. The intensity of this resulting wave is given by Eq. (3.5).

$$I = I_1 + I_2 + 2\sqrt{I_1 I_2} \cos\left(\frac{2\pi}{\lambda} \delta\right) \quad (3.5)$$

where  $I_1$  and  $I_2$  are the two waves intensity,  $\lambda$  is the wavelength and  $\delta$  is the optical path difference.

The term on cosine should not be zero in order to have the interference, which means that

$$\frac{2\pi}{\lambda} \delta \neq \frac{\pi}{2} + k\pi, k \in \mathbb{Z} \quad (3.6)$$

Which also means

$$\frac{2}{\lambda} \delta - \frac{1}{2} \notin \mathbb{Z} \quad (3.7)$$

In our case we have  $\lambda = 470 \times 10^{-9}m$  and the optical path difference is in millimetre ( $\delta = a \times 10^{-3}m, 1 \leq a \leq 10$ ). Than we have

$$\frac{2}{\lambda} \delta - \frac{1}{2} = \frac{4 \times a \times 10^5 - 47}{2 \times 47} \quad (3.8)$$

which is not an integer, because we have an odd number divided by even number. Therefore, theoretically, the interference always occur whatever is the value of optical path difference throughout the scanning segment.

### 3.2 System Implementation

Figure 3.2 presents the instrumental structure of our system with different optical implementations. A DMD (Digital Micromirror Display) from Texas Instruments was used to orientate the beams in the desired direction, in order to get a full scan of the two planes with micro pixel patterning. Each micro mirror in the DMD have two positions  $+12^\circ$  and  $-12^\circ$ , which makes it the best choice for our application. Electronic control of the micro-mirrors provides fast and easy manner to drive the beams in the desired direction. The two plano-convex lenses are used as a collimator to convert the source rays to a parallel beam. One of the two light sources is used for continuous emission, while the second is used for pulse excitation. These two sources are placed in the focal point of the lens to make an infinite parallel projection. Mirrors  $M_1$  and  $M'_1$  are used to avoid direct lighting of DMD, in order to eliminate the light noises and residues coming from the sources.  $M_{2,3,4}$  and  $M'_{2,3,4}$  are used as a light filter for non-collimated rays, since there will be a small portion of non-parallel rays because of non-singularity of the light source. These two filters help to increase the precision of the

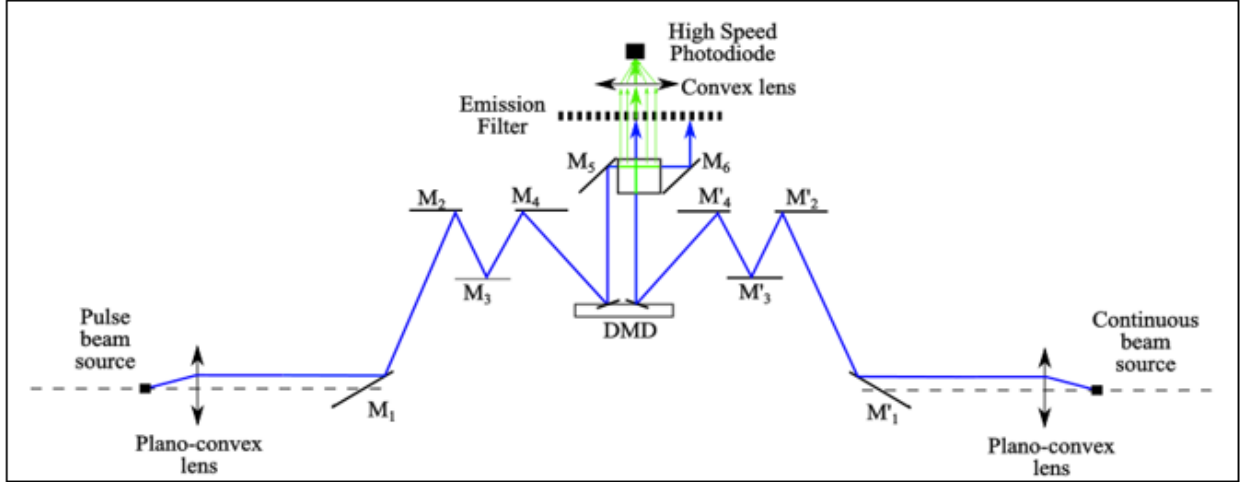


Figure 3.2 The system presentative schema with implemented optical devices. The horizontal and vertical scanning steps of the sample is insured by DMD. The Plano-convex lenses provide a collimated beam from the pulsed and the continuous sources. Mirrors  $M_5$  and  $M_6$  orientate the generated beams before and after the sample. The rest of the mirrors serves to filter the non-collimated rays and the light noises and residues coming from the sources. Emission filter blocks the direct beams coming from the source and only allow the fluorescence emission to get through. The convex lens picks up the resulting beams and drives it to the high-speed photodiode for measurement.

measurements. The purpose of mirror  $M_5$  is to convert the vertical beams coming from DMD to horizontal beams that will penetrate into the sample. Mirror  $M_6$  drives out the resulting beams after crossing the sample. Both  $M_5$  and  $M_6$  are tilted with  $45^\circ$ . The coordinate and the optimum inclination angle of every component are simulated and determined using Zemax OpticStudio software, and summarized in Table 3.1. The emission filter blocks the

Table 3.1 UNITS FOR COMPONENTS POSITION

Symbol	Quantity	Numerical Value
$d_{M1/M2}$	Horizontal distance between M1 and M2	20.04 mm
$h_{M1/M2}$	Vertical distance between M1 and M2	45 mm
$h_{M2/M3}$	Vertical distance between M2 and M3	11.23 mm
$h_{M4/DMD}$	Vertical distance between M4 and DMD	15 mm
$d_{DMD/M4}$	Horizontal distance between DMD and M4	6.68 mm
$d_{DMD/M1}$	Horizontal distance between DMD and M1	36.72 mm
$\theta_1$	Tilt angle of M1	31 degree

direct beams coming from the source and only allow the fluorescence emission to get through, to avoid false measurements. The convex lens picks up the resulting beams and drives it to

the high-speed photodiode for photons counting.

### 3.3 Experimental Setup

The fabrication of the instrument has been done by two types of 3D printing; Fused Deposition Modeling (FDM) for low cost parts that doesn't need high precisions and Stereolithography (SLA) which is most suitable for parts that require smooth surface finish and high level of feature detail, like the lens and DMD holders in our case. Figure 3.3 and 3.4 present respectively the assembly drawing of the instrument and the fabricated model with different optical parts.

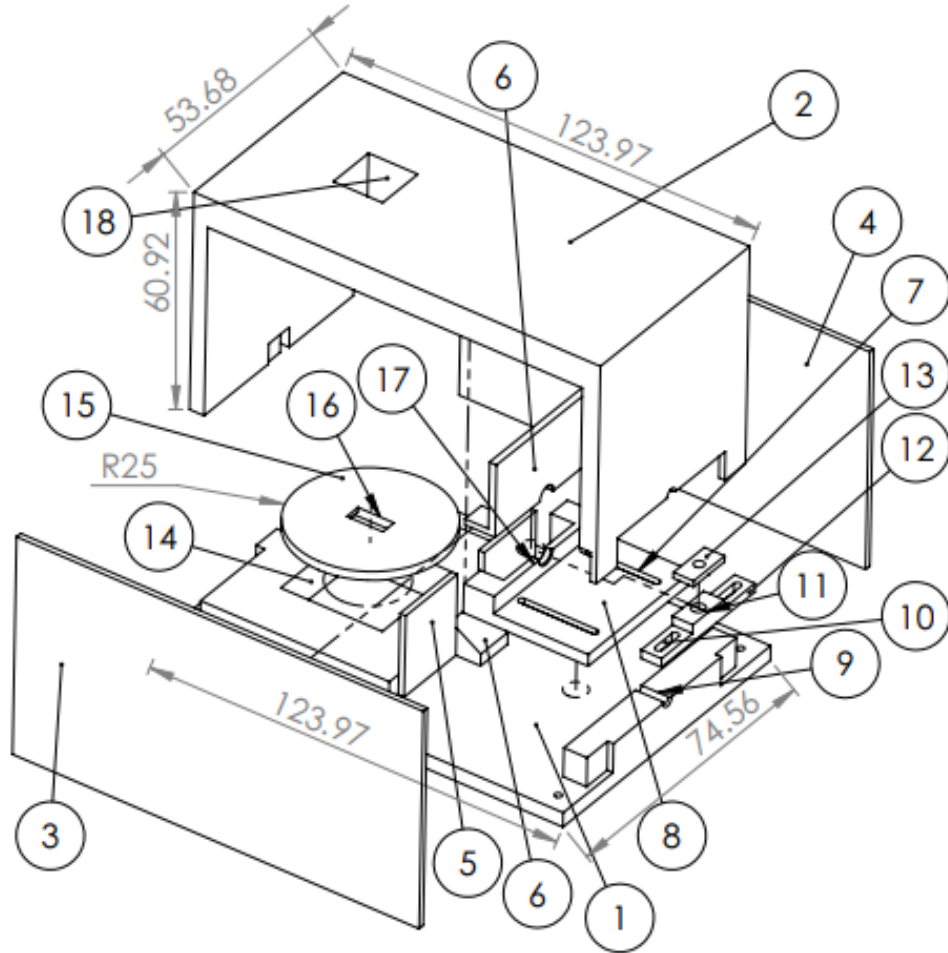


Figure 3.3 Assembly drawing of the proposed instrument designed by Solidworks software. 123.97 mm x 74.56 mm x 60.92 mm is its sizing.

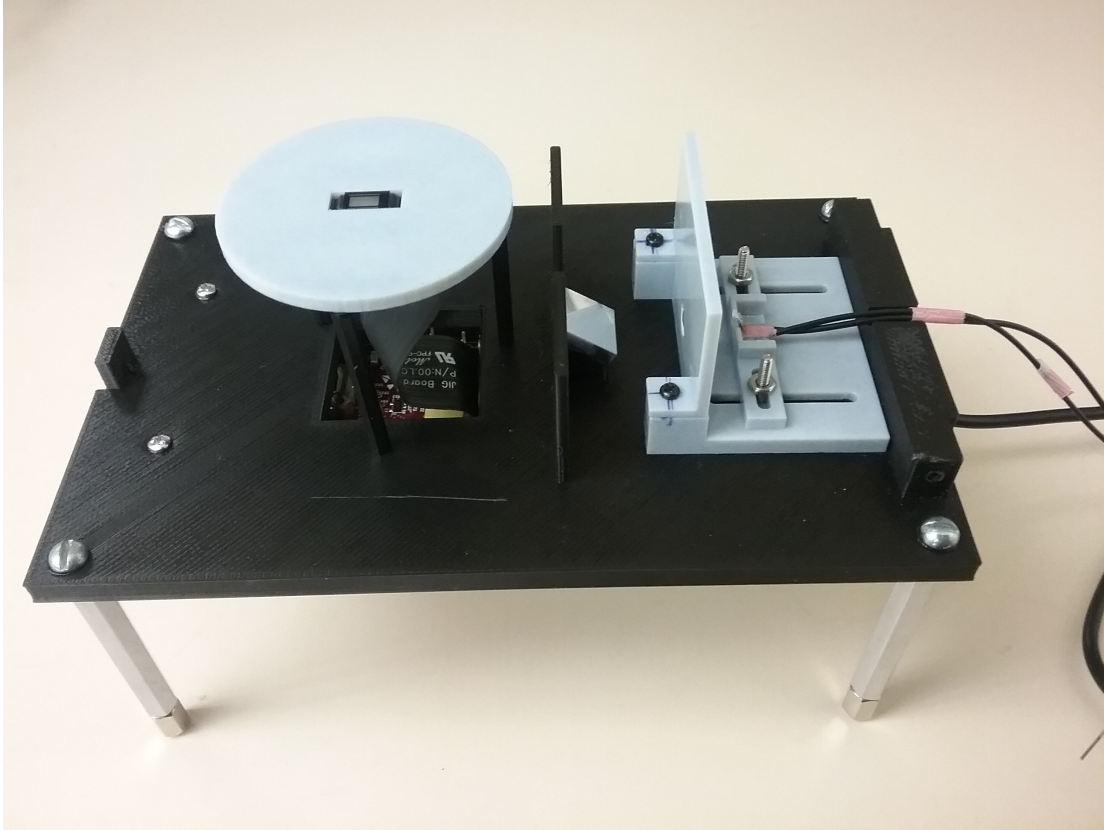


Figure 3.4 Photograph of the Instrument inside. The grey parts are fabricated by Stereolithography (SLA) while the others are made by Fused Deposition Modeling (FDM) for low cost.

The structure of this instrument is made up of a base table (1) with dimension of 123.97 mm x 74.56 mm, top cover (2), tow side covers (3) (4) to make a dark box, collimator (8) which is made up of lens and LED holder (6) (17) (11), non-desired rays' blocker (5), mirror site (6), DMD emplacement (15), and scan beams exit (18). The collimator and DMD holder were made by Stereolithography (SLA) since they require a high surface finish with micrometer precision. To have a good collimation, the center of the LED should be placed at the focal point of the plano-convex lens with a micrometer precision. Thus, as shown in Fig. 3.5, four micropositioners have been used for this purpose.

Tow for right/left movement and two for back/forward. The LED is connected to power supply and switched on. A white paper is placed in front of the collimator to visualize the light spot changing as the micro-positioners change the coordinates of the LED.

As a first model, we build this instrument with only one light source just to validate the idea of the system. While for a final instrument, two sources are required, one for continuous excitation and the second for pulses.



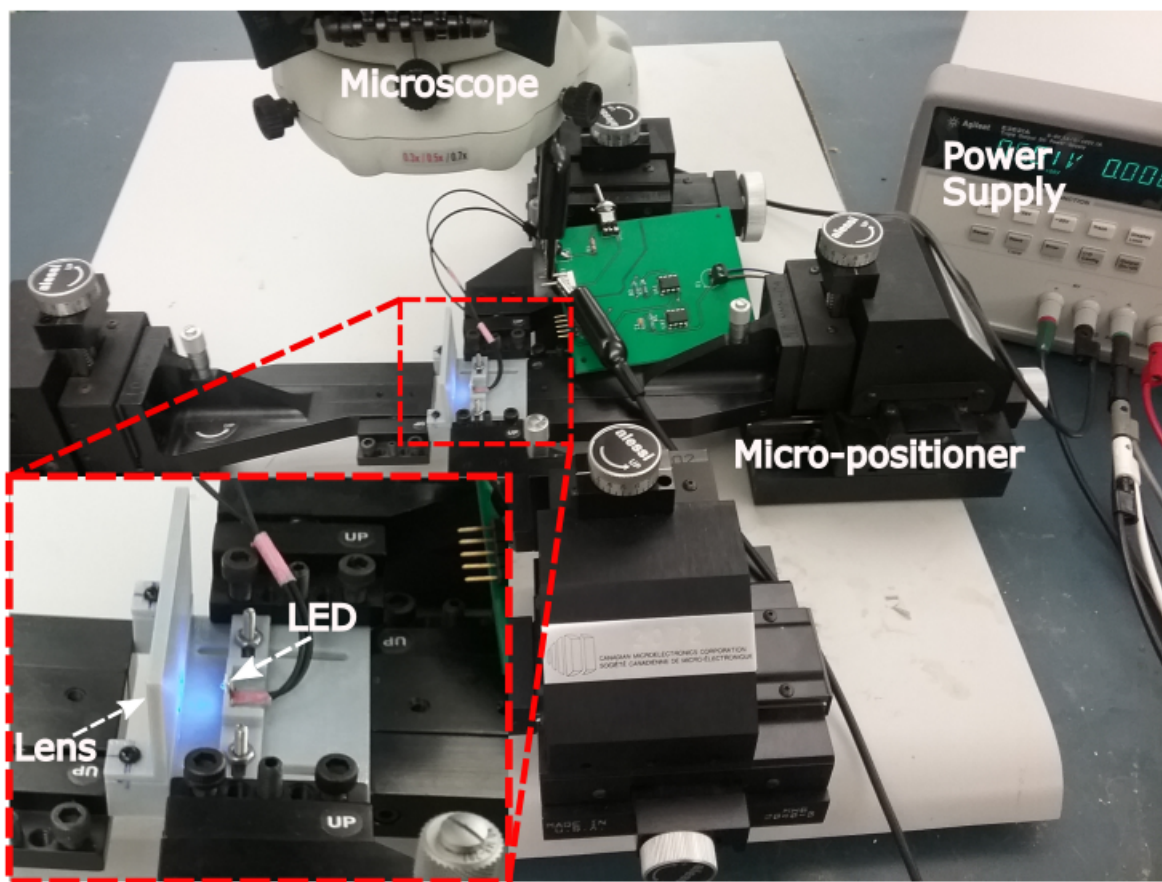


Figure 3.5 Collimator calibration by using four micro-positioners. Two for right/left and two for back/forward.

The chosen lens for the collimator is LENS PCX 6 X 9 VIS-NIR INK from Edmund Optics, with 6 mm in diameter and 9 mm for Effective Focal Length. For the first mirror we use MIRROR FS 1/10 WAVE UV AL 12.5 SQ, and FS 1/10 WAVE UV EN AL 5 SQ for the others.

The DMD used is DLP2000 (.2 nHD) with a future of 640x360 array of aluminum micrometer-sized mirrors in an orthogonal layout, 7.56-Micron micromirror pitch, 12° micromirror tilt relative to flat surface. To drive the DMD, we use DLP Light Crafter Display 2000 Evaluation Module (EVM) and Raspberry Pi 3B+ as an embedded host processor that provide a full control via I2C communication.

To measure the fluorescence intensity, we use Silicon Photodiode BPW 21 from OSRAM Opto-Semiconductors for Visible Spectral Range (350 nm to 820 nm) and LED GB PSLM31.13 with wavelength of 470 nm is used as an excitation source. Fluorescein is the chosen fluorophore for these measurements since it's a good indicator for pH in the neutral region.

To amplify the photodiode output signal and drive the LED, a Printed Circuit Board (PCB) was designed based on precision amplifiers OP27GPZ and a switching circuit as presented in Fig. 3.6.

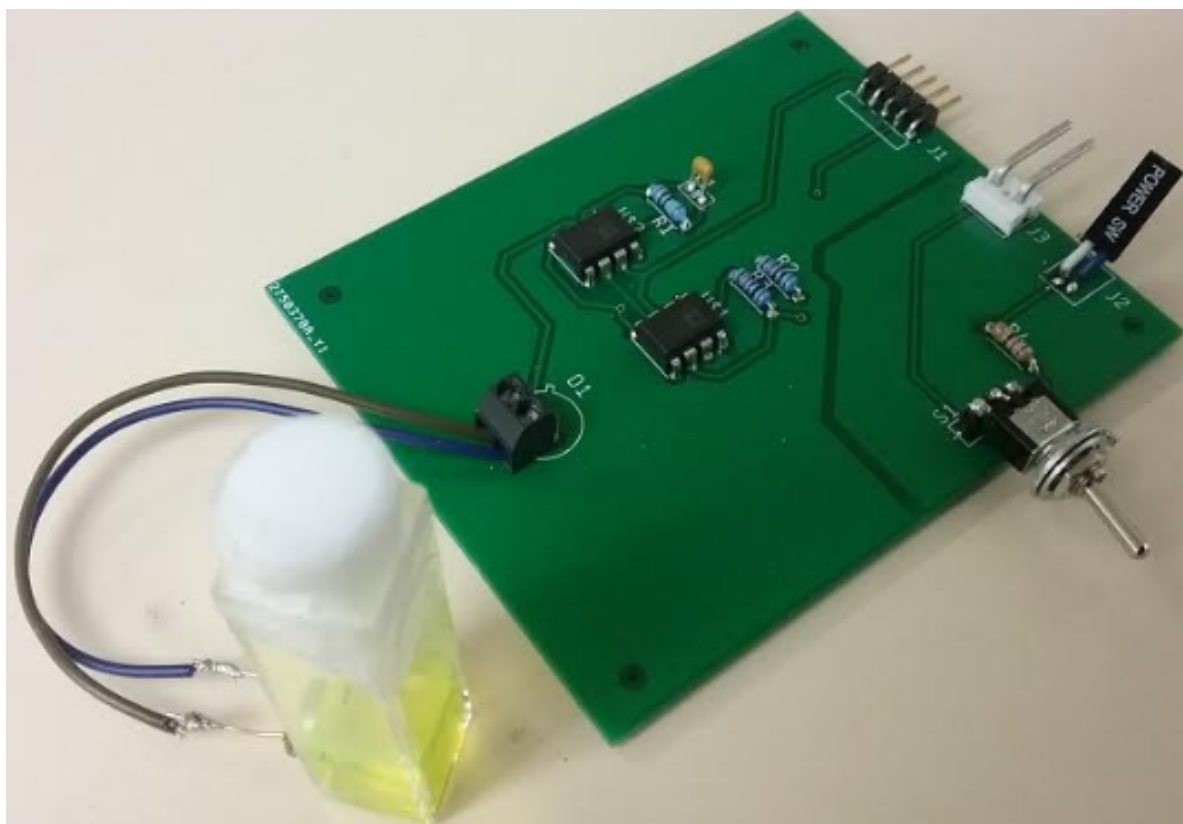


Figure 3.6 Fabricated PCB for photodiode output signal amplification and LED driving.



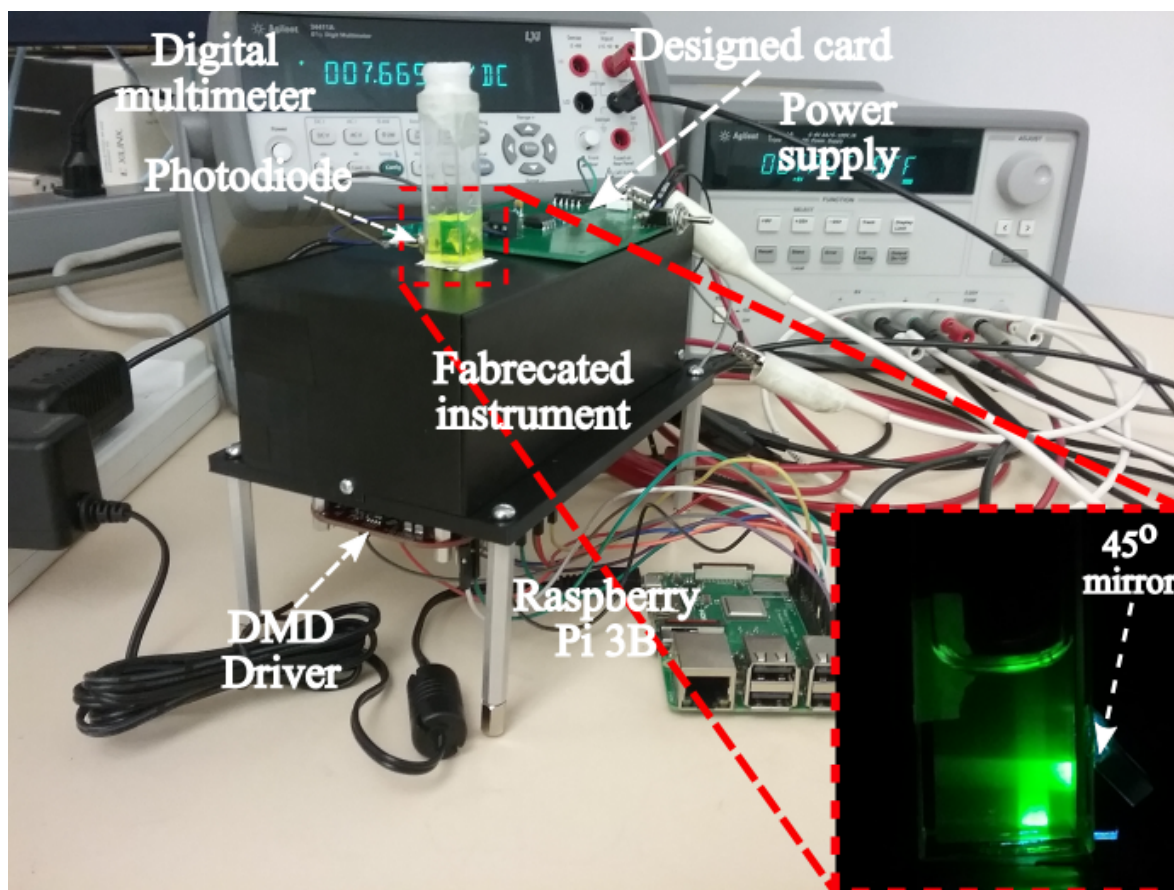


Figure 3.7 Experimental setup to test the instrument by measuring the interference between vertical and horizontal blue beam, inside a glass bowl contains fluorescein. In the right bottom is the obtained picture in the dark.

Figure 3.7 shows the experimental setup for our instrument where all parts are involved and connected with each other. In the right bottom is presented the obtained fluorescence emission image in the dark. Figure 3.8 shows the second setup to measure the fluorescein lifetime for two cases. The first one is for direct beam excitation and the second one is with combined two beams; direct and vertical beam. FLS920 Fluorescence Lifetime Spectrometer from Edinburgh Instruments Ltd was used to measure the fluorescence lifetime, which utilizes the technique of Time Correlated Single Photon Counting (TCSPC). 401.6 nm picosecond pulsed diode laser (77.4 ps) was used as excitation source. The results are obtained with the associated software that uses Non-Linear Least Square Fitting algorithm.

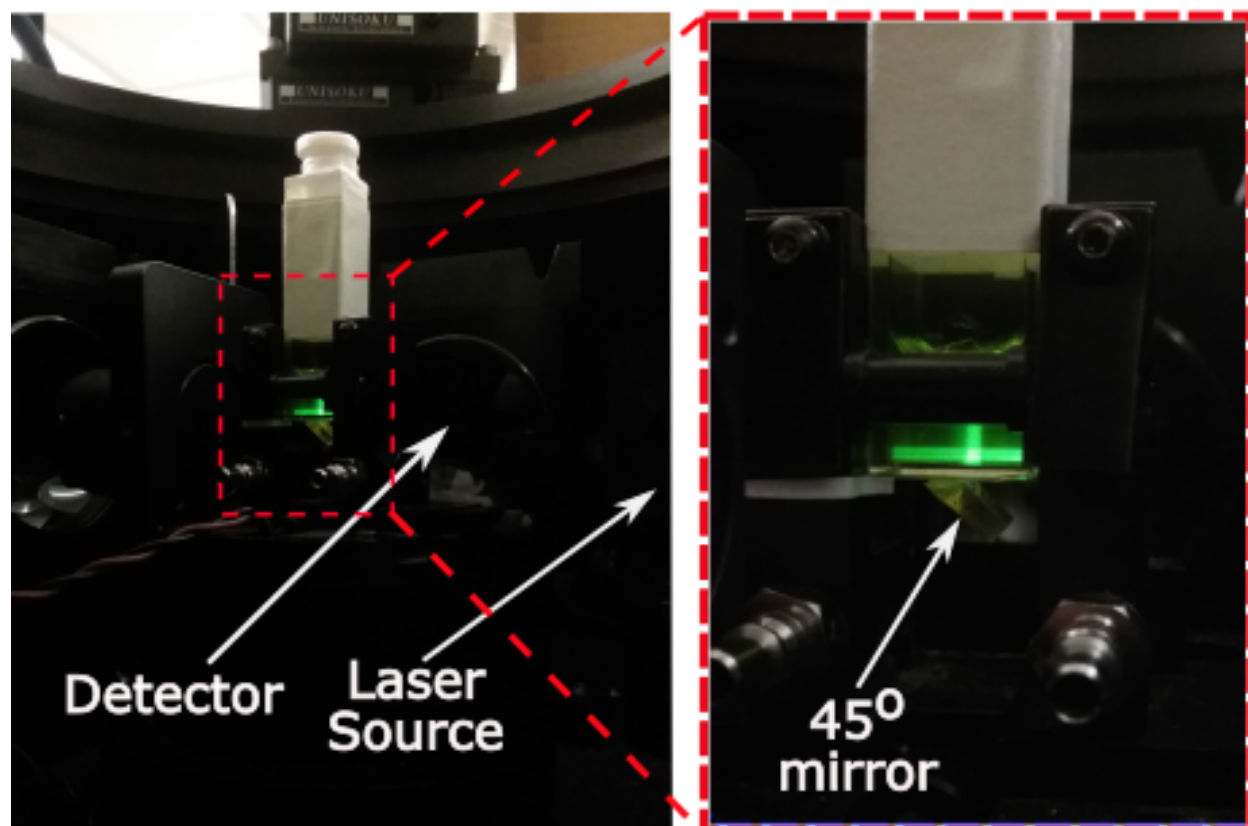


Figure 3.8 FLS920 Fluorescence Lifetime Spectrometer to measure fluorescein lifetime for direct and combined beams. 401.6 nm picosecond pulsed diode laser (77.4 ps) is used as excitation source.

For more sophisticated measurement, a hybrid optomicrofluidic platform was designed and proposed in Fig. 3.9 with the photograph of the fabricated chip. It is composed of a modular structure on the same chip for a fully integrated optofluidic platform. The bottom part with optical functionalities consists of a support plane with two mounted  $45^\circ$  mirrors (layer 1) and the top part realized by a PDMS layered structure with microfluidic functionalities (layer 2). Layer 3 serves as an upper cover. The layer 2 consist of a cubic room with 2.5mm in its width and a passive micro-mixer to create solutions at different fluorophore concentrations (mixing between fluorescein and EtOH). A serpentine-based micromixer was chosen to have a long path for efficient mixing.

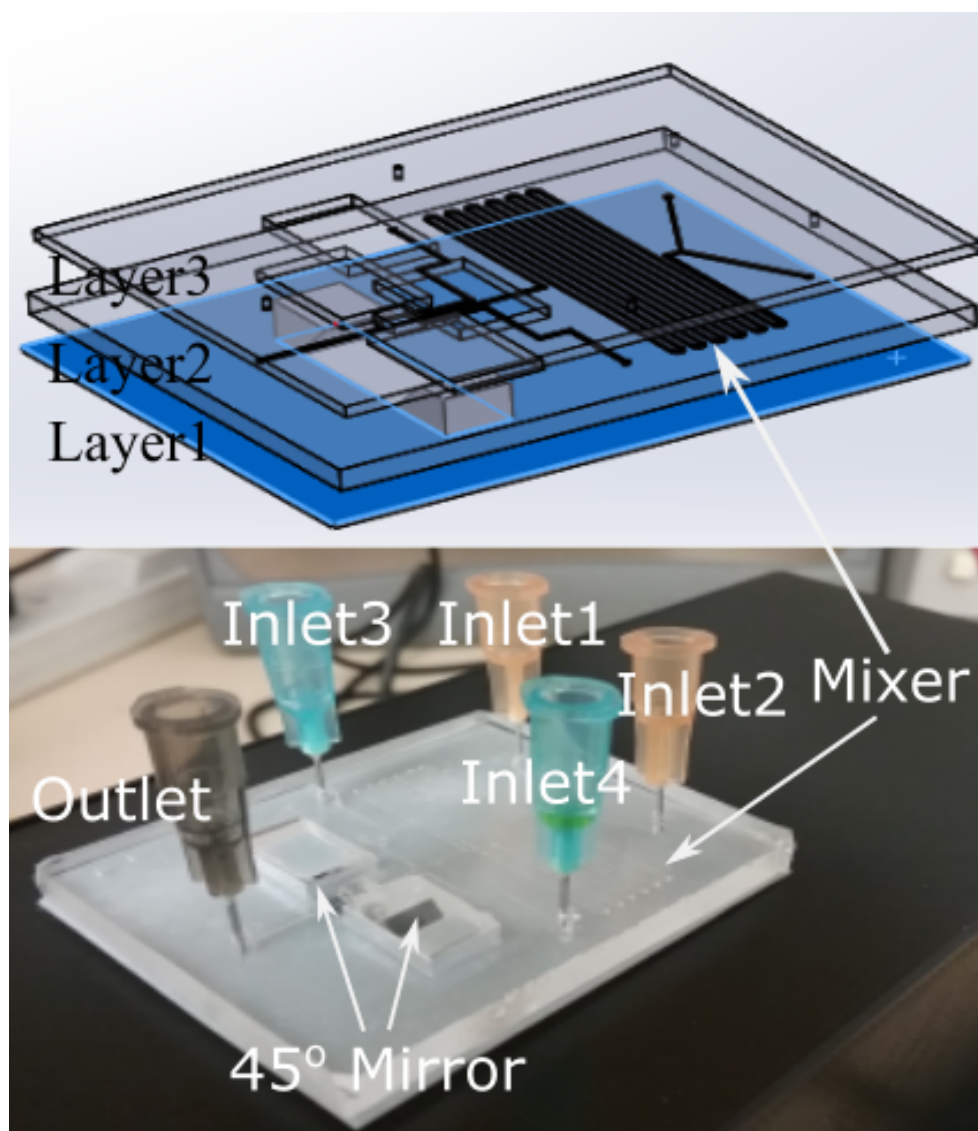


Figure 3.9 Modular structure of the proposed hybrid opto micro-fluidic platform with the photograph of the real fabricated chip.

The length of this path can be calculated by considering the time  $\tau = w^2/D$  that particles take to diffuse across the entire channel, where  $w$  is the width of the channel and  $D$  is the diffusion coefficient of the considered fluorophore. Thus, this length is  $l = V\tau$  where  $V = Q/w^2$  is the velocity and  $Q$  is the flow rate. Therefore, the minimum length of the serpentine for efficient mixing can be obtained as  $l = Q/D$  [47]. In our case, the diffusion coefficient of Fluorescein dye molecules is  $D \sim 4.25 \times 10^{-6} \text{ cm}^2/\text{s}$ . The dimension of the microfluidic channel was designed to be  $200 \mu\text{m} \times 200 \mu\text{m}$ . So, for a flow rate of  $Q = 0.5 \text{ ml/hr}$ , the length of the serpentine for a complete mixing should be at least  $L \sim Q/D = 32.68 \text{ cm}$ . 50 cm is the chosen value for the fabricated micro-mixer. Inlet 1,2 serve to fluorescein and EtOH injection and Inlet 3,4 serve to pH adjustment and variation, one for HCL and the second for NaOH.

### 3.4 Results

Obtained results for interference verification are presented in Fig. 3.10 and Fig. 3.11.

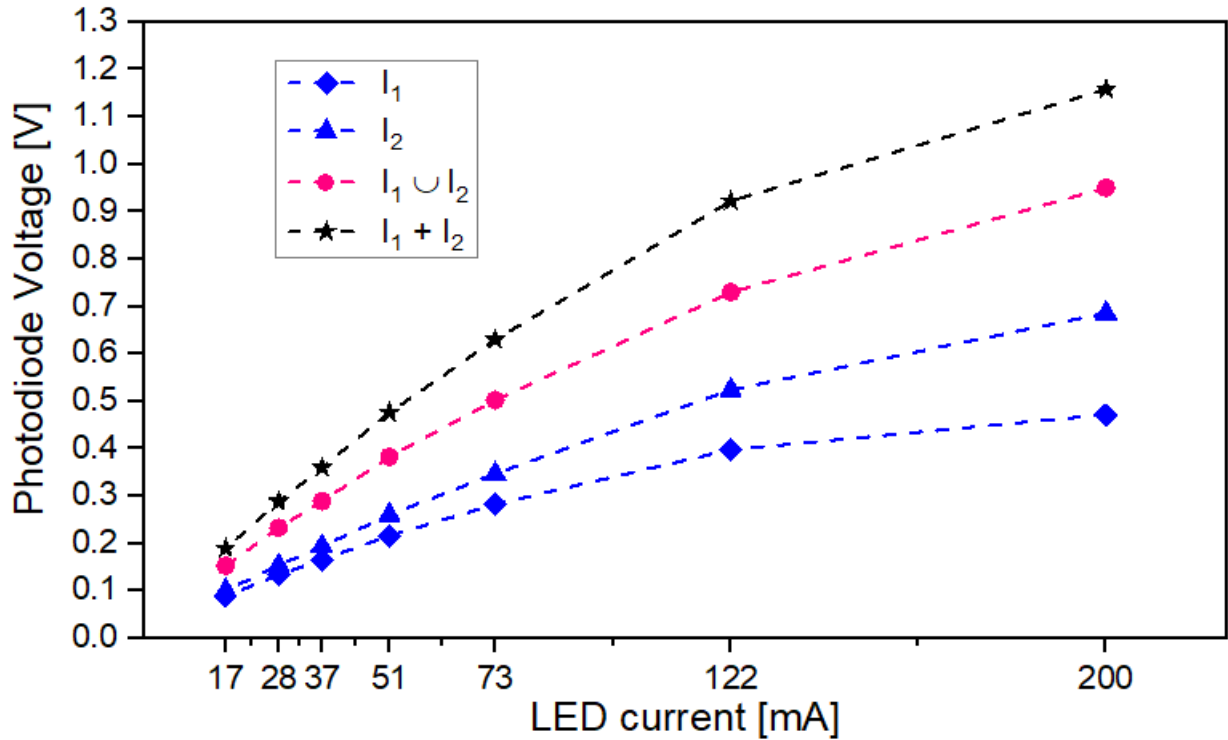


Figure 3.10 Photodiode output voltage vs LED driver current for vertical, horizontal and combined optical beams.

$I_1$ ,  $I_2$  represent respectively the horizontal and vertical emitted fluorescence beams, while  $I_1 \cup I_2$  is the simultaneous combination of the two beams.  $I_1 + I_2$  represents the numerical addition of the two beams value. Obviously, if the interference phenomenon does not occur, the photodiode output voltage for the combined beams will be necessary equal to the sum of the output voltages of the two beams separately. However, we observe that the curve of  $I_1 \cup I_2$  (pink color) is always under that of  $I_1 + I_2$  (black color) for every value of excitation intensity.

Figure 3.11 exhibits also that the interference always occur even for different value of the fluorophore concentration. From both graphs, it is clear that the interference is more visible for high excitation intensity and high fluorophore concentration. As the excitation intensity and the fluorophore concentration decrease, the curve of  $I_1 \cup I_2$  converge to that of  $I_1 + I_2$ , which means that the interference is less visible and less detectable.

In order to make the interference much more visible, the excitation light should be polarized in a specific way. In fact, the Equation (3.5) represents the interference only in scalar regime, without taken in account the vector aspect of the electromagnetic waves.

We consider two plane monochromatic waves with a spreading vectors  $\vec{k}_1$  and  $\vec{k}_2$ , polarized in directions  $\vec{u}_1$  and  $\vec{u}_2$ , presented by Eq. (3.9) and Eq. (3.10),

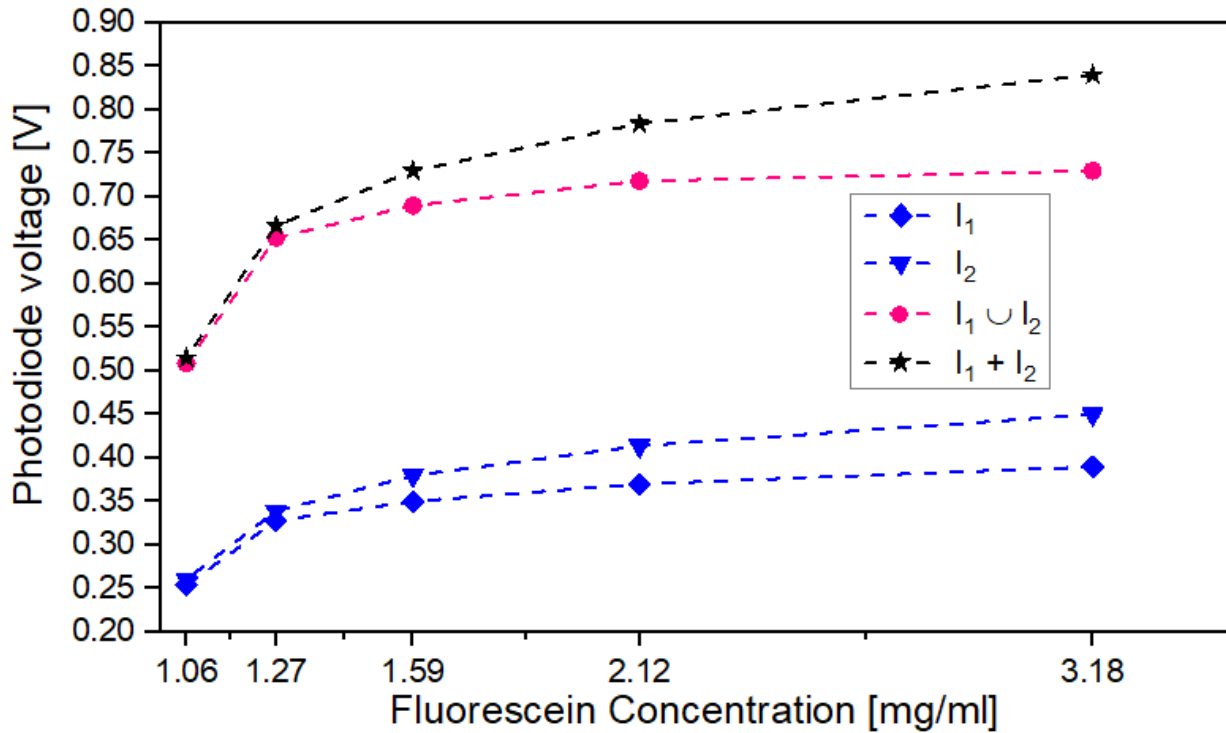


Figure 3.11 Photodiode output voltage vs fluorescein concentration for vertical, horizontal and combined optical beams.

$$\vec{E}_1(M, t) = E_1 e^{i(\omega t - \vec{k}_1 \cdot \vec{r} + \phi_1)} \vec{u}_1 \quad (3.9)$$

$$\vec{E}_2(M, t) = E_2 e^{i(\omega t - \vec{k}_2 \cdot \vec{r} + \phi_2)} \vec{u}_2 \quad (3.10)$$

The resulting intensity is

$$I = \frac{1}{2} \langle E \cdot E^* \rangle = I_1 + I_2 + 2\sqrt{I_1 I_2} \langle (\cos \Delta\psi) \vec{u}_1 \cdot \vec{u}_2 \rangle \quad (3.11)$$

where  $\Delta\psi = (\vec{k}_2 - \vec{k}_1) \cdot \vec{r} + \phi_1 - \phi_2$ ,  $I_1 = \frac{E_1^2}{2}$  and  $I_2 = \frac{E_2^2}{2}$ .

We see that the interference term  $2\sqrt{I_1 I_2} \langle (\cos \Delta\psi) \vec{u}_1 \cdot \vec{u}_2 \rangle$  depends on the polarization. In order to have a maximum interference, the two beams should have the same polarization. If the collimated beams are polarized vertically, the mirrors system will change their polarization as long as they are reflected and the interference term will be zero at the end of their intersection inside the sample. To have the maximum interference value, then the two collimated beams should be polarized horizontally. Therefore, two polarizer systems should be added to the system to get best performance. Since DMD is limited to 7.56-Micron micromirror pitch, an afocal system lenses can be added between DMD and the sample to increase the scanning resolution. It is worth mentioning also that a galvanometer or a piezo-mirror can be used instead of DMD to reduce the scanning parallelism error. Figure 3.12 presents the obtained results for fluorescence lifetime measurement for direct and combined beams. Three solution with different value of pH are investigated. The first remark to mention is dependence of lifetime on pH value. As the pH increases, the lifetime also increases. For example, the third graph with a pH value of 4.89 exhibits the smallest lifetime. The second remark is that for all these graphs, the direct and the combined beams shows a perfect parallel slope, which means a non-changing of the lifetime. The exact values of these lifetimes are summarized in Table 3.2. Thus, we can conclude the non-changing of lifetime while moving from one direct beam to combined beams.

Table 3.2 FLUORESCENCE LIFETIME VALUE

pH Value	For Direct Beam[ns]	For Combined Beams[ns]
4.89	3.5	3.5
6.13	4.9	4.9
7.10	5.1	5.1

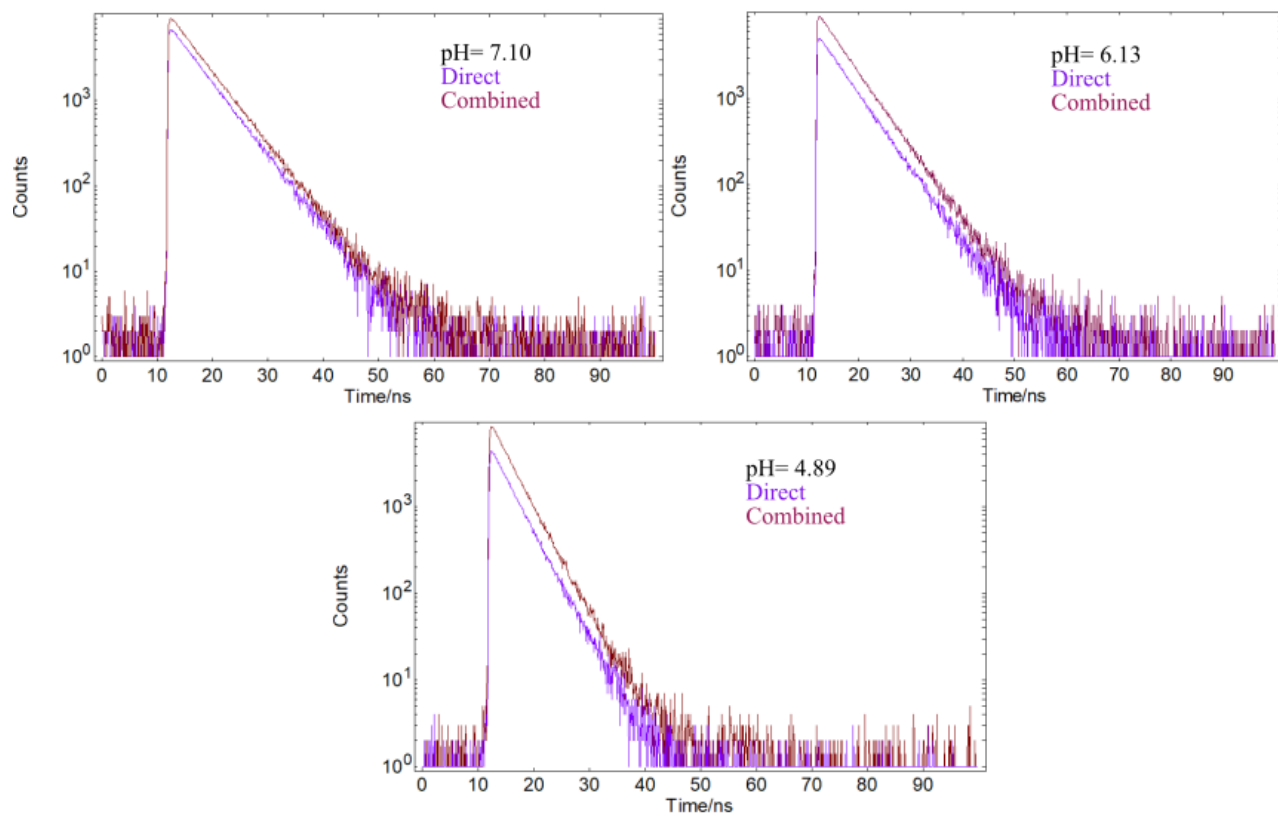


Figure 3.12 Fluorescence lifetime measurement for direct and combined beams, within three solution on three different pH value. 7.10 for first graph, 6.13 for second graph and 4.89 for the third graph.

## CHAPTER 4 HIGH-EFFICIENCY LED DRIVER

The new method of the proposed device as presented in the previous chapter is based on fluorescence lifetime measurement, where a light excitation with a short fall time is required to make this method possible. However, the most existing light source for short excitation are expensive and more difficult to be integrated in wearable instruments. To resolve this issue, Light emitting diodes (LED) can be used as an alternative solution because of their portability and lower cost. Nevertheless, LEDs fall time is in general in the average of 20 ns which is not enough for the most used fluorophore. Herein we propose a novel LED driver to deliver short pulse excitation by reducing significantly the optical fall time, which was the subject of an accepted article in IEEE International New Circuits and Systems Conference (NEWCAS) [48].

### 4.1 Introduction

Fluorescence sensing is becoming a widely used technique for biochemical research and analyses due to its non-invasive measurements and its high sensitivity and reliability compared to absorbance-based detectors [49].

Fluorescence lifetime sensing is one of the most efficient methods for various types of fluorescence microscopy. Its principle is based on exciting the sample with a pulse of light, then following this excitation, the light emitted from the sample quickly decays. The ratio of this decay is called the fluorescence lifetime  $\tau$ .

Two main issues have been identified for this method. The first one is the ability to distinguish targeted fluorescence signal from other background sources such as light excitation signal and non-target autofluorescence. Time-correlated single photon counting (TCSPC) technique is the best solution for this challenging procedure, it allows to measure the exponential decay of the echoed light from the sample under test [50]. The second challenging fact is being able to measure the fluorophores' lifetimes, which are on the order of nanoseconds. For example, these lifetimes are 14 ns, 4.0 ns, and 4.3 ns for Acridine, 6-Carboxyfluorescein, and Fluorescein Na salt, respectively [51]. Consequently the achievement of these two challenging issues requires the use of instruments that can provide light-source excitation and emission detection within a very-high speed.

Recently, many portable fluorescence instruments with nanosecond light source have been developed based on Light Emitting Diodes (LEDs) [52]. These LEDs, due to their low-power



dissipation and long lifetime, became effective light sources for a wide variety of applications, such as blood analysis [53], surface plasmon resonance sensor [54] and data transmission based on frequency modulation [55]. LEDs are also used as excitation source for fluorescence applications, due to corresponding wavelength options compared to laser diode based excitation sources.

The remaining of this chapter includes, In section 4.2, a description of fluorescence lifetime method, and shows the impact of improving LED fall time to achieve the high-measurement accuracy and efficiency. Also we state the already existing circuit drivers and methods to improve LED response time. In section 4.3 we present our new method as an alternative one to have more effective improvements. Section 4.4 exhibit the obtained results.

## 4.2 Fluorescence Lifetime Method

Fluorescence lifetime method is based on adding fluorescent indicator to the sample and exciting it by a short-light pulse. After the excitation source is turned off the light emission of the fluorescent indicator decay by a specific lifetime  $\tau$ . Any change in  $\tau$  value gives information about biochemical specifications change in the sample. Figure 4.1 shows an application example when measuring pH changes using Fluorescence emission decays of poly-amidoamine as a fluorescent indicator [56]. To measure the lifetime value  $\tau$ , Time Gating Algorithm (TGA) technique is used by measuring the emission only in two windows  $G_1$  and  $G_2$  as it is shown in Fig. 4.1 [57]. The average photons count is given by

$$N = K\tau(1 - e^{-T_G/\tau}) \quad (4.1)$$

where  $K$  is a constant depending on the excitation source,  $T_G$  is the duration of  $G_1$  and  $G_2$ . By counting the average photons  $N_1$  and  $N_2$  in gate  $G_1$  and  $G_2$ ,  $\tau$  can be found using Eq. (4.2).

$$\tau = (t_2 - t_1)/\ln(N_1/N_2) \quad (4.2)$$

As shown in Eq. (4.2),  $\tau$  is independent of excitation source  $K$ , which is the main powerful advantage of this method, in a way that any prospective excitation source variation or fluctuation will not affect measurement accuracy. It should be mentioned that in this method  $T_{delay}$  should be higher than the fall time of the excitation pulse to avoid false photon counting coming from this excitation pulse.

To increase the accuracy of lifetime  $\tau$  a multi-gate method was adopted instead of using only

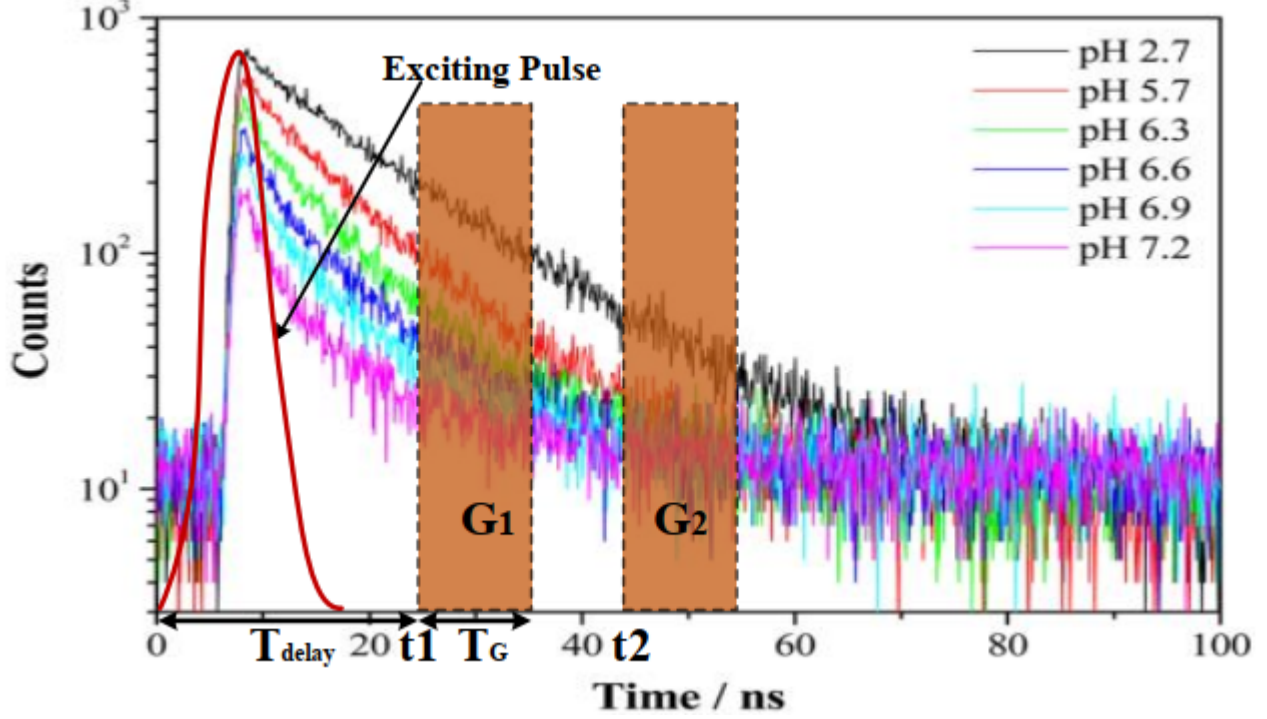


Figure 4.1 Poly-amidoamine fluorescence emission decays for pH sensing [56].

two-gate topology [57]. Expression of  $\tau$  is then given by Eq. (4.3).

$$\tau = \frac{(\sum_{j=0}^{M-1} t_j)^2 - M \sum_{j=0}^{M-1} t_j^2}{M \sum_{j=0}^{M-1} [t_j \ln(N_j)] - \sum_{j=0}^{M-1} t_j \sum_{j=0}^{M-1} \ln(N_j)} \quad (4.3)$$

where  $M$  is the number of gates and  $N_j$  is average photons number counted in gate  $G_j$ .

To increase the accuracy,  $M$  number of gates in Eq. (4.3) should be increased. However, this increase is limited by  $T_{delay}$  which is limited in its turn by the fall time of source excitation. The probability  $E_{em}(< 1)$  that a photon absorbed by the fluorophore will liberate a photoelectron can be expressed by Eq. (4.4) [58].

$$E_{em} = q E_{optics} Q e^{-T_{delay}/\tau} (1 - e^{-T_G/\tau}) \quad (4.4)$$

where  $E_{optics}$  is the signal collection efficiency for the detection optics, and  $Q$  is the quantum yield of the detector photocathode, and  $q$  is the quantum yield of the fluorescence probe.

In order to increase  $E_{em}$ ,  $T_{delay}$  and in its turn the excitation fall time should be as small as possible. As a result, from the above analysis, by decreasing excitation fall time the accuracy

of  $\tau$  and the measurement efficiency will be improved, in a way that the probability  $E_{em}$  and the number of gates  $M$  will be increased.

On the other hand, the LED fall time delay is due to its intrinsic junction capacitances that take time for discharging. The time depending turn-off transient can be expressed by Eq. (4.5) [59] which gives a fall time of the optical signal (90% to 10%) as shown in Eq. (4.6).

$$P_{opt}(t) \sim \frac{I_{pulse}}{\left(\sqrt{\frac{1}{k_{LED} \cdot I_{pulse}}} + t\right)^2} \quad (4.5)$$

$$t_f = 2.11 \frac{1}{\sqrt{k_{LED} \cdot I_{pulse}}} \sim 2.11 \frac{1}{\sqrt{I_{pulse}}} \quad (4.6)$$

This study shows that the fall time depends in the current pulse width ( $\sim \frac{1}{I_{pulse}}$ ). Several

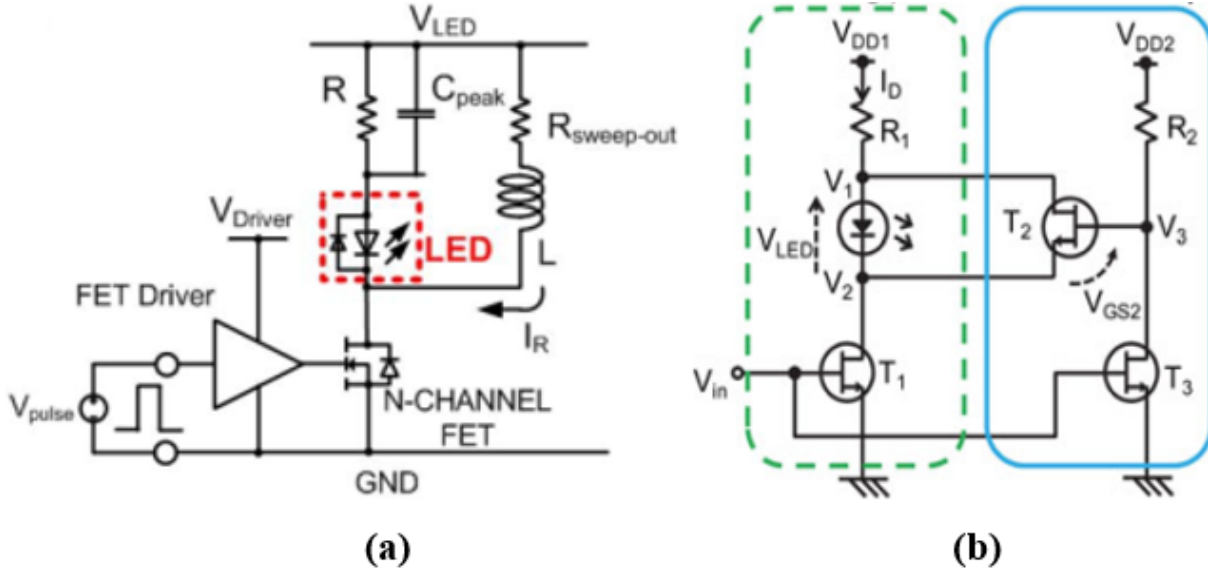


Figure 4.2 LED rise/fall time improvement driver circuits: (a) Halbritter *et al* circuit [59]; (b) Toshiki *et al* circuit [55].

authors improved the fall time of LED response, the main of them Halbritter *et al* have proposed a driver circuit to improve LED time response by using a capacitor and an inductor as it is shown in Fig. 4.2(a) [59].

The principle of this circuit is that the added capacitor  $C_{peak}$  by its charging provides a boosting current when the LED is turned on, which improves the optical rising time. For the optical fall time, the inductor  $L$  stores the energy and when the LED is turned off a negative current peak occurs, thus the optical fall time is ameliorated.

Figure 4.2(b) shows another circuit that was introduced by Toshiki *et al* to enhance the optical fall time [55]. The main basic principle of this idea is to short-circuit the LED in the turn off phase by using a GaAs FET  $T_2$ . By this technique the remaining carriers swept out which makes the LED shut-down swiftly. The drawbacks with these two circuits is that, the use of an inductor in the first one is not always desirable, especially if this LED driver circuit should work with RF applications. For the second method, this idea is less efficient when operating high current LEDs. At high current a complete discharge of the LED intrinsic junction capacitor cannot be done within an enough time.

### 4.3 Novel Driver Circuit

A novel driver circuit is proposed to improve the LED optical fall time, which is an alternative solution to above described limitations of aforementioned methods. The schematic of the proposed circuit is presented in Fig. 4.3. This new circuit is based on high-speed switching NMOS and PMOS transistors that toggle between two-operation phases as shown in Fig. 4.4. When this LED is turned on, transistors  $N_1$  and  $N_2$  are on and Transistors  $P_1, P_2, \dots, P_6$  are off, which leads to the equivalent circuit (a) in Fig. 4.4.

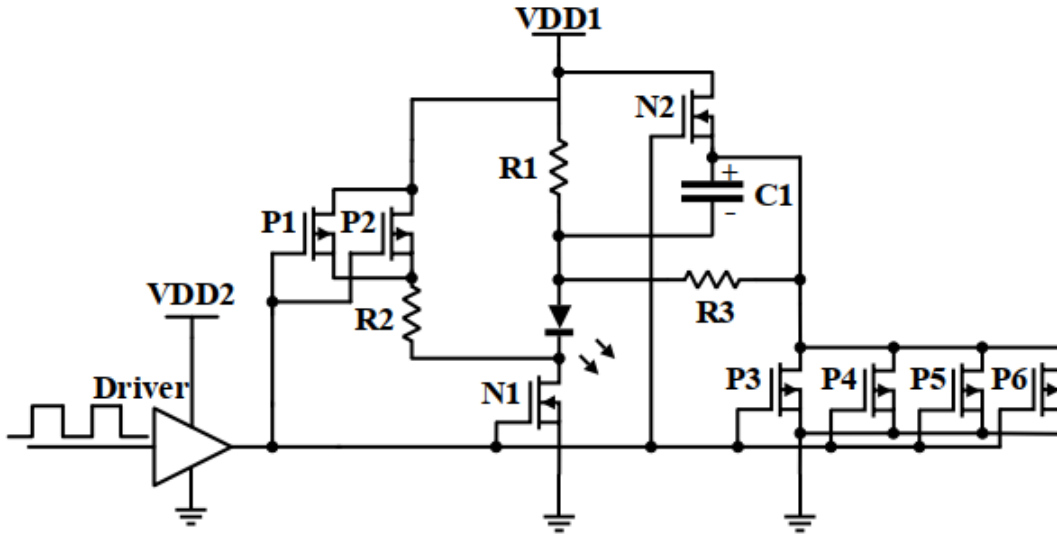


Figure 4.3 Novel circuit intended to reduce the fall time of the LED.

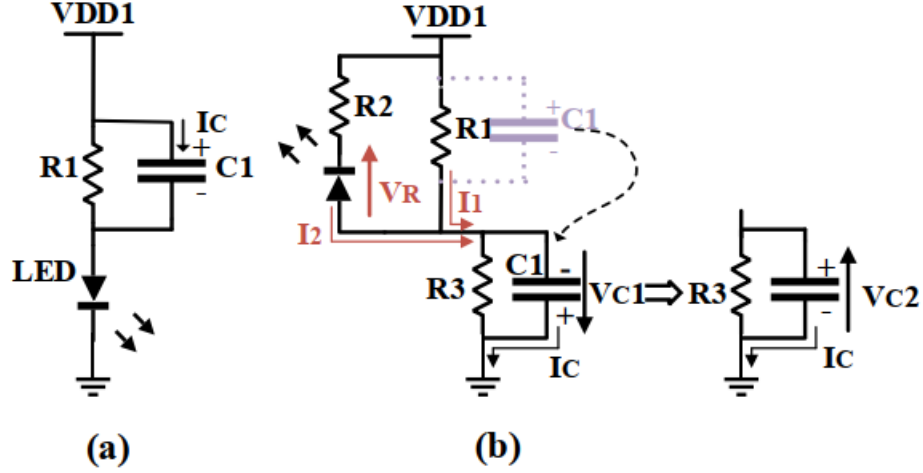


Figure 4.4 Driver equivalent circuit: (a) Turn-On phase, (b) Turn-Off phase.

In this phase, the capacitor  $C_1$  is charged and gives a current peak to the LED which improves its optical rise time. When the LED is turned off,  $N_1$  and  $N_2$  are off and  $P_1, P_2, \dots, P_6$  are on, which lead to the equivalent circuit in Fig. 4.4(b). In this phase the reverse voltage  $V_R$  discharge the LED which sweep-out the remaining carriers. Transistors  $P_3, P_4, \dots, P_6$  are used to sink direct and reverse currents  $I_1$  and  $I_2$  from the circuit to ground.

The second part of this proposed circuit is to exploit the already used capacitor  $C_1$  in the turn on phase to speed up the fall time when the circuit is in its off phase. The charge and discharge phases of this capacitor maintain the carriers sweep-out speed.

Figure 4.5 shows the timing diagram for each part of the circuit.

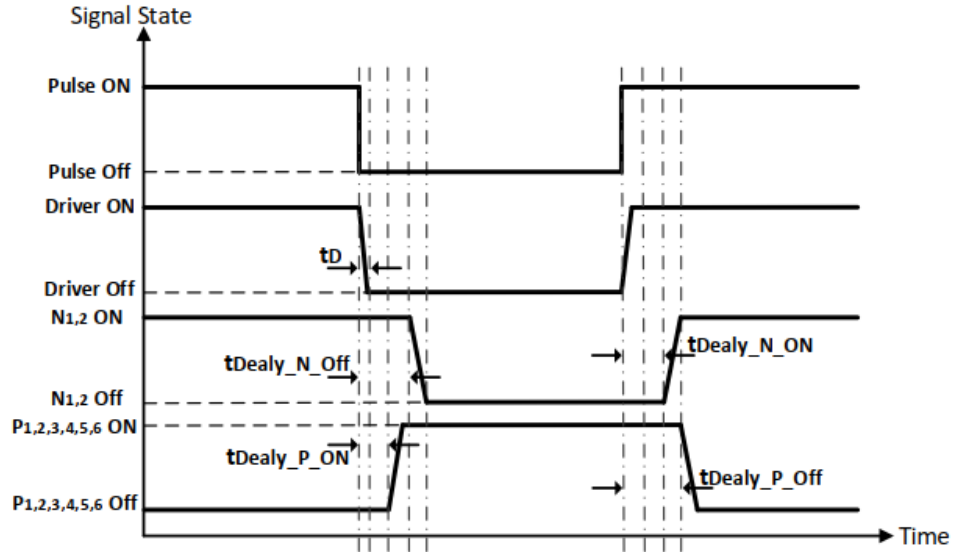


Figure 4.5 Timing diagram of proposed circuit.

To have a better results  $t_{Delay\_P\_ON}$  of  $P_3, P_4, \dots, P_6$  should be lower than  $t_{Delay\_N\_Off}$  of  $N_1$  which allow to obtain a smooth and synchronous operation by preventing the current coming from  $P_1$  and  $P_2$  to cause an excess to  $N_1$  drain current.

We report in Table 4.1 the simulation components and parameters used for this circuit driver and Table 4.2 shows all signal state time values.

Table 4.1 COMPONENTS OF THE LED DRIVING CIRCUIT

Parameter/Component	Designation	Value/Part number
NMOS	$N_{1,2}$	FDY301NZ
PMOS	$P_{1,2,3,4,5,6}$	BSS84LT1G
LED	-	GD DASPA2.14
DC Power Supply (V)	$V_{DD1}, V_{DD2}$	5, 5.75
Resistance ( $\Omega$ )	$R_1, R_2, R_3$	10.5, 11, 20
Capacitor (nF)	$C_1$	5
MOSFET Driver	Driver	LMG1020

Table 4.2 SIGNAL STATE TIME VALUES

Signal state times	Value [ns]
$t_D$	0.35
$t_{Delay\_N\_Off}$	8
$t_{Delay\_N\_ON}$	6
$t_{Delay\_P\_ON}$	3.6
$t_{Delay\_P\_Off}$	12

#### 4.4 Results

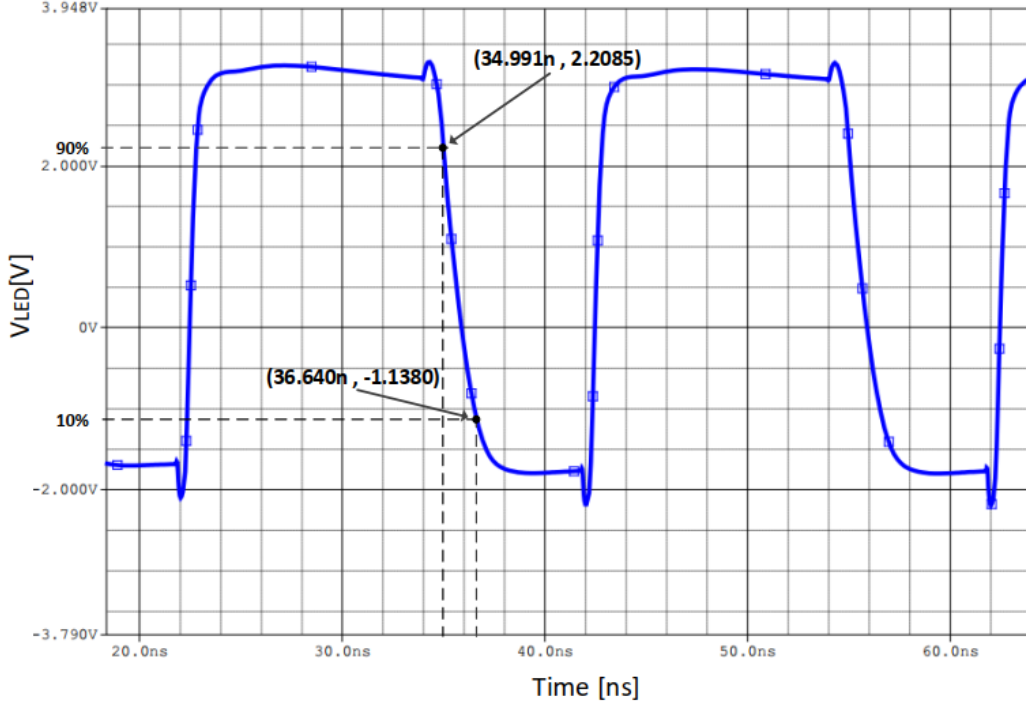


Figure 4.6 LED terminal voltage ( $V_{LED}$ ) waveform for a square waveform input with the switching driver.

Simulations of the proposed circuit are achieved with a square waveform input and with a current pulse of  $225mA$ . Figures 4.6 and 4.7 depicts the obtained results for LED terminal voltage with and without switching driver respectively. The fall time  $t_f$  is defined as the time needed by the signal to fall from 90% to 10% of its peak value. Without switching driver,  $t_f$  is equal to  $32.59ns$  and with switching driver,  $t_f$  is equal to  $1.65ns$ . That means a reduction of approximately 96%.

Figure 4.8 shows the dependence of optical fall time in the current pulse. These obtained results confirm the theoretical predicted dependency ( $\frac{1}{\sqrt{I_{pulse}}}$ ). As  $I_{pulse}$  increases  $t_f$  decreases. Figure 4.9 presents the fluorescence lifetime measurement efficiency  $\chi$  vs Lifetime  $\tau$ , with and without the used switching driver.  $\chi$  is given by Eq. (4.7).

$$\chi(\tau) = \frac{E_{em}}{qE_{optics}Q} \in [0, 1] \quad (4.7)$$

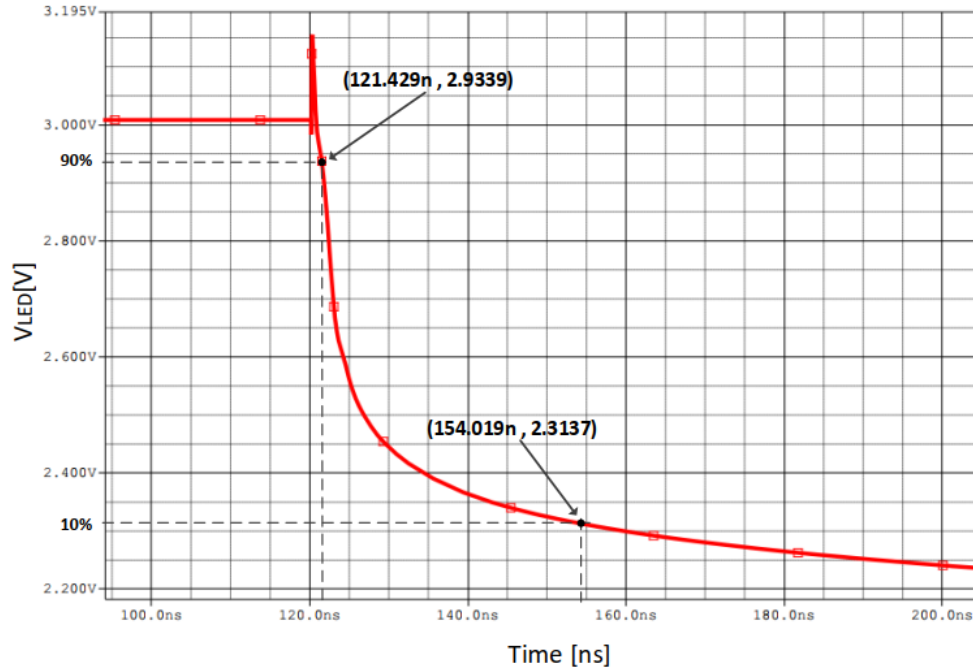


Figure 4.7 LED terminal voltage ( $V_{LED}$ ) waveform without the switching driver.

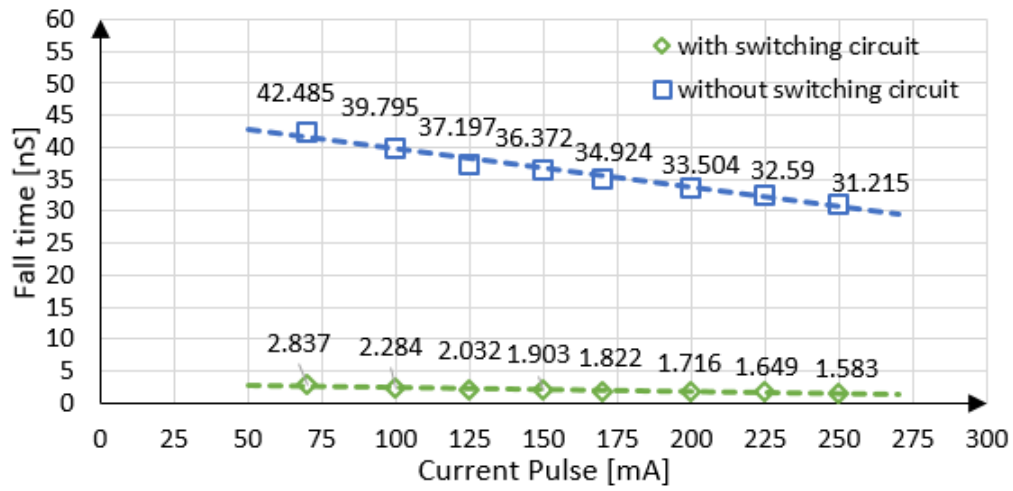


Figure 4.8 Optical fall time vs LED pulse current with and without the switching circuit.



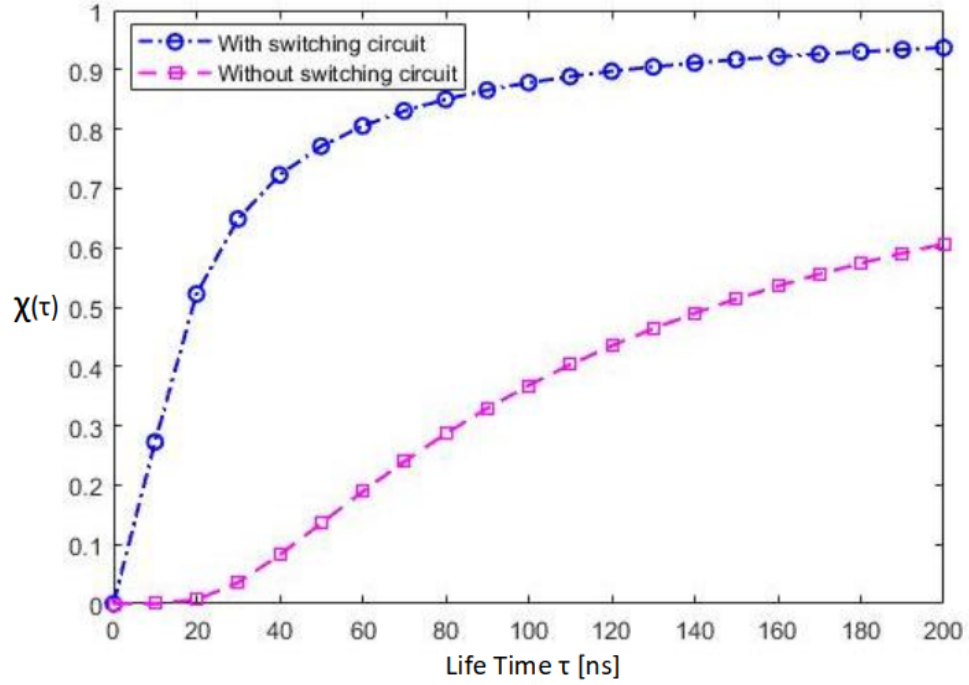


Figure 4.9 Fluorescence lifetime efficiency  $\chi$  vs. Lifetime ( $\tau$ ).

Table 4.3 PERFORMANCE COMPARISON OF LED DRIVERS

	[4]	[7]	[11]	[This work]
Driver technology	RF bipolar	GaAs FET	MOSFET	MOSFET
Supply voltage	5V	12V	12V	5V
LED driver current	66.1mA	22mA	2A	225mA
LED application	Fluorescence	Communication	Illumination	Fluorescence
LED color	UV	Blue	IR	Deep blue
Wavelength	405nm	465nm	850nm	450nm
Rise time	6.2ns	22ns	2.6ns	0.6ns
Fall time	6ns	10ns	2.6ns	1.6ns
Results type	experimental	experimental	experimental	simulation

The obtained results exhibit how this driver circuit improves significantly the fluorescence measurement efficiency. Likewise, this improvement is more important for smaller lifetime values ( $\leq 60ns$ ).

Performance of the proposed LED driver is summarized and compared with that of the previously reported works in Table 4.3.

## 4.5 Conclusion

This work evaluates the advantages of using LED technology as an excitation source for fluorescence lifetime based measurements, which is one of the most efficient sensing method for biochemical research and studies. We reported a novel LED driver circuit to achieve a high speed fall time excitation, as a major challenging point for fluorescence lifetime efficiency and accuracy. The proposed driver circuit achieved an excitation light fall time of around  $1.6ns$ . This short time value allows to achieve a high impact on fluorescence lifetime efficiency.

## CHAPTER 5 VALVES ARRAY FOR A FULL MICROFLUIDIC INTEGRATION

Instead of working with only one 3D environment, the proposed instrument presented in the previous chapters can be used for a system consisting of large number of microfluidic rooms to make possible multiple independent imaging measurements at the same time and in one chip . However, a large number of micro-fluidic channels will be needed to access various specific locations. Thus, in this chapter we present an embedded on-chip controller to drive the expected large number of switching valves with less number of off-chip control components. Also, the utility of this system for Organs-On-Chip (OOC) is presented in this chapter likewise. The following sections are the reproduction of a submitted article in IEEE Engineering in Medicine and Biology Society Conference (EMBC) [60].

### 5.1 Introduction

The interaction between accumulated work in microfluidic, cell culture and cell biology research has led recently to the emergence of Organ-On-Chip (OOC) technology. OOC consists of a microfluidic structure (Micro chambers, channels, valves, etc) that contains specific areas to handle living cells, controlled by micro-electromechanical systems (MEMSs) to make them mimic the behaviors and functionality of their counterparts in vivo.

Nowadays, as ethical concerns on animal experiments are rising, OOC technology is a very promising alternative solution for drug development and testings. Furthermore, the recent advancements made in this field make OOC a trustworthy candidate for more understanding of human organs physiology, as well as a reliable drug testing platform that can be used for personalized medicine and diseases studies [61] [62] [63].

On the other hand, while the complexity of OOC systems increases, the necessity of an efficient integrated drug delivery system follows. An ideal drug delivery system should be as subtle as it can target a specific site-of-interest in the organ. In this regard, a micro-needle array with nano-filters have been developed for a nanometer-scale selectivity [64]. From a precision delivery standpoint, a drug controller is indispensable for avoiding the delivery of uncontrolled drug doses. In this context, a full drug delivery System-On-Chip have been proposed with an integrated drug reservoirs and full wireless control [65]. As multiple organ modules can be interconnected in a physiologically relevant way to build a human-on-chip platform (Fig.5.1) [66], a large number of drug delivery channels is needed to make possible the access to all specific parts on the chip with a flexible switching manner.

Thus, such system requires a large number of micro-valves in order to make a full control of drug steering. Thereby, the challenging point is to find a way to drive this expected large number of valves with a less number of off-chip controllers. Several works have been done in this regard, notably a micro-pneumatic digital logic structures was designed to drive large number of micro-valves with less control lines [67] [68]. These structures, made up of pneumatic digital gates (AND, OR, NOT, NAND, and XOR), are based on micro-valves with MOSFET-like function. More recently, Kawi *et al* [69] proposed a control method based on multiplexers-demultiplexers, thus they can control 256 individual on-chip valves with only 18 control lines (Fig. 5.2).

In this work, we propose a novel system that can control  $5^n$  channels with only  $n$  line

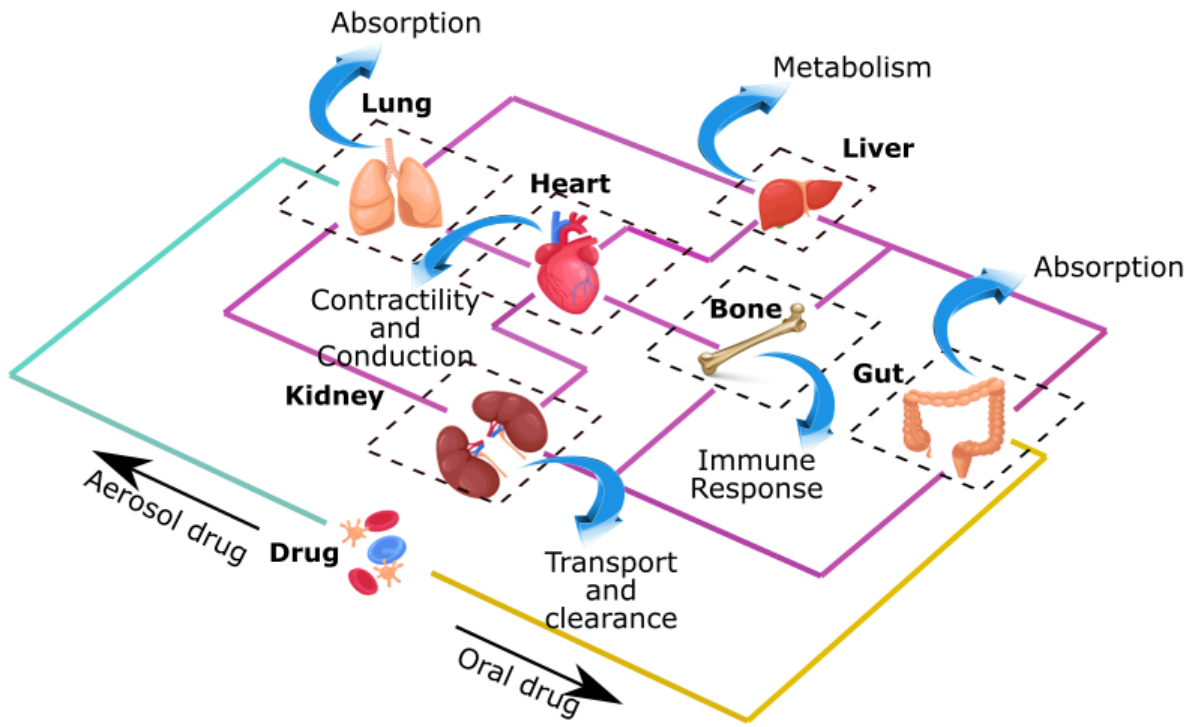


Figure 5.1 Body-on-chip model

control. As for example,  $625 = 5^4$  channels will be drove with only 4-line control interfaces.

The remaining of this chapter includes, in section 5.2, a description of the system we propose as an alternative solution to reduce the number of off-chip control components. Section 5.3 exhibits the obtained results.

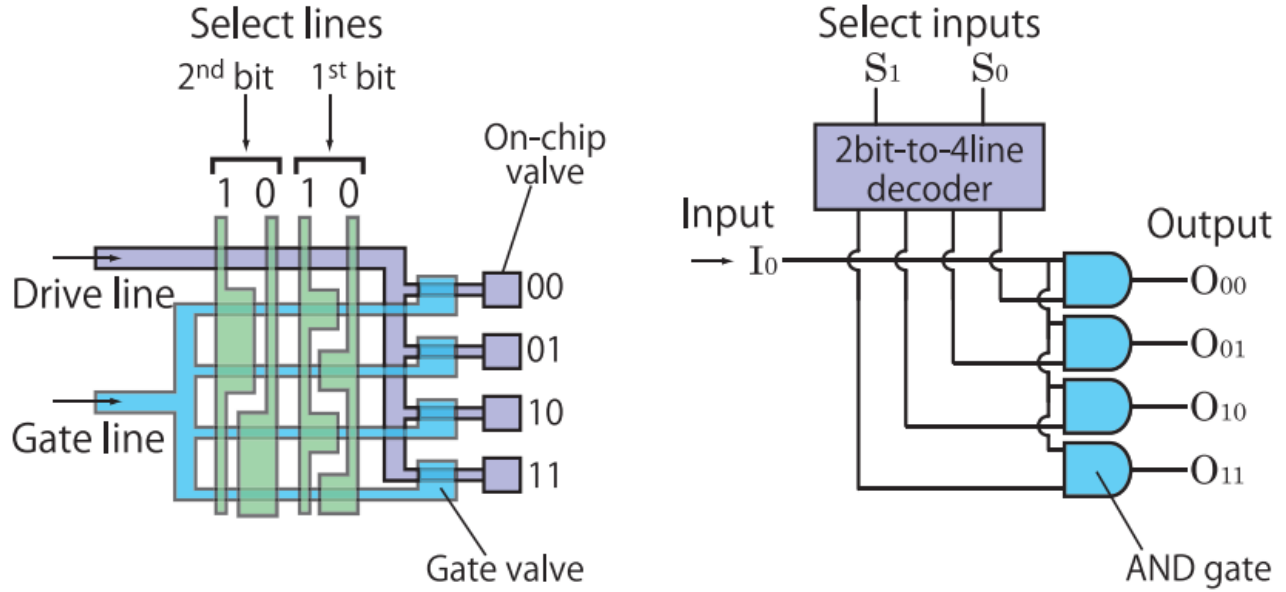


Figure 5.2 Two bit DEMUX valve control system and its equivalent logic circuit [69]

## 5.2 Description of the Proposed System

The operation principle of proposed system is presented in both Fig. 5.3 and Table 5.1.

Five channels are controlled by one pneumatic line through eight valves  $V_1, \dots, V_4$  and  $W_1, \dots, W_4$ . Initially,  $V_1, \dots, V_4$  are Off and  $W_1, \dots, W_4$  are ON, so the fluid goes throughout  $Ch_1$ . When a pressure  $P_1$  is applied, just  $V_1$  and  $W_1$  that change their state ( $V_1$  becomes ON and  $W_1$  becomes Off). By this way, the input fluid goes throughout  $Ch_2$ . When a pressure  $P_2 > P_1$  is applied, in addition to  $V_1$  and  $W_1$ ,  $V_2$  becomes ON and  $W_1$  becomes Off, so the fluid goes throughout  $Ch_3$ . By the same way, we can make the fluid goes throughout  $Ch_4$  and then  $Ch_5$ .

Table 5.1 TRUTH TABLE OF SCHEMA SHOWN IN FIG. 3.

Pressure	V1	V2	V3	V4	W1	W2	W3	W4	Active Channel
Initial	Off	Off	Off	Off	ON				Ch1
P1	ON	Off	Off	Off	Off	ON			Ch2
P2	ON	ON	Off	Off	Off	Off	ON		Ch3
P3	ON	ON	ON	Off	Off	Off	Off	ON	Ch4
P4	ON	ON	ON	ON	Off	Off	Off	Off	Ch5

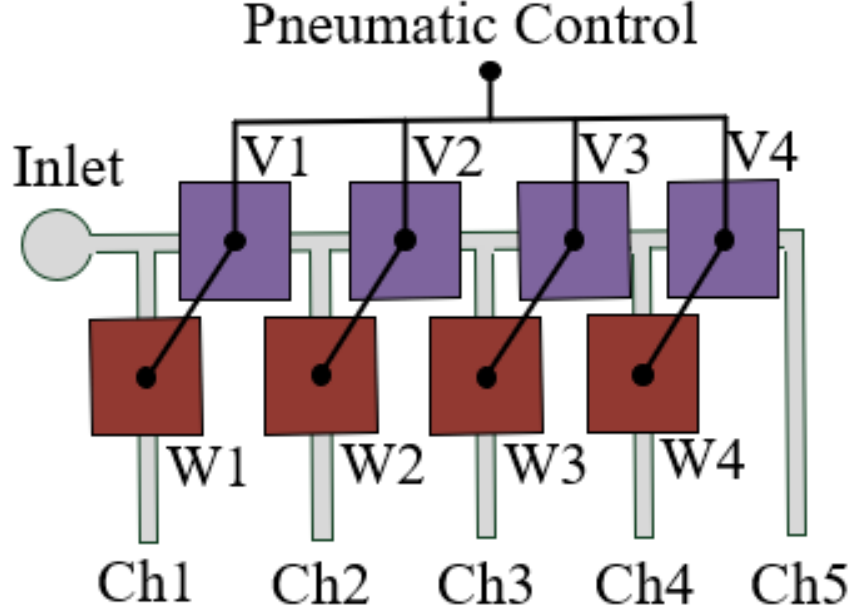


Figure 5.3 Simplified schema illustrating the proposed system.

by applying respectively pressure  $P_3$  and  $P_4$  in a way that  $P_4 > P_3 > P_2 > P_1$ . Therefore, this system is like a demultiplexer that conducts the input fluid to a specific output channel based on a selected level of pressure.

The challenging point is to find a way to build a multi-valves system that works in such a way. To do so, analysis of membrane deflection, that can be modelled as a beam fixed from both ends, must be done.

The relationship between beam's deflection and the applied load is described by Euler–Bernoulli expression, given by Eq. (5.1).

$$\frac{d^2}{dx^2}(EI \frac{d^2\omega}{dx^2}) = q \quad (5.1)$$

where  $E$  is material Young's modulus,  $I$  is second moment of area,  $\omega$  is the deflection of the beam in the vertical direction at some position of  $x$ , where  $x$  is a point along the beam, and  $q$  represents the used load [10].

In present case, the beam is exerted for uniform load, and the center deflection can be deduced [70];

$$\omega_c = \frac{qL^4}{384EI} \quad (5.2)$$

where  $\omega_c$  is the deflection of the beam at the center and  $L$  its length. For a rectangular beam with  $h \times b$  cross section, we have

$$\begin{cases} I = \frac{bh^3}{12} \\ q = P.b.h \end{cases} \quad (5.3)$$

where  $P$  is the applied pressure. Thus, the relation between the central deflection, pressure and the geometry is given by Eq. (5.4)

$$\omega_c = P \times \frac{L^4}{32.E.h^3} \quad (5.4)$$

The working principle of proposed control method is based on this equation, in a way that we can build a valves array with different geometries controlled with the same input pressure. When a specific pressure is applied, the displacement response of each membrane differs based on its geometry. Figure 5.4 presents the idea of this system.

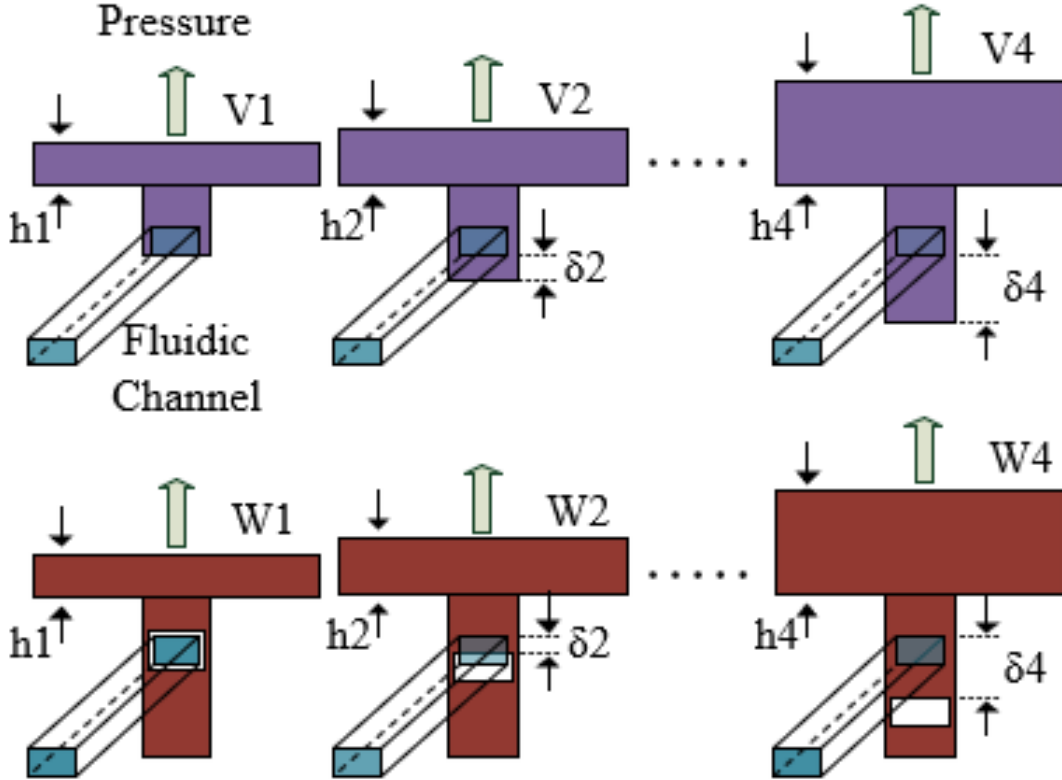


Figure 5.4 The proposed valves array system based on geometries variation

The membrane high  $h_1$  of  $V_1$  and  $W_1$  is smaller than  $h_2$  of  $V_2$  and  $W_2$ , and so on ( $h_1 < h_2 < h_3 < h_4$ ).  $\delta_2$  is the displacement of  $V_2$  when  $P_1$  is applied. So when  $P_1$  is applied  $V_1$  is open but  $V_2$  still closed and also  $V_3$  and  $V_4$ . The same status for  $P_2$ ,  $P_3$  and  $P_4$ . In other words,  $P_1$  opens just  $V_1$ ,  $P_2$  opens  $V_1$  and  $V_2$ ,  $P_3$  opens  $V_1$ ,  $V_2$  and  $V_3$ , and finally  $P_4$  opens  $V_1$ ,  $V_2$ ,

$V_3$  and  $V_4$ . In the other hand, for valves  $W_1, \dots, W_4$  a window is made to make them ON by default. So, when  $P_1$  is applied  $W_1$  is closed, but  $W_2$  become open. The same thing for  $P_2$ ,  $P_3$  and  $P_4$ . Also,  $P_1$  closes just  $W_1$ ,  $P_2$  closes  $W_1$  and  $W_2$ ,  $P_3$  closes  $W_1$ ,  $W_2$  and  $W_3$ , and finally  $P_4$  closes  $W_1, \dots, W_4$ .

The second challenging point is that when pressure  $P_4$  is applied the previous membranes especially  $V_1/W_1$  and  $V_2/W_2$  may not support such a high pressure. To resolve this issue, a Silicon braking obstacle was added to limit the membrane deflection (Fig.5.5).

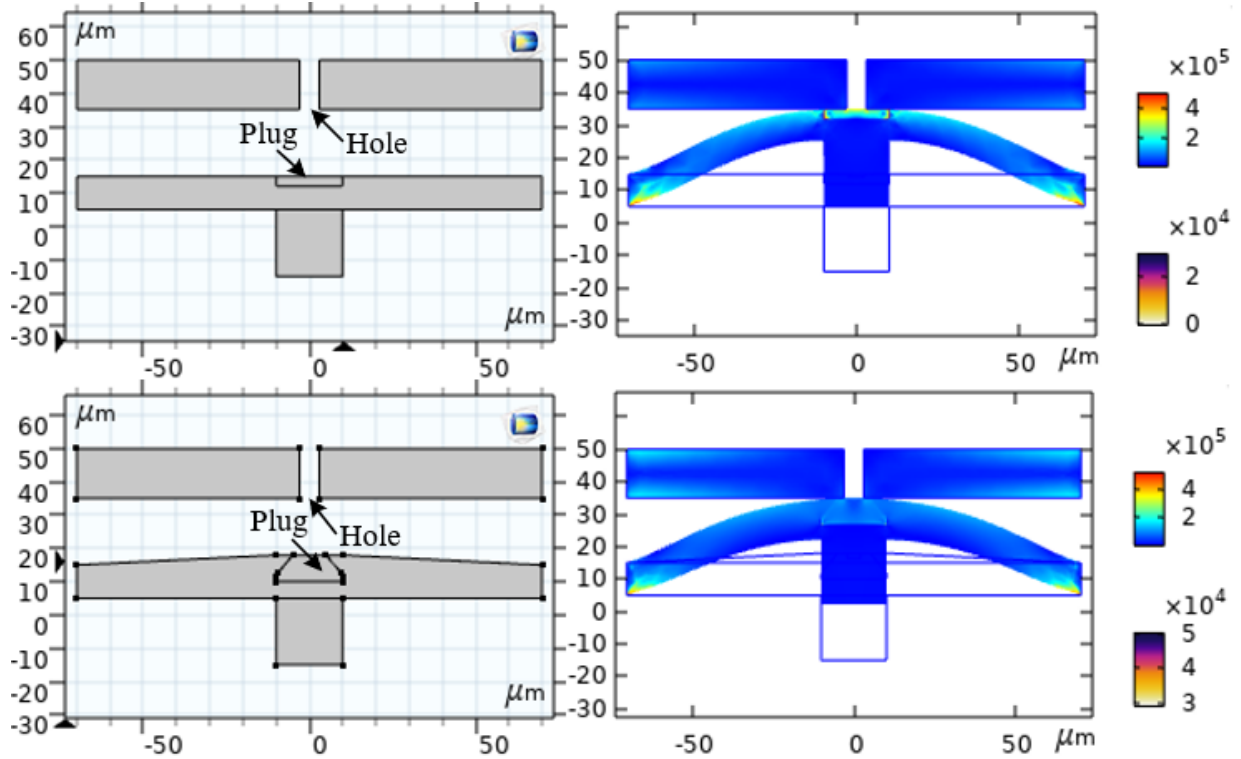


Figure 5.5 Membrane braking obstacle simulation

The role of the hole, shown in Fig. 5.5, is to make possible the air suction and so attract the membrane. A mince layer of Polytetrafluoroethylene (PTFE) material is used to form a plug in order to close the hole when the membrane reaches the silicon obstacle. The material used for the membrane is PDMS, due to its best elastic proprieties.

Mechanical stress simulation is presented in the top right of Fig. 5.5. It is shown that there is more constraints concentrated around the PTFE plug. To resolve this issue the geometry of the membrane is a little bit edited as presented in bottom left of Fig.5.5, as well as the form of the plug. The constraints concentration problem is now resolved as it is shown on the simulation results.



Table 5.2 shows the design parameters for the eight valves. All valves have the same length  $L = 140\mu m$ .  $\delta_i$  is the displacement of valve  $V_i/W_i$  when pressure  $P_{i-1}$  is applied.  $7\mu m$  is the height of the opening section of the valve which is also the height of the micro-fluidic channel.

Table 5.2 PHYSICAL AND GEOMETRICAL DESIGN PARAMETERS FOR THE PROPOSED SYSTEM

Pressure/ Valve	0.9 kPa	3.4 kPa	9.8 kPa	24 kPa
<b>V1/W1</b> $h = 10\mu m$	$7\mu m$			
<b>V2/W2</b> $h = 14\mu m$	$\delta_2 = 3.4\mu m$	$10.4 = 7 + \delta_2$		
<b>V3/W3</b> $h = 20\mu m$		$\delta_3 = 5.5\mu m$	$12.5 = 7 + \delta_3$	
<b>V4/W4</b> $h = 28\mu m$			$\delta_4 = 7.2\mu m$	$14.2 = 7 + \delta_4$

After building the basic unit DEMUX that controls five channels, the system can be extended to build a control system for large number of channels. Figure 5.6 represents the global system realized to drive  $125 = 5^3$  channels with 3 off-chip control lines. All fluidic channels are controlled directly by DEMUXs in level 1. These DEMUXs are controlled by DEMUXs in level 2 which in turn are driven by DEMUX in level 3.

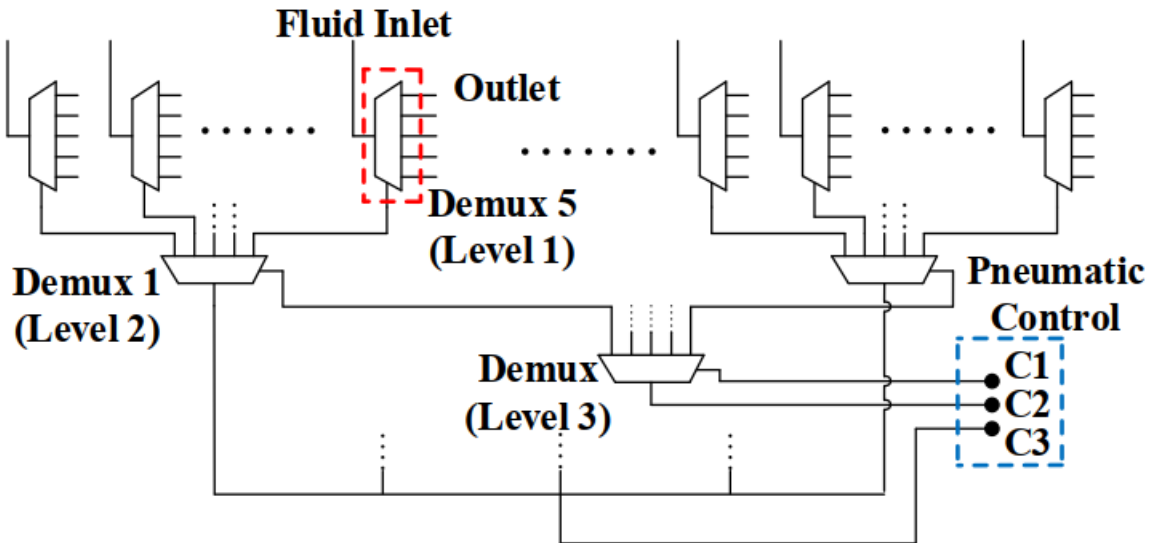


Figure 5.6 Global system schematic to drive 125 channels with 31 DEMUX units and 3 off-chip control lines

Figure 5.7 shows the final fluidic chip of proposed system. Its dimensions are  $2\text{cm} \times 1.8\text{cm} \times 2\text{mm}$ , with 125 outlets, 25 inlets, 31 DEMUXs and 3 pneumatic control lines.

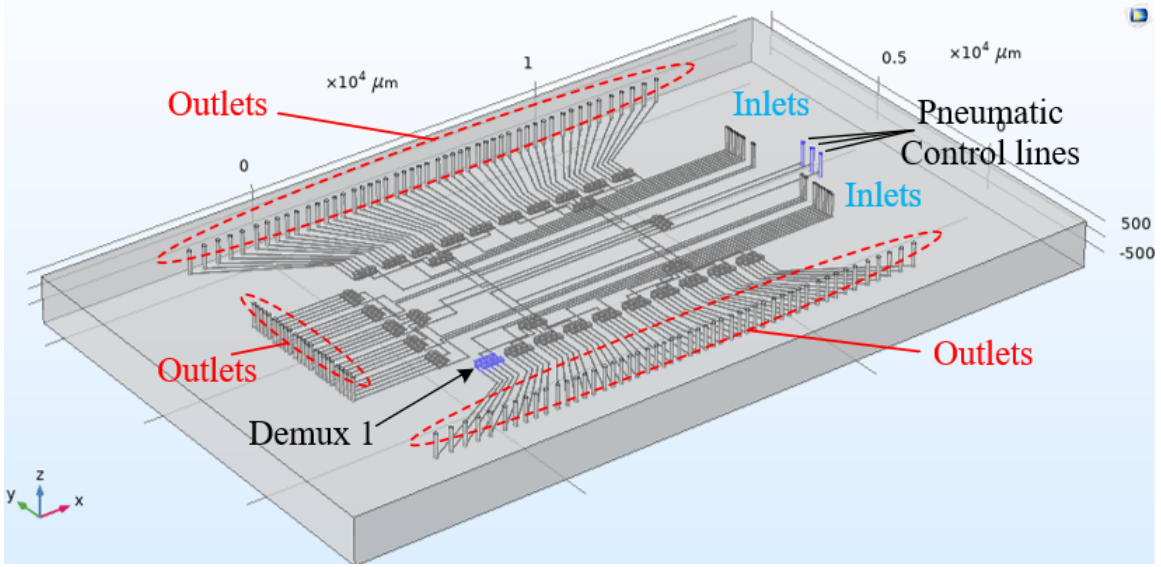


Figure 5.7 The proposed Integrated microfluidic platform

### 5.3 Results

The simulations of proposed system have been done with COMSOL Multiphysics modeling software. Figure 5.8 shows the vertical displacement of each membrane depending on its associated height, with an applied differential pressure of 3 kPa.

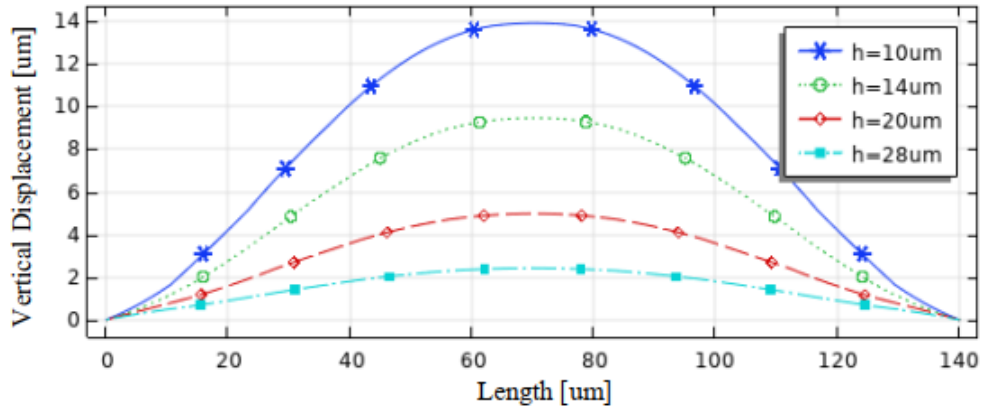


Figure 5.8 Vertical displacement vs membrane high

The displacement graduation is clearly depending on height value as a geometry parameter of each valve.

Figure 5.9 presents the displacement profile for each valve as function of differential pressure variation. As assumed, when a valve reaches its braking obstacle, the displacement remains constant while the following valves still increase in terms of deflection. The pressure needed to make the last valve reaches its upper limit is 22kPa, while for the first valve is 0.9kPa.

Figures 5.10 and 5.11 depict the obtained results for fluidic flux profile according to differential pressure applied to each valve. Figure 10 is for valves  $V_1, \dots, V_4$  and Figure 11 is for valves  $W_1, \dots, W_4$ .

Water is used for this simulation as a test fluid. The flux variation is between 0 and  $13.10^6 \mu m^3/s$ , and the variation speed depends on each valve. Variation speed under the first valve  $V_1/W_1$  is the greatest one, which is normal because of its fast ON/Off operation. While the variation speed under the last valve  $V_4/W_4$  is the lowest one because of its slowest ON/Off operation.

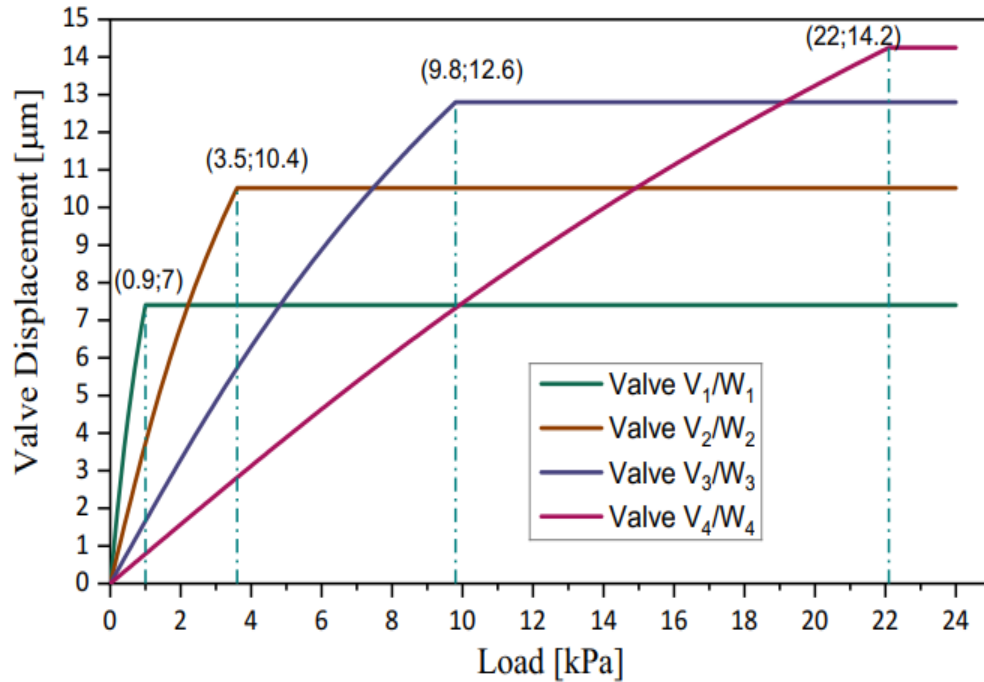


Figure 5.9 Valves displacement vs applied differential pressure

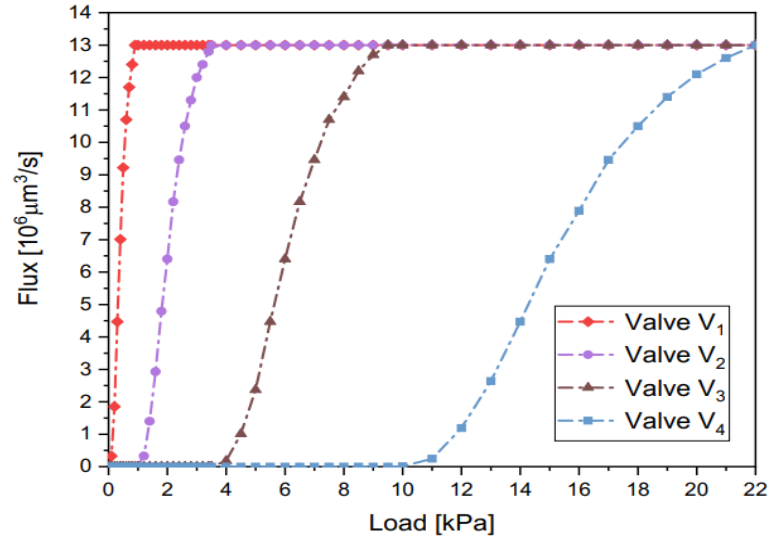


Figure 5.10 Fluidic flux vs applied differential pressure for valves  $V_1, \dots, V_4$

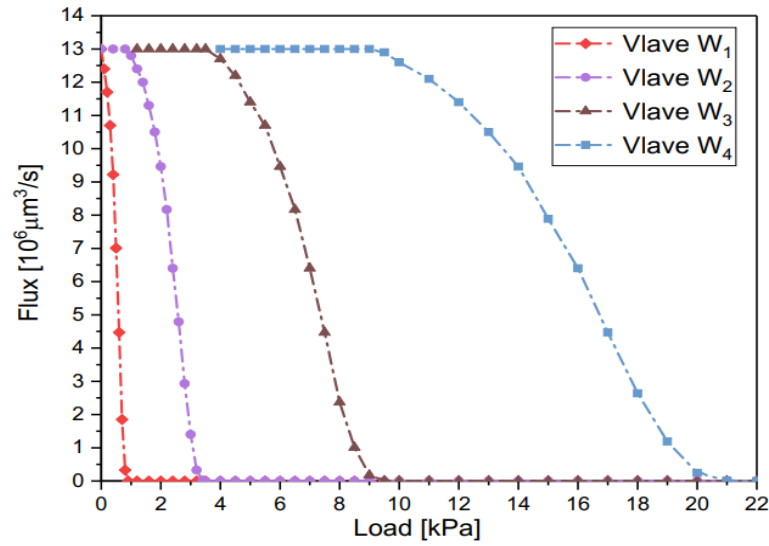


Figure 5.11 Fluidic flux vs applied differential pressure for valves  $W_1, \dots, W_4$

## 5.4 Conclusion

This work evaluates the increasing necessity of building a very efficient drug delivery system as the complexity of organs-on-chip structures keeps increasing and multiple organs can be interconnected in a single platform. We reported a novel system for microfluidic valves array control, as a new method to drive a large number of channels with a less number of off-chip controllers. With our system, we have been able to control 125 microfluidic channels with only 3 control lines. The principle of this system can be exploited and improved to control an even bigger number of microfluidic channels.

## CHAPTER 6 ELECTRONIC SYSTEM FOR FULL PORTABILITY

### 6.1 Overview

In this brief chapter we present a designed electronic system to make this fabricated instrument fully wearable in terms of power and communication. Also, a specific readout circuit was designed for mechanical sensors that can be integrated in this instrument. These mechanical sensors helps to have a second measurements of the desired bio-chemical parameters and thus a calibration of the proposed optical sensor is then possible. Therefore, this circuit helps to avoid false measurements and also the necessity of an external calibration.

This electronic system consisting of power circuit, communication block and calibration sensing, will make this instrument fully portable with a high autonomy.

### 6.2 System description

Figure 6.1 presents the schema of the designed electronic system with different blocks. It's made up of read-out block, power block, CPU block and communication block.

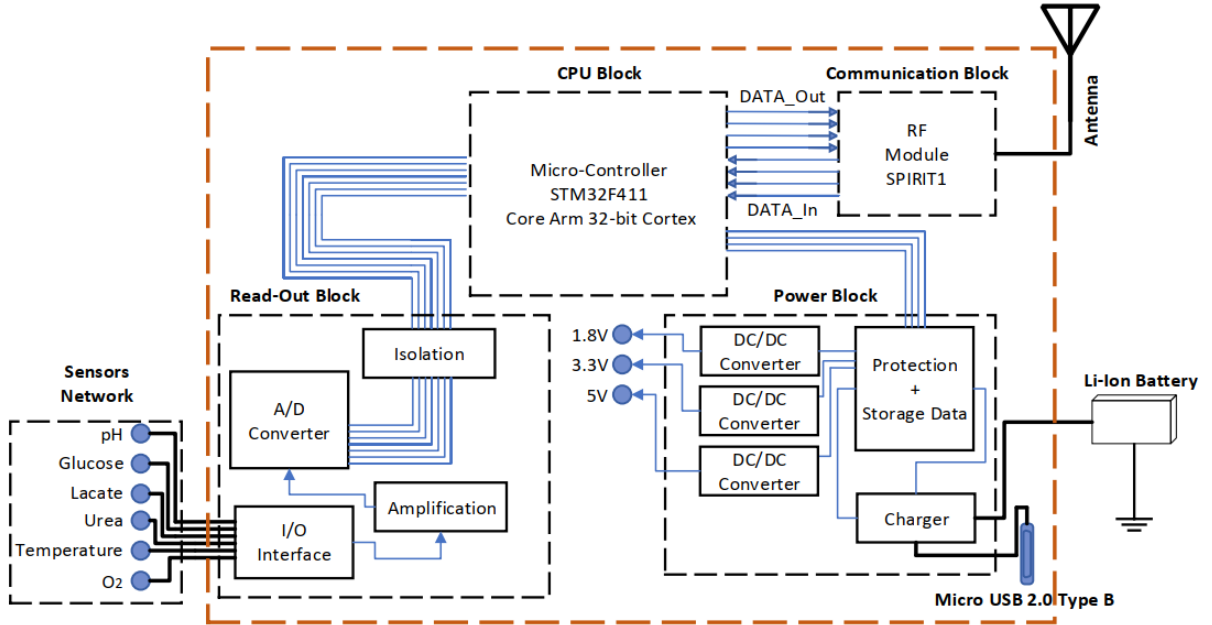


Figure 6.1 Block diagram of the proposed electronic system

### 6.2.1 Power Block

Using battery in this instrument is very useful and necessary for its portability and power autonomy.

For this purpose, the battery charger from Linear Technology LT1513 was chosen. It's a current mode switching regulator specially configured to create a constant or programmable current/constant voltage battery charger. This component can charge a Li-ion battery with a capacity up to 1200mAh.

Since the Li-ion batteries needs more precautions for its charging, DS2764 from Maximic was used. This component is a high-precision Li+ battery monitor and protector that provides data-acquisition, storage information, and safety protection. Also in this Power Block, two Buck/Boost DC-DC converter « LTC3531 » from Linear Technology where used, to make a constant 5V and 3.3V voltages to power different parts of the system that require different voltage level. Finally, for the charger header a Micro USB 2.0 Type B was chosen , so this instrument can be charged with any Samsung charger.

### 6.2.2 Radio Frequency Communication

This block is indispensable to make the instrument completely portable in terms of wireless communication, which is very important when the measurement should be done in a specific environment of temperature and oxygen for example.

Table 6.1 gives a comparison between different RF Modules that we can use from different manufacturers.

nRF905 is the most one used in wireless communication, but it's an older technology with less performances. The S2-LP and SPIRIT1 from STMicroelectrinics are the best ones, and SPIRIT1 was chosen because of its well documentation. SPIRIT1 provides an excellent performance of receiver sensitivity, selectivity, and blocking, with a four frequency bands; 150-174 MHz, 300-348 MHz, 387-470 MHz, 779-956 MHz.

This RF Module needs a driving Microcontroller and PIC18F25K20 from Microchip Technology have been then implemented.

As a first prototype, an external RF antenna was chosen because an on-chip antenna can lead to a bad performance than with an external antenna.

### 6.2.3 Sensors Read-Out Circuit

In this block, the Operational Amplifier LTC 2063 from Analog Devices was used to amplify the output signals of the three sensors; Oxygen Sensor, ISFET pH Sensor, and RTD Pt100

Table 6.1 COMPARISON TABLE FOR DIFFERENT RF MODULES FROM DIFFERENT MANUFACTURERS.

Part	Manufacturer	RX Sensitivity	TX power	Max data rate
S2-LP	ST	-130dBm	+16dBm	500kbps
SPIRIT1	ST	-118dBm	+16dBm	500kbps
Si4455	SiLabs	-116dBm	+13dBm	500kbps
MRF89XA	Microchip	-113dBm	+12.5dBm	200kbps
CC1310	TI	-124dBm	+15dBm	50kbps
nRF905	NRF	-100dBm	+10dBm	50kbps
ATA5428	Atmel	-116.5dBm	+10dBm	20kbps
ADF7020	analog	-119dBm	+13dBm	200kbps
ADF7025	analog	-104.2dBm	+13dBm	384kbps
RF69W	hoperf	-	-	-
CMT2300A	cmostek/hoperf	-	-	-
MAX2904	maxim	-	-	-

for temperature Sensor.

For analogue to digital conversion, AD7794 from Analog Devices was used, which is a 6-Channel, Low Noise, Low Power, 24-Bit  $\Sigma\Delta$  ADC. We should note that the pH measurement depends strongly on the temperature, so this AD7794 provide an accurate temperature compensation via its differential reference. In addition, this IC have its own integrated sensor for measuring the ambient temperature. We should mention that we used just four channel of this ADC, so there are still two channels available for other sensors. Also, in this block ADUM5401 was used which is a quad-channel digital isolator with an integrated dc-to-dc converter. It provides the digital signal and power isolation between the microcontroller and the AD7794 digital lines.

#### 6.2.4 Control Unit

To manage and control the whole of the system, Microcontroller STM32F411 from ST-Microelectronics was used. It's a very efficient Microcontroller with a Core Arm 32-bit Cortex, Up to 512 Kbytes of Flash memory, and 128 Kbytes of SRAM. This CPU have 64 pins which is far enough for adding other prospective slave devices in the future.

### 6.3 PCB Design

The PCB design of this electronic system was done by Altium Software. The related schematics are presented in the Appendixes. Figure 6.2 and 6.3 present respectively the PCB board and its 3D card.



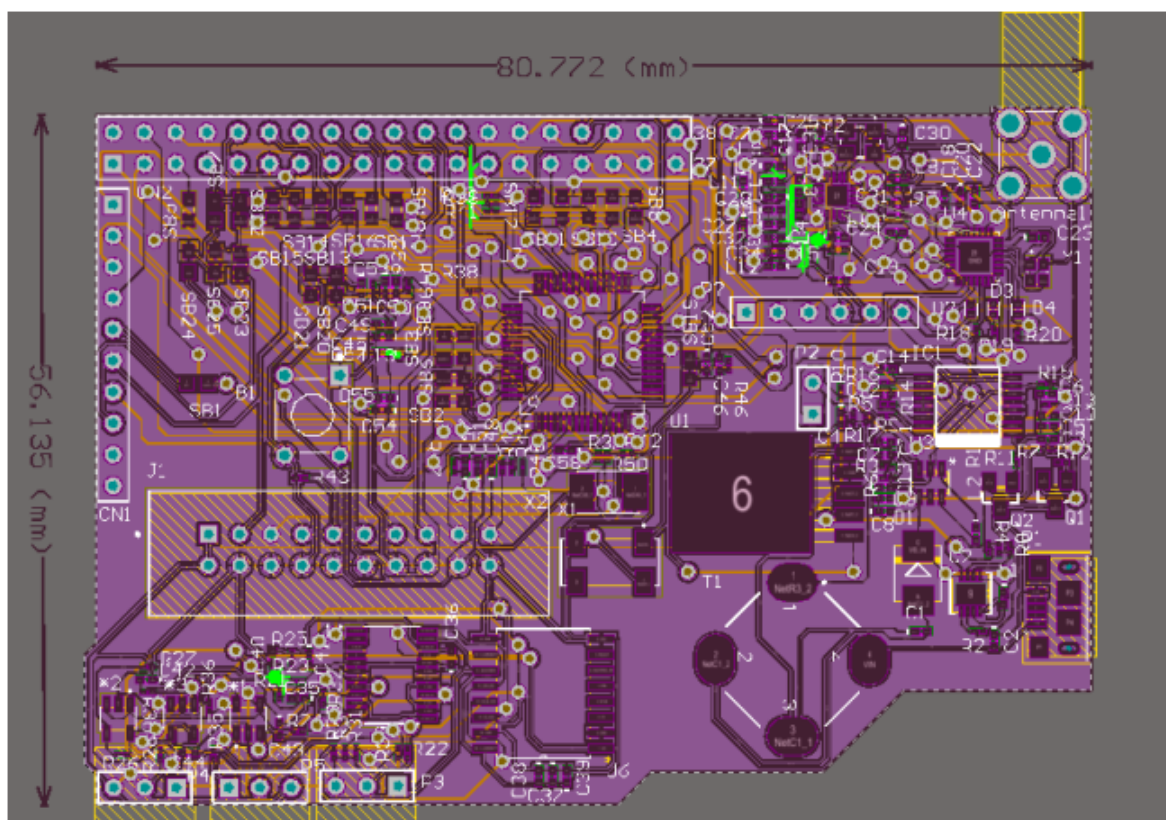


Figure 6.2 PCB board of the designed electronic system

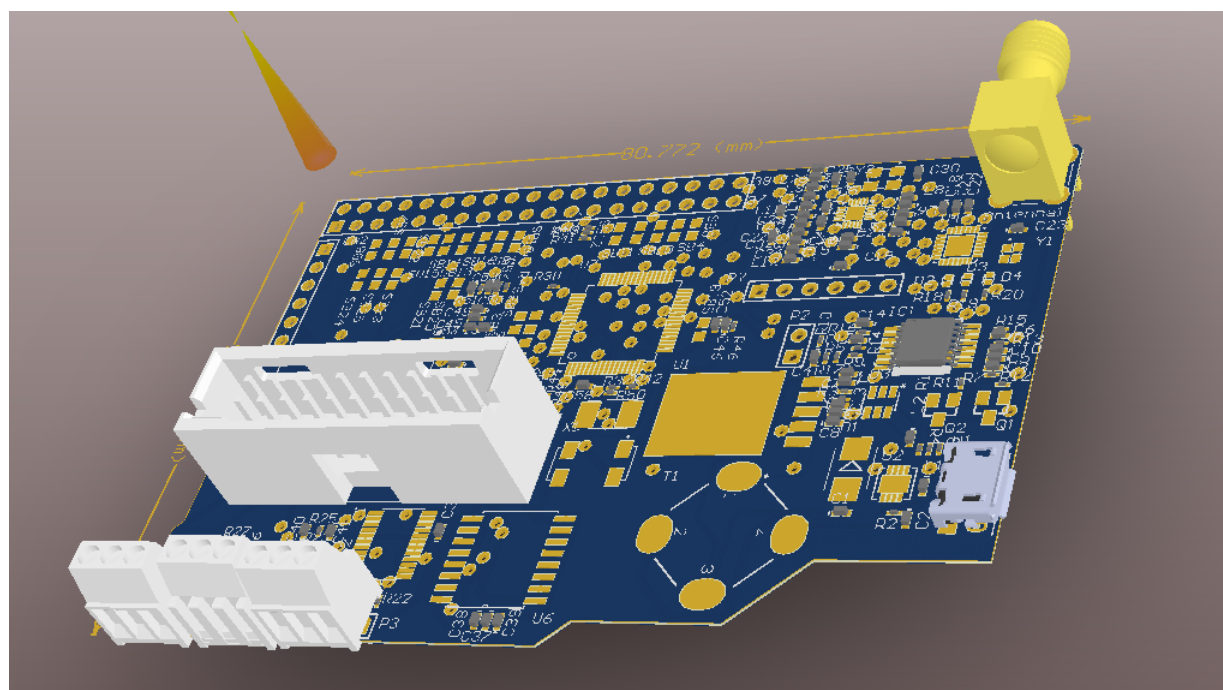


Figure 6.3 3D card of the designed electronic system

## CHAPTER 7 CONCLUSION

We presented an integrable portable 3D fluorescence microscopy based on multi-exponential fitting and the optical interference phenomenon. The proposed device was designed in a way that it doesn't require a charge-coupled device (CCD) chip or CMOS camera for detection, which resolve the temporal and spatial limitation. High speed photodiode such as Si Avalanche Photodiode is the only detection system needed to pick up the emitted fluorescent photons and construct the full sensing image. Therefore, this device is competitively higher in terms of commercialization price and in terms of portability. The experimental measurements validate the two main axes of this novel method; The interference phenomenon and the non-change of fluorescence lifetime during different steps of the measurement procedure. We reported a novel LED driver circuit to achieve a high speed fall time excitation, as a major challenging point for making a wearable devices. Furthermore, an embedded on-chip valves controller was presented to make our instrument more suitable for microfluidic handling and Organs-On-Chip platforms.

The fabricated instrument features an ease of user manipulation and can be easily interfaced with a remote PC for real-time acquisition and data processing, while being inside a cell culture incubator or again integrated with organs on chip platforms. This present elaborated sensing technique may open new perspectives towards novel generation of low cost and wearable 3D imaging and sensing.

## REFERENCES

- [1] Chen, Chien-Liang, et al. "Influence of external and intracellular pH on propofol-induced responses in rat locus coeruleus neurons." *European journal of pharmacology* 545.2-3 (2006): 115-122.
- [2] Yang, H., William M. Miller, and E. T. Papoutsakis. "Higher pH promotes megakaryocytic maturation and apoptosis." *Stem Cells* 20.4 (2002): 320-328.
- [3] Teo, Ailing, Athanasios Mantalaris, and Mayasari Lim. "Influence of culture pH on proliferation and cardiac differentiation of murine embryonic stem cells." *Biochemical engineering journal* 90 (2014): 8-15.
- [4] Putney, Luanna K., and Diane L. Barber. "Na-H exchange-dependent increase in intracellular pH times G2/M entry and transition." *Journal of Biological Chemistry* 278.45 (2003): 44645-44649.
- [5] Gruenberg, Jean, and Harald Stenmark. "The biogenesis of multivesicular endosomes." *Nature reviews Molecular cell biology* 5.4 (2004): 317
- [6] Hunte, Carola, et al. "Structure of a Na<sup>+</sup>/H<sup>+</sup> antiporter and insights into mechanism of action and regulation by pH." *Nature* 435.7046 (2005): 1197.
- [7] Stock, Christian, and Albrecht Schwab. "Protons make tumor cells move like clockwork." *Pflügers Archiv-European Journal of Physiology* 458.5 (2009): 981-992.
- [8] Kumar, Sandeep, Alakesh Das, and Shamik Sen. "Multicompartment cell-based modeling of confined migration: regulation by cell intrinsic and extrinsic factors." *Molecular biology of the cell* 29.13 (2018): 1599-1610.
- [9] Wolf, Katarina, et al. "Physical limits of cell migration: control by ECM space and nuclear deformation and tuning by proteolysis and traction force." *J Cell Biol* 201.7 (2013): 1069-1084.
- [10] Lautscham, Lena A., et al. "Migration in confined 3D environments is determined by a combination of adhesiveness, nuclear volume, contractility, and cell stiffness." *Biophysical journal* 109.5 (2015): 900-913.
- [11] Harada, Takamasa, et al. "Nuclear lamin stiffness is a barrier to 3D migration, but softness can limit survival." *J Cell Biol* 204.5 (2014): 669-682.

- [12] Davidson, Patricia M., et al. "Nuclear deformability constitutes a rate-limiting step during cell migration in 3-D environments." *Cellular and molecular bioengineering* 7.3 (2014): 293-306.
- [13] Lammerding, Jan, et al. "Lamin A/C deficiency causes defective nuclear mechanics and mechanotransduction." *The Journal of clinical investigation* 113.3 (2004): 370-378.
- [14] Zuela-Sopilniak, Noam, and Jan Lammerding. "Engineering approaches to studying cancer cell migration in three-dimensional environments." *Philosophical Transactions of the Royal Society B* 374.1779 (2019): 20180219.
- [15] Semenza, Gregg L. "Life with oxygen." *Science* 318.5847 (2007): 62-64.
- [16] Wiederkehr, Andreas, and Claes B. Wollheim. "Minireview: implication of mitochondria in insulin secretion and action." *Endocrinology* 147.6 (2006): 2643-2649.
- [17] Cannon, Barbara, and J. A. N. Nedergaard. "Brown adipose tissue: function and physiological significance." *Physiological reviews* 84.1 (2004): 277-359.
- [18] Höfling, Felix, and Thomas Franosch. "Anomalous transport in the crowded world of biological cells." *Reports on Progress in Physics* 76.4 (2013): 046602.
- [19] Brandenburg, Boerries, and Xiaowei Zhuang. "Virus trafficking—learning from single-virus tracking." *Nature Reviews Microbiology* 5.3 (2007): 197.
- [20] Li, Chen Hong, et al. "Dynamic tracking and mobility analysis of single GLUT4 storage vesicle in live 3T3-L1 cells." *Cell research* 14.6 (2004): 480.
- [21] Yildiz, Ahmet, et al. "Myosin V walks hand-over-hand: single fluorophore imaging with 1.5-nm localization." *science* 300.5628 (2003): 2061-2065.
- [22] Fujiwara, Takahiro, et al. "Phospholipids undergo hop diffusion in compartmentalized cell membrane." *The Journal of cell biology* 157.6 (2002): 1071-1082.
- [23] Mathai, P. P., James A. Liddle, and Samuel M. Stavis. "Optical tracking of nanoscale particles in microscale environments." *Applied physics reviews* 3.1 (2016): 011105.
- [24] von Diezmann, Alex, Yoav Shechtman, and W. E. Moerner. "Three-dimensional localization of single molecules for super-resolution imaging and single-particle tracking." *Chemical reviews* 117.11 (2017): 7244-7275.
- [25] Berezin, Mikhail Y., and Samuel Achilefu. "Fluorescence lifetime measurements and biological imaging." *Chemical reviews* 110.5 (2010): 2641-2684.

- [26] Baldini, Francesco. "Alexander P. Demchenko: Introduction to fluorescence sensing." *Analytical and Bioanalytical Chemistry* 395.5 (2009): 1195.
- [27] Becker, Wolfgang. *Advanced time-correlated single photon counting techniques*. Vol. 81. Springer Science Business Media, 2005.
- [28] Ross, Justin A., and David M. Jameson. "Time-resolved methods in biophysics. 8. Frequency domain fluorometry: applications to intrinsic protein fluorescence." *Photochemical Photobiological Sciences* 7.11 (2008): 1301-1312.
- [29] Perrin, Francis. "La fluorescence des solutions-Induction moleculaire.Polarisation et duree d'emission.Photochimie." *Annales de physique*. Vol. 10. No. 12. EDP Sciences, 1929.
- [30] Selanger, K. A., J. Falnes, and T. Sikkeland. "Fluorescence lifetime studies of Rhodamine 6G in methanol." *The Journal of Physical Chemistry* 81.20 (1977): 1960-1963.
- [31] Birks, J. B. "Photophysics of Aromatic Molecules, Chap. 10." (1970).
- [32] Pawley, James, ed. *Handbook of biological confocal microscopy*. Springer Science Business Media, 2010.
- [33] Sanderson, Michael J., et al. "Fluorescence microscopy." *Cold Spring Harbor Protocols* 2014.10 (2014): pdb-top071795.
- [34] Denk, Winfried, James H. Strickler, and Watt W. Webb. "Two-photon laser scanning fluorescence microscopy." *Science* 248.4951 (1990): 73-76.
- [35] Betzig, Eric, et al. "Imaging intracellular fluorescent proteins at nanometer resolution." *Science* 313.5793 (2006): 1642-1645.
- [36] Hess, Samuel T., Thanu PK Girirajan, and Michael D. Mason. "Ultra-high resolution imaging by fluorescence photoactivation localization microscopy." *Biophysical journal* 91.11 (2006): 4258-4272.
- [37] Higashino, Nobuya, et al. "LED-CT Scan for pH Distribution on a Cross-Section of Cell Culture Medium." *Sensors* 18.1 (2018): 191.
- [38] I. Gharib, and M. Sawan, "Towards Portable 3D Interferometric Fluorescence Microscopy for Microfluidics based platforms".
- [39] I. Gharib, and M. Sawan, "Portable 3D Interferometric Fluorescence Microscopy", 2020.

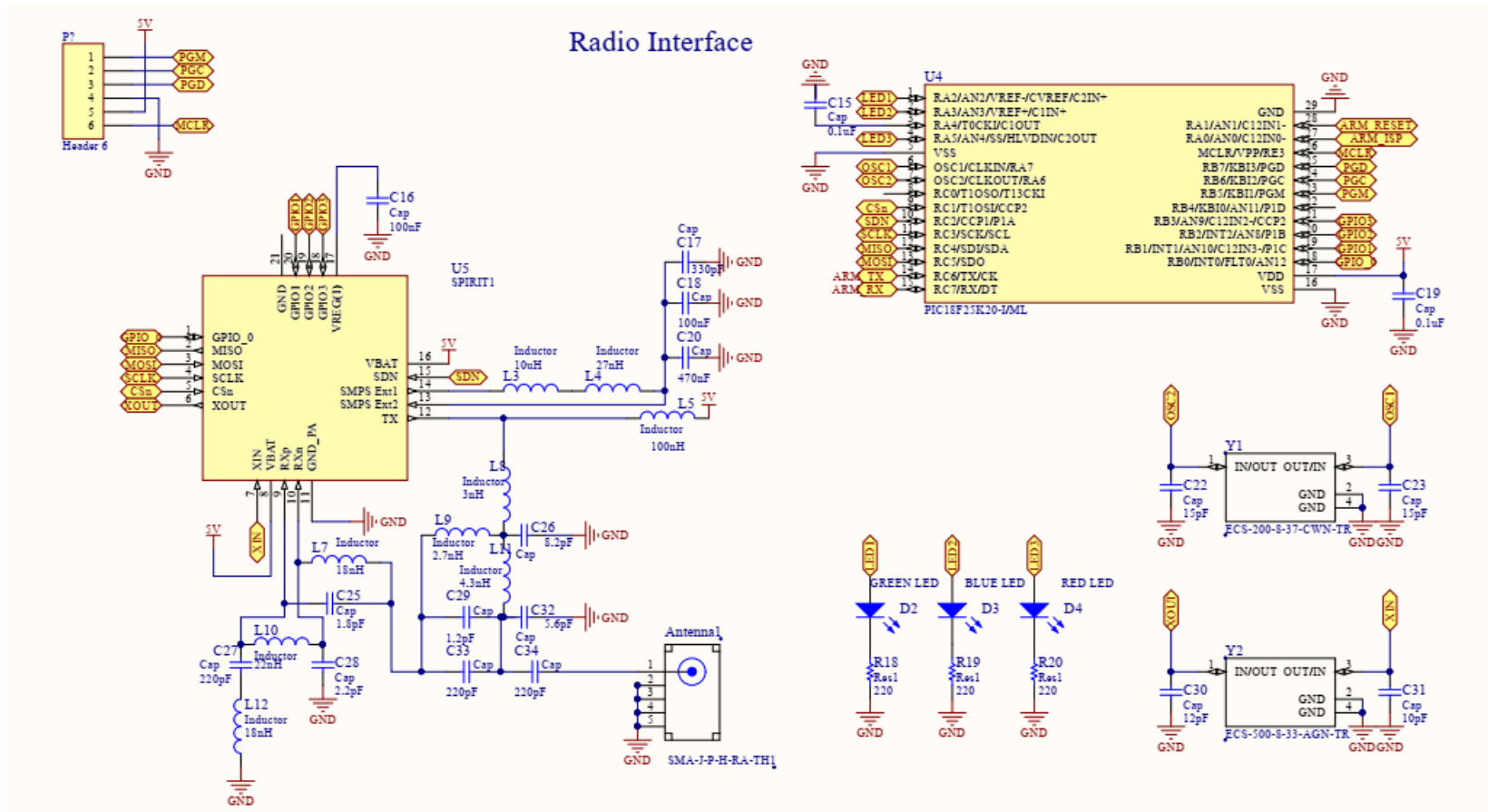
- [40] Cubeddu, Rinaldo, et al. "Fluorescence lifetime imaging: an application to the detection of skin tumors." *IEEE Journal of selected topics in quantum electronics* 5.4 (1999): 923-929.
- [41] Berezin, Mikhail Y., and Samuel Achilefu. "Fluorescence lifetime measurements and biological imaging." *Chemical reviews* 110.5 (2010): 2641-2684.
- [42] Lakowicz, Joseph R., and Henryk Szmajda. "Fluorescence lifetime-based sensing of pH, Ca<sup>2+</sup>, K<sup>+</sup> and glucose." *Sensors and Actuators B: Chemical* 11.1-3 (1993): 133-143.
- [43] Burdikova, Zuzana, et al. "Measurement of pH micro-heterogeneity in natural cheese matrices by fluorescence lifetime imaging." *Frontiers in microbiology* 6 (2015): 183.
- [44] Enderlein, Jörg, and Rainer Erdmann. "Fast fitting of multi-exponential decay curves." *Optics Communications* 134.1-6 (1997): 371-378.
- [45] Kim, Jeongtae, and Jiyeong Seok. "Statistical properties of amplitude and decay parameter estimators for fluorescence lifetime imaging." *Optics express* 21.5 (2013): 6061-6075.
- [46] Yang, Sejung, et al. "Estimation of multiexponential fluorescence decay parameters using compressive sensing." *Journal of biomedical optics* 20.9 (2015): 096003.
- [47] Squires, Todd M., and Stephen R. Quake. "Microfluidics: Fluid physics at the nanoliter scale." *Reviews of modern physics* 77.3 (2005): 977.
- [48] I. Gharib, and M. Sawan, "High-efficiency LED Driver for Short Fluorophores Lifetime Biosensing Applications", *IEEE International New Circuits and Systems Conference (NEWCAS)*, 2019.
- [49] Banks, P. R., Paquette, D. M. (1995). Comparison of three common amine reactive fluorescent probes used for conjugation to biomolecules by capillary zone electrophoresis. *Bioconjugate chemistry*, 6(4), 447-458.
- [50] Becker, W., Bergmann, A., König, K., Tirlapur, U. (2001, April). Picosecond fluorescence lifetime microscopy by TCSPC imaging. In *Multiphoton Microscopy in the Biomedical Sciences* (Vol. 4262, pp. 414-420). International Society for Optics and Photonics.
- [51] Ryder, A. G., Power, S., Glynn, T. J., Morrison, J. J. (2001, July). Time-domain measurement of fluorescence lifetime variation with pH. In *Biomarkers and Biological*

- Spectral Imaging (Vol. 4259, pp. 102-110). International Society for Optics and Photonics.
- [52] Wang, H., Qi, Y., Mountziaris, T. J., Salthouse, C. D. (2014). A portable time-domain LED fluorimeter for nanosecond fluorescence lifetime measurements. *Review of Scientific Instruments*, 85(5), 055003.
  - [53] Cox, M. P., Ma, H., Bahlke, M. E., Beck, J. H., Schwartz, T. H., Kymissis, I. (2010). LED-based optical device for chronic in vivo cerebral blood volume measurement. *IEEE transactions on electron devices*, 57(1), 174-177.
  - [54] Ong, Y. S., Grout, I., Lewis, E., Mohammed, W. S. (2018). Utilization of data classification in the realization of a surface Plasmon resonance readout system using an FPGA controlled RGB LED light source. *IEEE Sensors Journal*, 18(20), 8517-8524.
  - [55] Kishi, T., Tanaka, H., Umeda, Y., Takyu, O. (2014). A high-speed LED driver that sweeps out the remaining carriers for visible light communications. *Journal of Lightwave Technology*, 32(2), 239-249.
  - [56] Pacheco-Linan, P. J., Garzon, A., Tolosa, J., Bravo, I., Canales-Vazquez, J., Rodríguez-López, J., ... García-Martínez, J. C. (2016). pH-Sensitive Fluorescence Lifetime Molecular Probes Based on Functionalized Tristyrylbenzene. *The Journal of Physical Chemistry C*, 120(33), 18771-18779.
  - [57] Li, D. D. U., Ameer-Beg, S., Arlt, J., Tyndall, D., Walker, R., Matthews, D. R., ... Henderson, R. K. (2012). Time-domain fluorescence lifetime imaging techniques suitable for solid-state imaging sensor arrays. *Sensors*, 12(5), 5650-5669.
  - [58] Jin, D., Connally, R., Piper, J. (2007). Practical time-gated luminescence flow cytometry. I: Concepts. *Cytometry Part A: The Journal of the International Society for Analytical Cytology*, 71(10), 783-796.
  - [59] Halbritter, H., Jäger, C., Weber, R., Schwind, M., Möllmer, F. (2014). High-speed LED driver for ns-pulse switching of high-current LEDs. *IEEE Photonics Technology Letters*, 26(18), 1871-1873.
  - [60] I. Gharib, and M. Sawan, "Microfluidic Valve Arrays for Drug Delivery in Organ-OnChips", *IEEE Engineering in Medicine and Biology Society Conference (EMBC)*, 2020.

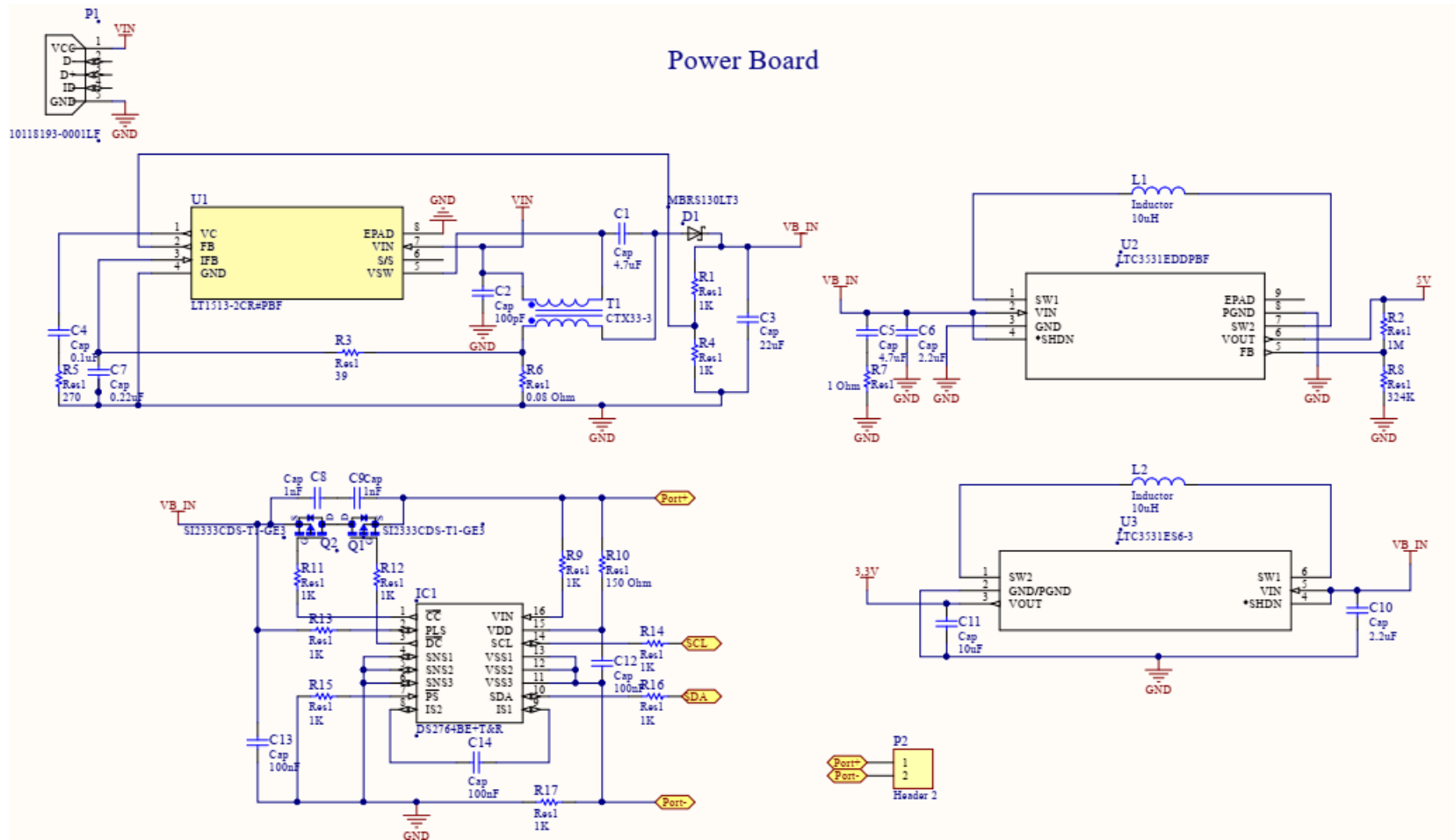
- [61] Bhise, N. S., Manoharan, V., Massa, S., Tamayol, A., Ghaderi, M., Miscuglio, M., ... & Annabi, N. (2016). A liver-on-a-chip platform with bioprinted hepatic spheroids. *Biofabrication*, 8(1), 014101.
- [62] Stucki, A. O., Stucki, J. D., Hall, S. R., Felder, M., Mermoud, Y., Schmid, R. A., ... & Guenat, O. T. (2015). A lung-on-a-chip array with an integrated bio-inspired respiration mechanism. *Lab on a Chip*, 15(5), 1302-1310.
- [63] Marsano, A., Conficconi, C., Lemme, M., Occhetta, P., Gaudiello, E., Votta, E., ... & Rasponi, M. (2016). Beating heart on a chip: a novel microfluidic platform to generate functional 3D cardiac microtissues. *Lab on a Chip*, 16(3), 599-610.
- [64] Wang, H., Xiang, Z., Hu, C. F., Pastorin, G., Fang, W., & Lee, C. (2014). Microneedle Array Integrated With CNT Nanofilters for Controlled and Selective Drug Delivery. *Journal of Microelectromechanical Systems*, 23(5), 1036-1044.
- [65] Huang, P. L., Kuo, P. H., Huang, Y. J., Liao, H. H., Yang, Y. J. J., Wang, T., ... & Lu, S. S. (2011). A controlled-release drug delivery system on a chip using electrolysis. *IEEE Transactions on Industrial Electronics*, 59(3), 1578-1587.
- [66] MoraesEqual contributions, C., Labuz, J. M., Leung, B. M., Inoue, M., Chun, T. H., & Takayama, S. (2013). On being the right size: scaling effects in designing a human-on-a-chip. *Integrative Biology*, 5(9), 1149-1161.
- [67] Jensen, E. C., Grover, W. H., & Mathies, R. A. (2007). Micropneumatic digital logic structures for integrated microdevice computation and control. *Journal of Microelectromechanical Systems*, 16(6), 1378-1385.
- [68] Potluri, S., Pop, P., & Madsen, J. (2019). Design-For-Testability of On-Chip Control in mVLSI Biochips. *IEEE Design & Test*, 36(1), 48-56.
- [69] Kawai, K., Arima, K., Morita, M., & Shoji, S. (2015). Microfluidic valve array control system integrating a fluid demultiplexer circuit. *Journal of Micromechanics and Micro-engineering*, 25(6), 065016.
- [70] Gere, J. M., & Goodno, B. J. (2001). *Mechanics of Materials* 5th. Brooks Cole, 780.



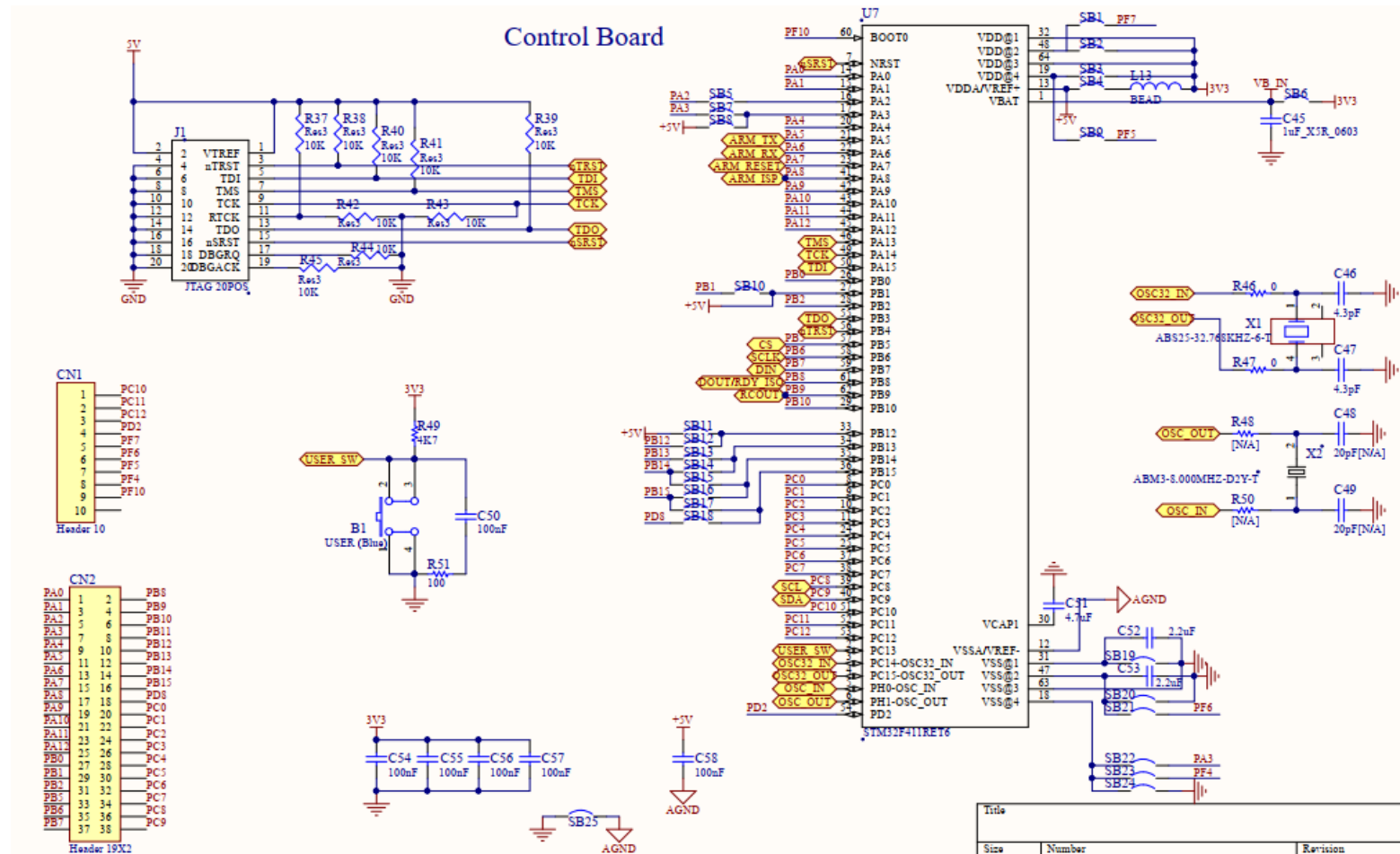
## APPENDIX A



## APPENDIX B



## APPENDIX C



## APPENDIX D

